“Using *Drosophila melanogaster* to model glial lipid biology dysfunction in Alzheimer’s disease”

by Roman Seliverstov
C1712999

Thesis for submission for the degree of
Master of Philosophy (MPhil)
June 2024

Table of Contents

Acknowledgements

First and foremost, I would like to dedicate this thesis to my grandmother Larisa, who valued education like nobody else, fostered an appreciation for science and knowledge, and who gave her all to make sure I would get a chance to embark on this academic journey. Большое спасибо тебе от всего сердца.

I would like to thank my supervisor Dr Owen Peters for believing in me as a scientist and offering a place in his fantastic research laboratory. Thank you so much for your encouragement, support, endless enthusiasm and the chance to turn my technician position into a research project. I would also like to thank Dr Gaynor Smith for her fantastic co-supervision, as well as input and suggestions during lab meetings.

I would like to massively thank the DRI Fly lab for being such an amazing team. Thank you for making the endless hours of flipping vials fly by and thank you for putting up with my quirks and chaotic caffeinated streams of consciousness. Namely, I would like to thank Lucie for making it past the Brecon trek together and the mental vigour it provided later on, Peta for always being the most kind and optimistic person, Uroosa for being the best desk mate in the office (and sharing side-eyes with), and of course Jess and Bea, the Dobbies. Thank you to Hannah for your ability to make everyone feel welcome, and massive thank you to Dan for answering my endless questions about flies and sharing literature to get this project started. Of course, the biggest thanks go to Leo, the Master, who helped me tremendously with this project and taught me probably everything I know about the flies.

To the wider DRI and HEB, thank you so much for creating such a fantastic working environment. Thank you to Dr Andrew Jefferson and Dr Dina Fathalla for being the most understanding and most amazing colleagues, you really are the most precious gems of the DRI. Thank you to all the friends I have made along this degree; thank you to Jincy, Rachel, Karolina, Sri and the other stem cell besties, to Eilish and Elena, to the ECR reps. Massive thank you to the HEB tech team, to Toni, Olena, Emma, Jo, Mark and Bob, for making sure the building is still standing and functioning. To many more wonderful colleagues from HEB, who I simply could not fit here, thank you!

Special thanks to my friends; to Aggie for sticking out together through our undergrad and still coming out of it as friends, to Max for being the most patient friend and housemate, to Fraser for being the most fabulous and inspiring person, and to Tara for always knowing the right things to say.

I would like to thank my family for the opportunity to move far away from home to pursue my dreams and career. It was definitely a team effort, and I will forever appreciate it. Thank you Mum and Dad, for having the trust in me and always being by my side. I would also like to thank my newfound family; thank you Andrea and Nigel for looking after me and accepting me as your son. Ultimately, I would like to thank fy nghariad Liam for seeing and accepting me for who I am and being the biggest support throughout this sometimes-rocky journey. Thank you so much for putting up with me, making me smile, and proofreading everything to make sure I don’t write long weird sentences (you best believe he will be proofreading this as well). I am excited to see what the next chapter has in store for us.

Summary

Glial lipid accumulation in Alzheimer's disease (AD) has been known since the disease was first described in 1902, however remained a rather unexplored aspect of AD until recently. With recent advances in bioinformatics, the evidence of genetic involvement in lipid homeostasis dysfunction in AD became evident, with many significant risk-genes associated with lipid-related pathways. Newest findings suggest that some of these genes are tightly involved in lipid transport from neurons to glial cells, in response to AD pathology. Whilst carrying out an apparent neuroprotective role, this shuttling also appears to negatively affect glial ability to carry out their homeostatic functions. In the forefront of this research, Drosophila melanogaster, the fruit fly, emerged as a perfect model for studying the causality of this dysregulation.

In this thesis we proposed and characterised a novel model of studying lipid droplet (LD) homeostasis dysfunction, by expressing a fluorescent marker for lipid droplets in fly wings. Fly wings contain both neurons and glia in close proximity, allowing to examine the interactions between these cell types, as well as are an easily accessible tissue.

The glial wing LD model was shown to be responsive to axotomising injury and modifiable by neuronal debris phagocytosis modulation. Furthermore, the model has shown an increase in glial LDs in response to glial amyloid expression. Finally, the creation of a two-system expression model, allowing for independent expression of different transgenes in neurons and glia, led to a successful recreation of the glial LD accumulation in response to neuronal amyloid toxicity.

Further development and utilisation of this model could provide a novel model of LD homeostasis examination. With growing evidence of lipid transport involvement in AD pathology, this model could allow for high-throughput phenotypic screening of AD risk genes, further unravelling this molecular hallmark of the disease.

Table of figures

Table of tables

List of abbreviations

a.u.	arbitrary unit
AA	amino acid
AAPsα/β	soluble amyloid precursor protein α/β
Ab	antibody
ABCA1/7	ATP-binding cassette transporter 1/7
Aβ40/42	Amyloid beta 40/42
ACSL1	acyl-CoA synthetase long chain family member 1
Acv	anterior cross-vein
AD	Alzheimer’s disease
AICD	amyloid precursor protein intracellular domain
AMPK	AMP-activated protein kinase
ANOVA	analysis of variance
Aos	Argos
APOE	apolipoprotein E
APP	amyloid precursor protein
Appl	amyloid precursor protein-like protein
Arc	Arctic
BACE1	beta-site amyloid precursor protein cleaving enzyme 1
BBB	blood brain barrier
BDSC	Bloomington Drosophila Stock Centre
CD2AP	CD2-associated protein
CMY	cornmeal-molasses-yeast
CNS	central nervous system
CSF	cerebrospinal fluid
DNA	deoxyribonucleic acid
DPE	days post eclosion
DS	Down syndrome
dsDNA	double-stranded DNA
Eato	engulfment ABC Transporter in the ovary
EDTA	ethylenediaminetetraacetic acid
EGFP	enhanced green fluorescent protein
EOAD	early-onset Alzheimer’s disease
FDA	Food and Drug Association
FIJI	Fiji Is Just ImageJ
gDNA	genomic DNA
GFP	green fluorescent protein
GLaz	glial Lazarillo
GWAS	genome-wide association studies
hAPP	human amyloid precursor protein
Hsp70	heat shock protein 70
iPSC	induced pluripotent stem cells
JNK	c-Jun N-terminal kinase
Klar	klarsicht (DE: transparent)
L1-5	longitudinal vein 1-5

LacZ	β-galactosidase
LD	lipid droplet
ldd	lipid droplet deficient
LOAD	late-onset Alzheimer’s disease
LRP1	low density lipoprotein receptor-related protein 1
LXR	liver X receptor
mCD8	membrane-targeted cluster of differentiation 8
MCI	mild cognitive impairment
MRI	magnetic resonance imaging
Nec	necrotic
NFT	neurofibrillary tangle
NLaz	neuronal Lazarillo
NMNAT	nicotinamide mononucleotide adenylyltransferase
nSyb	neuronal synaptobrevin
OE	overexpression
PBS	phosphate buffered saline
PCR	polymerase chain reaction
PFA	paraformaldehyde
PI	post injury
PI3K	phosphoinositide 3-kinase
PICALM	phosphatidylinositol binding clathrin assembly protein
PNS	peripheral nervous system
POI	product of interest
PSEN1/2	presenilin 1/2
PTX	PBS and Triton X solution
qPCR	quantitative polymerase chain reaction
Repo	reversed polarity
RM	repeated measure
RNA	ribonucleic acid
RNAi	RNA interference
ROI	region of interest
ROS	reactive oxygen species
SD	standard deviation
SNP	single nucleotide polymorphism
SREBP	sterol regulatory element-binding protein
Sv40	simian virus 40
TAE	Tris-acetate- ethylenediaminetetraacetic acid
TREM2	triggering receptor expressed on myeloid cells 2
UAS	upstream activating sequence
VDRC	Vienna Drosophila Resource Center
WD	Wallerian degeneration

1. Introduction

1.1. Background

Alzheimer’s disease (AD) is a neurodegenerative disorder, manifesting itself through symptoms such as decline of brain function and cognition, memory loss and dementia. Identified and characterised by Alois Alzheimer in 1901 (Stelzmann et al. 1995), to this day the aetiology of this disorder remains elusive.

No effective treatment has yet been discovered, with symptomatic treatment remaining the only therapeutic strategy, however some recent advances in immunotherapy have been showing promising results in slowing down the disease progression.

The prevalence of dementia within the UK population aged over 65 years is estimated to be over 7%, with AD making up to 62% of that number (Prince et al. 2014). It was estimated the global cost of dementia alone was $1.313 trillion, with informal care and direct social sector costs making up to 84% of that (Wimo et al. 2023). Diagnosed patients depend on caregivers to support them with managing daily activities, administering medication, and with various other needs. This ultimately leads to withdrawal of two people from the active work force, causing a shadow effect on the healthcare system and the economy. The rapidly increasing rate of population aging only exacerbates this issue, amplifying an already existing strain on both social welfare system and public funds.

With the molecular mechanisms underlying Alzheimer’s disease remaining unclear, it is crucial that we establish the exact pathways that contribute towards the progression of this disease. It has been established that neurodegeneration in AD starts decades before the manifestation of any cognitive symptoms (Sperling et al. 2011; Swaddiwudhipong et al. 2023). Understanding the molecular mechanisms behind AD could allow us to provide early diagnosis and therapeutical intervention before the onset of the disease. Furthermore, understanding the molecular mechanisms of AD would help us identify the potential targets and develop novel therapeutic strategies that modulate disease progression.

1.2. Disease Overview

1.2.1. Clinical Manifestation

AD mainly affects cognitive functions, as well as memory and behaviour (López and DeKosky 2008; Atri 2019). The link of cognitive decline and ageing has been established since the Antiquity, with a more precise understanding of the disease only starting to develop by the nineteenth century (Berchtold and Cotman 1998). Onset of AD initially manifests in mild lapses in memory which is often misattributed as Mild Cognitive Impairment (MCI) in old age. MCI shares initial symptoms with AD and is considered to be a transitional state between healthy cognition and dementia, with an annual conversion rate of MCI into AD at about 10-15%(Kelley and Petersen 2007; Farias et al. 2009). As AD advances, more severe irreversible symptoms such as memory loss, aberrant reasoning and communication problems develop. Overall, the progression of AD impacts the daily lives of patients, with tasks such as grooming, cooking, and dressing becoming challenging, eventually leading to complete reliance on caring assistance. Beyond the cognitive manifestation of AD, a variety of neuropsychiatric and physiological symptoms prevail, such as depression, sleep disturbances, aggression, and psychosis (Li et al. 2014). One of their manifestations, the “sundowning” syndrome, is characteristic of AD and dementia and entails exacerbation of these symptoms during late hours (Khachiyants et al. 2011).

1.2.2. Neuropathological hallmarks

Brain atrophy is one of the physical hallmarks of AD, which can be detected by magnetic resonance imaging (MRI), and mostly affects the hippocampus, neo- and subcortex regions of the brain (Pini et al. 2016). Besides the general clinical picture, several neuropathological hallmarks of AD exist, with the two most crucial ones being senile plaques and neurofibrillary tangles (NFTs). Ultimately, accumulation of these hallmarks is associated with neurodegeneration, which drives disease. Furthermore, amyloid deposition has been associated with cerebrovascular pathogenesis and dysfunction, such as cerebral amyloid angiopathy, which has been linked with the vascular aetiology of AD and other dementias (Greenberg et al. 2020). Both plaques and NFTs initially localise in the transentorhinal cortex, spreading to other regions of the brain as the disease progresses (Figure 1.1) (Braak and Braak 1985; Braak and Braak 1991). The following spread into entorhinal cortex and hypothalamus coincides with the early symptoms of the disease, as these brain regions are directly involved in memory, navigation and sleep (Schultz et al. 2015; Vercruysse et al. 2018).

Finally, plaques and NFTs spread into the neocortex and primary sensory areas, which are responsible for cognition, consciousness and the sensory systems (Diaz and Gleeson 2009), neurodegeneration of which leads to characteristic symptoms of late Alzheimer's disease.

Senile plaques are aberrant extracellular aggregates of amyloid beta protein (Aβ). It has been shown that the plaques appear in stages in different regions of the brain years before the onset of neurological symptoms (Bateman et al. 2012). These extracellular plaques are a result of aberrant amyloid precursor protein (APP) processing by β- and γ-secretases. This, together will amyloid clearance disturbance, leads to abnormal accumulation of Aβ40 and Aβ42 peptides, creating insoluble extracellular peptide plaques (Hardy and Selkoe 2002; DeTure and Dickson 2019). NFTs, on the other hand, are thick insoluble peptide filaments made of aggregated hyperphosphorylated tau protein (Muralidar et al. 2020). Normally, tau protein plays and important role in supporting microtubular structure of neuronal axons, however when hyperphosphorylated and misfolded, it created insoluble aggregates, which lead to neurodegeneration not only in AD, but also several other tauopathies (Zhang et al. 2022).

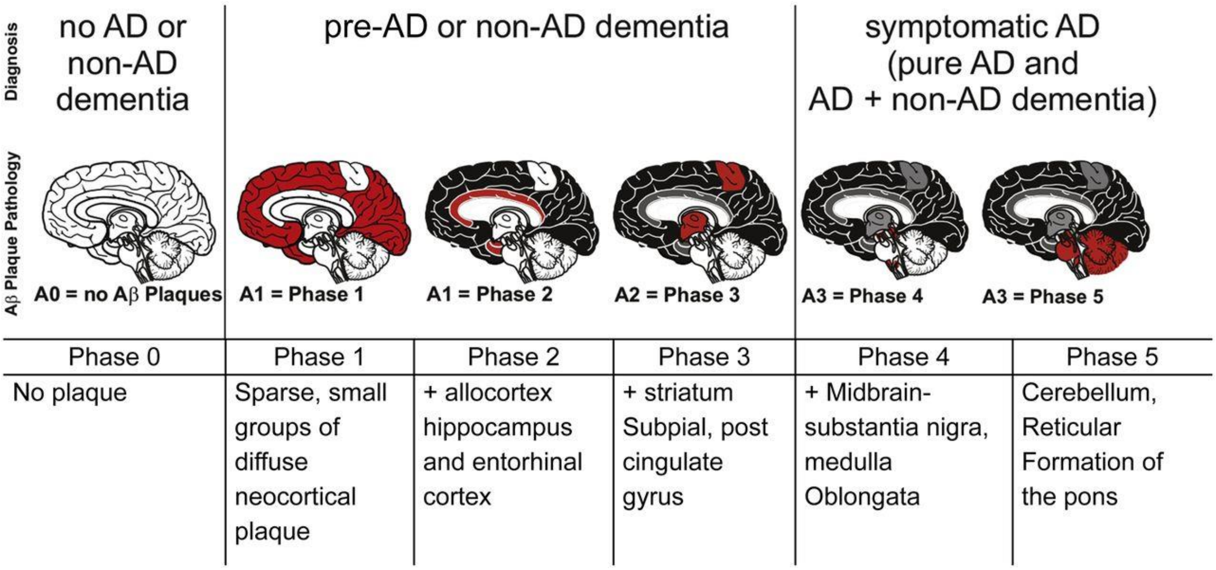

Phase 0	Phase 1	Phase 2	Phase 3	Phase 4	Phase 5
No plaque	Sparse, small groups of diffuse neocortical plaque	+ allocortex hippocampus and entorhinal cortex	+ striatum Subpial, post cingulate gyrus	+ Midbrain-substantia nigra, medulla Oblongata	Cerebellum, Reticular Formation of the pons

Figure 1.1 Gradual amyloid plaque spread in AD.
Schematic of amyloid spread, showing affected brain regions and the associated diagnosis, Aβ42 plaque pathology score, and Thal phase.
Figure adapted from Koychev et al. (2020).

1.2.3. Glial inflammation and blood brain barrier dysfunction

Beyond amyloid plaques and neurofibrillary tangles, several other mechanisms, such as glia-driven neuroinflammation and blood brain barrier (BBB) dysfunction are believed to actively contribute to AD pathophysiology (Figure 1.2). Growing evidence suggests that in AD microglia and astrocytes, which are normally responsible for supporting neurons and mediating the immune surveillance, become hyperactivated and aberrantly initiate inflammation cascades (Al-Ghraiybah et al. 2022) (Figure 1.2). These pro-inflammatory cues lead to cytokine production by glia, raising the oxidative stress and negatively impacting neurons, and potentially exacerbating the neurotoxicity caused by amyloid plaques and neurofibrillary tangles (Leng and Edison 2021). Dysfunction in BBB, also mediated by glia, leads to increased BBB permeability and subsequent further accumulation of Aβ42 and tau, oxidative stress, neurotoxic blood proteins and iron, all of which contribute to neurodegeneration (Sharma et al. 2021). The disrupted BBB leads to vascular symptoms of AD, such as brain hemorrhage, white blood cell infiltration and inflammation cause by blood proteins (Keep et al. 2014). BBB dysfunction also leads to additional microglial activation (Takata et al. 2021), which in turn promotes further deterioration (Haruwaka et al. 2019), potentially creating a damaging feedback loop. Furthermore, amyloid accumulation negatively affects axonal myelination, destroying the myelin sheathing produced by oligodendrocytes (Maitre et al. 2023), disrupting the efficiency of active potential transmission and axonal integrity (Figure1.2). With the above pathophysiological hallmarks in mind, it is apparent that AD aetiology is complex, highly multifaceted, and is potentially a result of an intricate interplay of several of these mechanisms, once again reiterating the importance of understanding what actually drives AD on a molecular level.

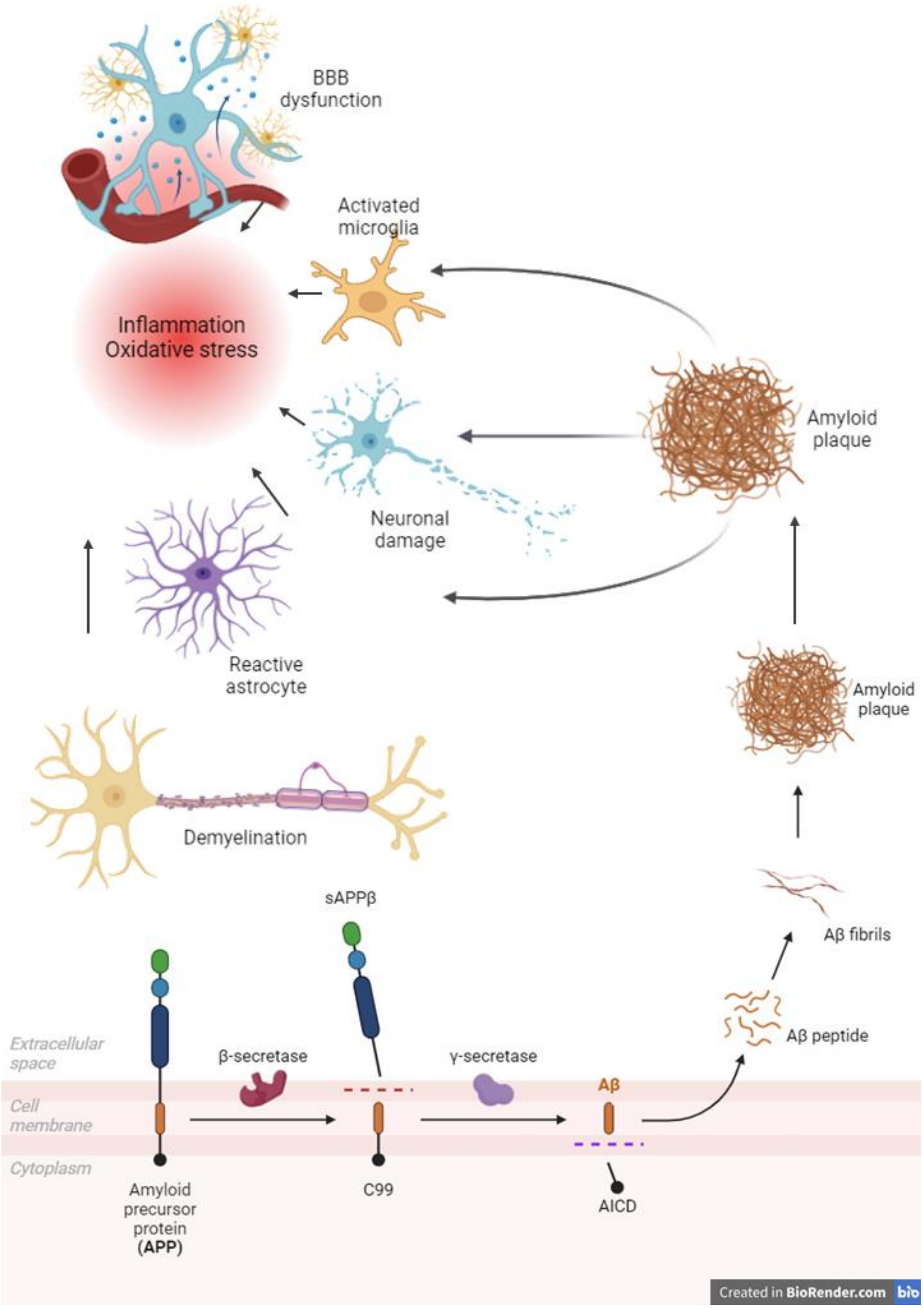

Figure 1.2. Amyloid pathophysiology.
Schematic of complex AD pathophysiology driven by amyloid production. Amyloidogenic processing (discussed in more detail in Chapter 1.3.1.) results in production of Aβ monomers, which readily aggregate first into oligomers, then fibrils, ultimately becoming amyloid plaques. These fibrils and plaques in turn launch several pathological mechanisms, such as activation of astrocytes and microglia, which contributes to inflammation in AD and aberrant neuronal metabolic support. Amyloid also drives demyelination of neurons and BBB dysfunction, further fuelling neurodegeneration and driving inflammation. Within cells, tau aggregates form neurofibrillary tangles as a result of microtubule disintegration. This aggregation leads to tauopathy, another hallmark of neurodegeneration in AD. Furthermore, amyloid oligomers cause damage and dysfunction to mitochondria in both neurons and glial cells, further facilitating neurodegeneration, disrupting cellular homeostasis and contributing to oxidative stress.
Figure adapted and modified from Panza et al. (2019) and created using BioRender.com.

1.3. Molecular aetiology of AD

1.3.1. Amyloid cascade

The potential involvement of a wide range of mechanisms in the progression of AD led to the founding of several hypotheses attempting to explain how the disease begins. The most widely established hypothesis remains the amyloid cascade hypothesis. Initially proposed just over 30 years ago (Hardy and Higgins 1992), the Amyloid cascade hypothesis was based on accumulating evidence that mutations in amyloid precursor protein (APP) itself (Goate et al. 1991), as well as in enzymes cleaving it in normal conditions (Scheuner et al. 1996; De Strooper et al. 1998; Yan et al. 1999) result in an aberrant build-up of Aβ42 peptides. These findings cemented amyloid as the centrepiece of AD pathogenesis. To better understand the possible implication of amyloid cascade in AD, it is important to understand how APP is normally processed and where does it go wrong.

Aβ is a small peptide, produced during the proteolytic cleavage of APP. The biological function of APP and the products remains unclear, with some evidence suggesting involvement in synaptic homeostasis, axon pruning and degeneration, and apoptosis (Müller and Zheng 2012; Hampel et al. 2021). In the non-amyloidogenic pathway, APP is cleaved by α-secretase at the Aβ domain, creating the C-terminal (C83) and N-terminal (APPsα) fragments (Figure 1.3A) (Zhao et al. 2020). C83 is subsequently cleaved by γ-secretase, producing the p3 peptide, which has also been debated to have an involvement in AD (Kuhn et al. 2020). During the amyloidogenic pathway, β-secretase (BACE1) cleaves APP beyond the Aβ domain, generating N-terminal fragment (APPsβ) and C-terminal fragment (C99). C99 is then cleaved by γ-secretase, producing APP intracellular domain (AICD) and Aβ peptides of various lengths, with Aβ40 and Aβ42 involved in AD the most (Karran et al. 2011; Zhao et al. 2020). Aβ42 is more involved in plaque formation, compared to Aβ40 (Gravina et al. 1995); the ratio between two (Aβ42/Aβ40 ratio) has been utilised as a cerebrospinal fluid (CSF) biomarker of AD pathology (Graff-Radford et al. 2007). The unique steps of amyloidogenic processing have unveiled several pharmaceutic targeting points, which were utilised in creating anti-amyloid therapeutics (Figure 1.3B) (Zhao et al. 2020).

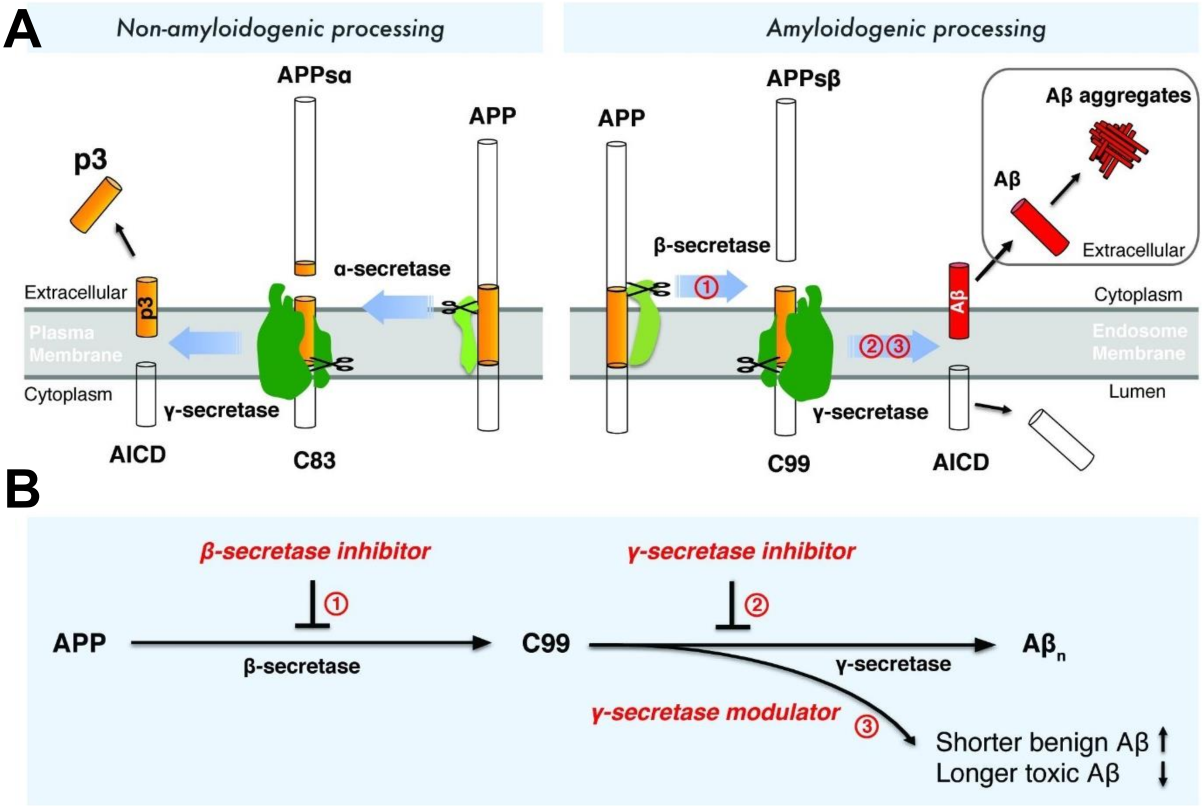

Figure 1.3. Amyloid precursor protein (APP) processing pathways.
A) Non-amyloidogenic pathway favours α-secretase activity, ultimately resulting in creation of p3 peptide and APP intracellular domain (AICD). Contrary, amyloidogenic processing pathway favours β-secretase activity, resulting in creation of AICD and the neurotoxic Aβ peptide, which is capable of forming amyloid aggregates. **B)** Amyloidogenic pathway-specific druggable targets, which potentially lower toxic amyloid peptide production.
Figure taken from Zhao et al. (2020).

The monomers of amyloid-β peptides are then capable of binding together, forming soluble oligomers and insoluble amyloid fibrils (Chen et al. 2017). Whilst it was initially accepted that those insoluble fibrils are the main driver of neurodegeneration in AD, early research has shown little correlation between the fibril deposition in plaques and the neuronal loss in AD (Terry et al. 1991). It has since been shown that the oligomers, capable of spreading due to their solubility, may be the toxic disease-driving molecules (Kayed et al. 2003; Cline et al. 2018), or contribute to fibril formation (Verma et al. 2015).

The main reasoning behind this hypothesis is that the Aβ CSF biomarkers predate other established biomarkers, such as phosphorylated tau, and structural brain changes by many years (Jack et al. 2010; Jack and Holtzman 2013). This suggests that Aβ could be essential for initiating the progression of AD via other molecular pathways, mentioned previously. Specifically, accumulating evidence suggests that tau phosphorylation and subsequent pathogenesis is promoted by Aβ (Oliveira et al. 2015; He et al. 2018; Busche and Hyman 2020), implying synergistic interaction between the two hallmarks of AD. Furthermore, the apparent effect of Aβ on glial activation and their neuroinflammation dysregulation, further validates this theory (Leng and Edison 2021).

The biggest shortcoming of this hypothesis so far was the relative lack of efficacy in amyloid-targeting therapy. Despite the obvious involvement of amyloid aggregation in AD, the reduction of amyloid levels not always correlating with cognitive improvement and adverse side effects, such as brain swelling and haemorrhage remain the major pitfalls of anti-Aβ therapy (Lian et al. 2023; Zhang et al. 2023). However, recent FDA approval of three anti-Aβ monoclonal antibodies, lecanemab, aducanumab and donanemab, has reignited the hope in the potential of this therapeutic approach, albeit their efficacy in treating AD are yet to be fully defined (Cummings 2023; Sims et al. 2023). Despite several failed trials, other novel amyloid processing-targeting therapies, such as γ-secretase modulators and BACE-1 inhibitors are still being developed (Miranda et al. 2021).

The multiple pathological mechanisms affected by Aβ are the building blocks of more global interactions between the different cell types of the brain, such as neurons, astrocytes, microglia, oligodendrocytes and vascular cells, also known as the cellular phase (De Strooper and Karran 2016). Better understanding of the way these cell types interact could potentially unveil more therapeutic targets, providing alternative prospects in AD treatment.

1.3.2. Cellular phase: the complex relationship between brain cell types.

Neurons are undoubtedly the main brain cell type implemented in AD; their premature death and inability to maintain synapses is what ultimately leads to cognitive impairment. However, it appears that AD pathophysiology is also tightly linked to other brain cells – glial cells, which support normal neuronal function, and vascular cells, supplying the brain with blood, providing oxygen and nutrients. This scope and stage of AD pathology is referred to as the “cellular phase”.

Neurons are highly specialised cells, focused on the transmission of action potentials through changes in voltage and the release of neurotransmitter molecules. However, with this high degree of specialization comes a caveat: neurons heavily rely on glial cells to maintain their metabolism, signalling, transport, myelin sheath, and synapse formation modulation (Rasband 2016). Glial cells support the integrity of the BBB, allowing selective transport between the bloodstream and brain (Alvarez et al. 2013)(Figure 1.4). Furthermore, glia are the major enforcers of the immune system within the brain, regulating inflammation, and play a crucial role in clearing cellular debris and maintaining homeostasis.

Astrocytes are the most numerous glial cells, and are involved in synapse support, maintenance of neuronal activity, brain ion homeostasis, metabolic support of neurons, as well as formation and maintenance of the BBB (Figure 1.4). Essential for neuronal survival (Wagner et al. 2006), astrocytes convert the glucose from the bloodstream to lactate, which is subsequently transported to neurons, providing energy essential for their function (Bélanger et al. 2011; Tang et al. 2014). Astrocytes are sensitive to the change in their environment, and are readily activated by physical damage and biochemical cues, such as inflammation (Linnerbauer et al. 2020). In response to inflammation, astrocytes release cytokines, which initiate the immune response pathway, also attracting and activating microglia.

Microglia are the resident immune cell of the brain. Normally quiescent, they roam the cellular environment of the brain, responding to cellular debris, infectious pathogens and other pathological stimuli (Figure 1.4) (Hickman et al. 2013). When encountering their targets, microglia become activated, initiating phagocytosis and pro-inflammatory response (Rodríguez-Gómez et al. 2020). In context of AD, microglia are highly involved in clearance of Aβ deposits and initiating inflammatory response to the aggregates (Hickman et al. 2008). However, it appears that this pathway becomes highly dysregulated in AD, resulting in aberrantly-activated microglia mediating synapse loss and further neurodegeneration (Hong et al. 2016).

The activation of both of these cell types is thought to lead to aberrant pro-inflammatory pathway upregulation, ultimately leading to neuronal dysfunction and damage through harmful levels of cytokines and loss of trophic support (Figure 1.4) (Leng and Edison 2021). Interestingly, both microglia and astrocytes express high levels of Apolipoprotein-E (APOE), an apolipoprotein transporter, which has been established as the biggest risk factor for late-onset AD (LOAD) (Raulin et al. 2022). Whilst not directly involved in inflammation, this protein facilitates neuronal lipid transport and metabolism, another major pathway dysregulated in AD. To further understand the implications of APOE it is important to first characterise LOAD and how its pathology differs from familial forms of AD.

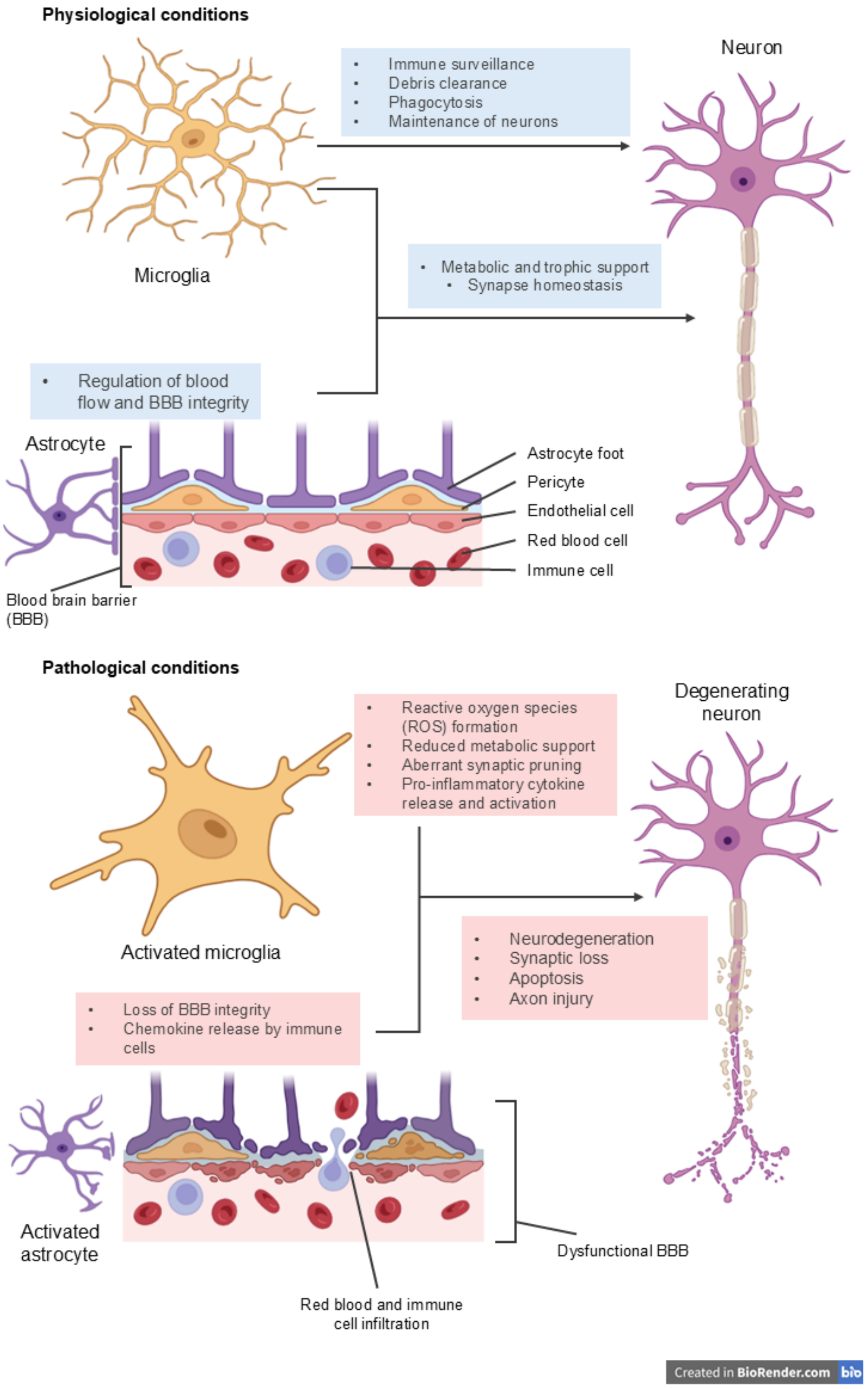

Figure 1.4. Function and pathology of glial cells in cellular phase of AD.
A brief overview of glial cell function at normal physiological conditions, such as regulation of blood flow and blood brain barrier (BBB) integrity support by astrocytes, enforcement of the immune system and surveillance by microglia, as well as the involvement of both cell types in trophic support of neurons and upkeep of synaptic homeostasis. Pathological challenge faced as a result of AD pathology renders these functions aberrant, leading to activation of glia, and subsequent pro-inflammatory cytokine release, disruption of BBB and loss of homeostatic neuronal support. As a result of these changes, axon injury is increased, as well as an increase in neuronal dysfunction, apoptosis and synaptic loss is observed Figure adapted from Leng and Edison (2021) and created using BioRender.com

1.4. Genetics of AD

1.4.1. Early and Late Onset AD

With accumulating evidence of multifaceted nature of Alzheimer's disease, it becomes clear that aetiology of AD is complex and most likely is a combination of several factors under certain conditions.

Two major forms of AD are distinguished: early-onset AD (EOAD) and late-onset AD (LOAD). EOAD, including the familial form of AD, is an autosomal dominant form of AD, which comprises only 5% of the total patient population. EOAD is usually caused by mutations in genes involved in amyloid precursor protein processing and lipoprotein metabolism, such as *APP*, presenilin 1 (*PSEN1*) and presenilin 2 (*PSEN2*) (Corder et al. 1993; Karch and Goate 2015; TCW and Goate 2017). Whilst *APP* mutations affect amyloid protein directly, *PSEN1*&*2* encode proteins integral in formation of presenilin, the catalytic subunit of γ-secretase. Consequently, mutations in both *PSEN1* and *PSEN2* lead to aberrant activity of γ-secretase, changing its preferred APP cleaving site, and thus increasing neurotoxic Aβ42 peptide production, altering the Aβ42/Aβ40 ratio (Li et al. 2016).

Trisomy 21, the causative factor of Down syndrome (DS), introduces another copy of *APP* and has been linked to a higher incidence of AD in individuals with DS (Potter et al. 2016). Whilst not traditionally classified as EOAD, DS-related AD incidence further highlights the involvement of amyloid in neuroinflammation and tau hyperphosphorylation observed in both EOAD and LOAD (Hof et al. 1995).

LOAD on the other hand, is sporadic, and is thought to be affected by several risk factors. AD risk factors can be classified as environmental and genetic. The environmental risk factors include alcohol consumption, smoking, several other diseases such as cardiovascular disease, type 2 diabetes mellitus, traumatic brain injury, depression and chronic sleep deprivation (Herrera-Rivero 2013). However, the biggest risk factor for LOAD remains age. Whilst mutations in *APP* or *PSEN1*/*2* are considered AD-causative factors, the newest genome-wide association studies (GWAS) discover multiple novel gene polymorphisms, that are thought to increase the genetic risk of developing AD. The recent technological advances have allowed for large scale genetic profiling, crucial for a heterogeneous disease like LOAD. GWAS is used to identify genetic variations associated with certain traits or diseases. It involves comparison of genomes between the diseased and healthy control cohorts (Uffelmann et al. 2021). These studies identify loci polymorphisms, that statistically differ between these populations and are suggested to be involved in the studied disease. To this date, GWAS have resulted in identification of 75 AD risk loci (Figure 1.5) (Bellenguez et al. 2022).

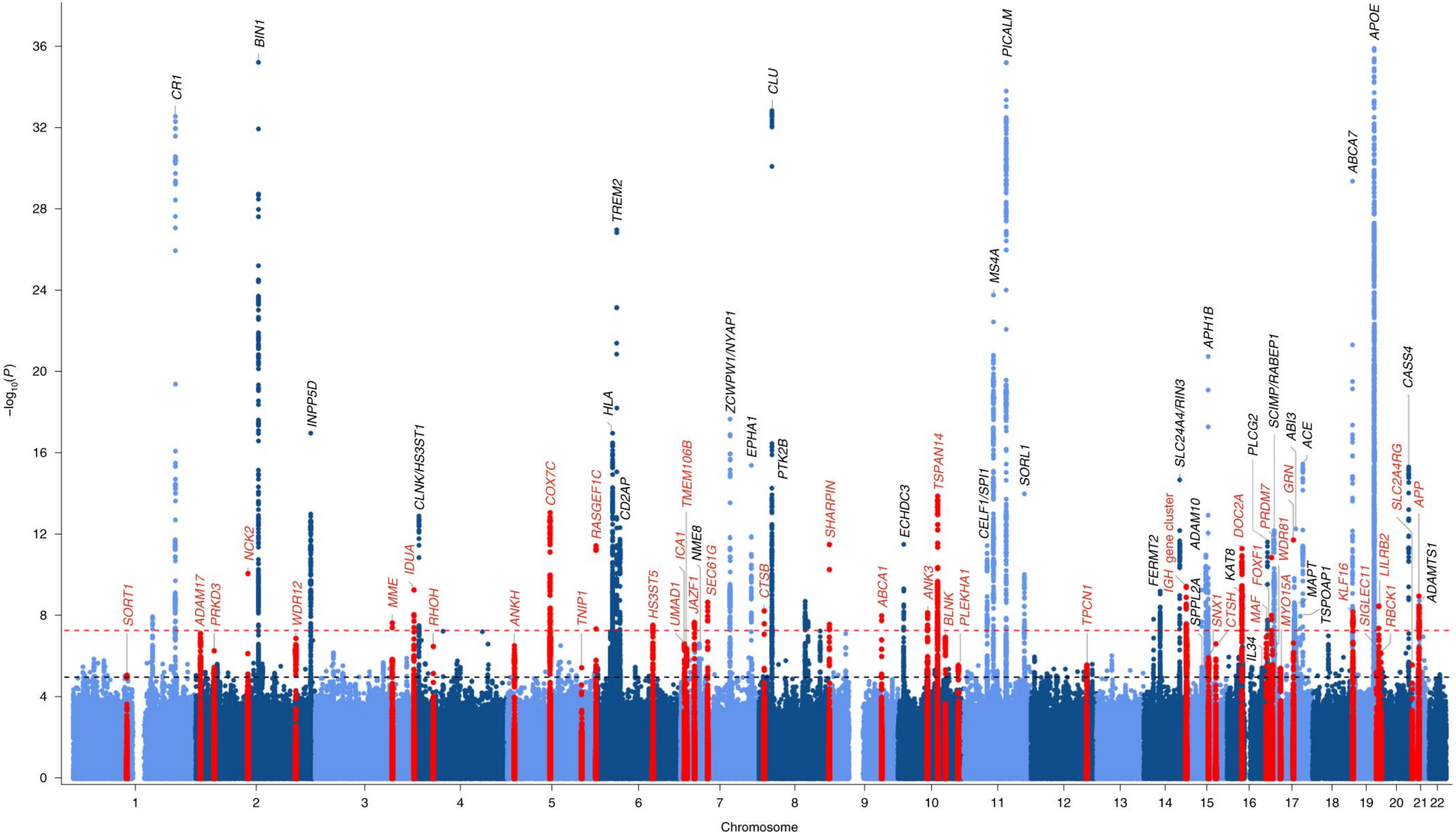

Figure 1.5. Latest LOAD GWAS study risk gene hits.
A Manhattan plot showing genome-wide statistically significant loci of late-onset AD (LOAD), with newly identified loci shown in red. Suggested significance threshold is marked by the black dotted line, whilst the genome-wide significance threshold marked by the red dotted line.
Figure taken from Bellenguez et al. (2022)

1.4.2. *APOEε4* in AD

APOEε4 was the first common variant linked to increased risk of developing LOAD, becoming a focal point of AD research, which it remains to this day.

APOE plays a crucial role in lipid metabolism, as well as cholesterol and phospholipid transfer in the brain (Liao et al. 2017). It facilitates it by binding high-density lipoprotein particles with their receptors, enabling their further endocytosis into the cells. In the brain, APOE is primarily expressed by astrocytes and microglia, with neurons being able to produce it under certain conditions, such as excitotoxic injury (Holtzman et al. 2012; Ioannou et al. 2019). In glia, APOE binds cholesterol and other lipid molecules, creating apolipoproteins which are then transported into neurons (Leduc et al. 2010) via low density lipoprotein receptor related protein 1 (LRP1, also known as CD91), a lipid molecule critical for neuron function (Liu et al. 2010). There, APOE plays an important role in cholesterol distribution for myelination and cellular membrane maintenance (Boyles et al. 1990). Recently, the APOEε4 isoform has been shown to cause dysregulated cholesterol accumulation in oligodendrocytes, the glial cells responsible for myelination of neuronal axons (Blanchard et al. 2022), further implicating its importance in neuronal cholesterol transport.

By the end of the 20th century, it was established that *APOE* isoforms can either increase the risk of developing of AD (namely *APOEε4*), or have a protective effect in patients (*APOEε2* and *APOEε3*) (Corder et al. 1993; Strittmatter and Roses 1996). These three isoforms are encoded by 2 single nucleotide polymorphisms (SNPs), with up to 25% of the population estimated to carry at least one allele of the *APOEε4* isoform (Roses 1996). *APOEε4* homozygosity has recently been identified as distinct form of LOAD, with almost all *APOEε4* homozygotes exhibiting some form of AD pathology (Fortea et al. 2024).

The pathogenic role of *APOEε4* still remains unclear, with studies showing conflicting results. The main notion suggest that APOEε4 has better binding affinity towards Aβ, however is less capable at carrying amyloid towards clearance within the cells, and possibly due to poorer lipidation of APOE4 (Kanekiyo et al. 2014; Fitz et al. 2021). Contrary to this, a seminal study of *APOE* knockout mouse models has shown that APOE is crucial for amyloid plaque formation, with close to none plaques forming in mice deficient in APOE (Bales et al. 1997). Considering these apparent discrepancies of APOE function between different variants and stimuli, it is important to take a closer look at the role of APOE in glial cells specifically and what effect it has on their lipid homeostasis. Interestingly, there is accumulating evidence of APOE involvement in lipid homeostasis dysregulation in microglia, which has become a forefront of current research in this field of AD pathophysiology.

1.5. Microglial lipid accumulation in AD

1.5.1. Microglia in AD

Microglia, the resident immune cells of the brain, normally quiescent, provide the first line of defence against pathogenic factors. Being extremely sensitive, any damage or pathogenic agent results in their activation and subsequent elimination of the lesion via phagocytosis and inflammation cascade initiation. It has been shown that microglia might play a significant role in AD, with activated microglia showing a significant association with the disease aetiology (Figure 1.6) (Leng and Edison 2021). Microgliosis, an aberrant inflammatory response of microglia, appears to be to harness a dual effect on AD progression (Hansen et al. 2018). Accumulating and colocalising with senile plaques and NFTs (Serrano-Pozo et al. 2011), microglia are capable of clearing the aggregates through phagocytosis (Figure 1.6), however, their abnormal activation also leads to synapse loss and neurodegeneration (Hong et al. 2016). Microglial activation has been recorded prior to detection of Aβ and tau biomarkers in AD patients, suggesting an early involvement of microglial dysregulation in AD pathophysiology (Parbo et al. 2018). Increasing evidence of microglial gene involvement in AD (Jones et al. 2010; Bellenguez et al. 2022), many of which are also somehow involved lipid homeostasis, has created a standpoint in AD research – how are microglia involved in this lipid regulation and what does go wrong?

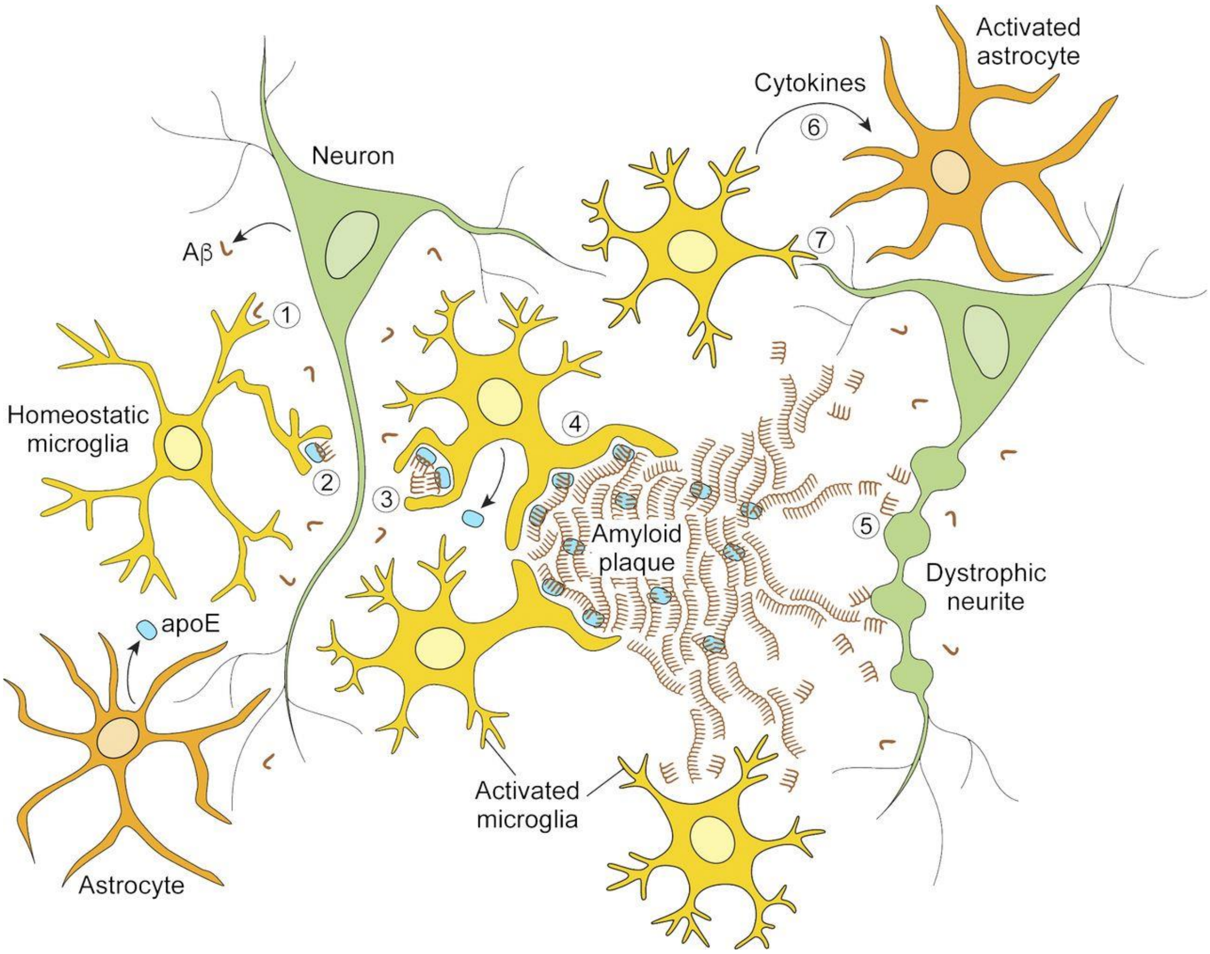

Figure 1.6. Microglial role in Aβ-related pathology in AD.
Microglia are capable of clearing free extracellular Aβ peptides (1), APOE-bound Aβ (2), as well as small Aβ aggregates (3) through phagocytosis. Activated microglia colocalise with the amyloid plaques (4) in attempt to contain them and preventing them from neuronal damage (5). Activated microglia initiate pro-inflammatory cytokine release (6), activating astrocytes and initiating immune response, which negatively affects neuronal synapses and axons, promoting their loss (7).
Figure taken from Hansen et al. (2018).

1.5.2. Lipid Droplets in AD

Recent studies in the field indicate that microglia possibly play a neuroprotective role in AD by sequestering reactive oxygen species from neurons through lipid droplet shuttling. Lipid accumulation in glial cells surrounding amyloid plaques was initially described by Alois Alzheimer in his seminal study (Stelzmann et al. 1995), however, lipid homeostasis dysfunction in AD has only recently become a topic of scientific interest.

Lipid droplets (LDs) are small organelles, used for storage of lipids, quintessential macromolecules, used in a variety of cellular mechanisms, such as maintenance of cellular membrane integrity, energy metabolism, production of hormones and other lipid-derived molecules (Pol et al. 2014). Lipid droplets are composed of two distinct parts: the hydrophobic core, containing triglycerides and cholesterol esters, and the outer single phospholipid layer, incorporating cholesterol and LD-associated proteins (Meyers et al. 2017; Farmer et al. 2020). Varying in size from 0.1-5 µm in non-adipocytes, LDs are able to split or merge together, allowing for fine-tuning of lipid storage needs of the cell (Fujimoto and Parton 2011; Onal et al. 2017). In the microglia, LDs appear to accumulate with age (Marschallinger et al. 2020), and in response to inflammation (Farmer et al. 2020). However, the potential use of LDs as a neuroprotective mechanism of reducing oxidative stress in neurons appears most interesting in context of AD pathophysiology.

Reduced lipid transport capacity between microglia and neurons, displayed by APOEε4 compared to other isoforms, is hypothesized to be a major factor in the development of AD-related in reactive oxygen species (ROS) and mitochondrial defect damage in neurons (Liu et al. 2017; Moulton et al. 2021). Earlier, Liu et al. have established a link between ROS levels and formation of LD in Drosophila and mouse neurodegeneration models (Liu et al. 2015). The study has shown a correlation between increased ROS levels and LD accumulation, as well as neuroprotective effects of decreasing ROS levels, delaying neurodegeneration and reducing the production of LDs (Figure 1.7). Increased lipid production via c-Jun N-terminal kinase/sterol regulatory element-binding protein (JNK/SREBP) and lipid peroxidation was identified as a key mechanism in transferring the oxidative stress onto LDs (Figure 1.7, Figure 1.8) (Liu et al. 2015). Furthermore, neurons were shown to intrinsically produce LDs under oxidative stress, which are subsequently transported to surrounding glia (Ralhan et al. 2023). Interestingly, it has recently been shown in *Drosophila* that neuronal mitochondrial dysfunction and its subsequent oxidative damage leads to senescence in glial cells, promoting lipid accumulation first in senescent and then in non-senescent glia (Byrns et al. 2024). Similarly to amyloid pathology, LD accumulation in glia has also been shown in tauopathy, accompanied by pro-inflammatory signalling and a decrease in phagocytic activity (Li et al. 2024).

Most recent findings using *Drosophila* models suggest that this mechanism of LD trafficking is carried out at night and is highly dependent on the sleeping cycle (Figure 1.7) (Goodman et al. 2024; Haynes et al. 2024). It is hypothesised that the highly metabolically active neurons accumulate ROS during wake, which are then shuttled to glia, and catabolised during sleep (Haynes et al. 2024). Interestingly, this transfer of LDs was shown to rely on *Drosophila* APOE orthologues – neuronal and glial Lazarillo (NLaz and GLaz), potentially unveiling yet another function of this principal AD risk gene. The effects of sleep deprivation and extended wake on brain oxidative stress homeostasis is particularly interesting, considering sleep disorders are one of the characteristic symptoms of AD (Brzecka et al. 2018).

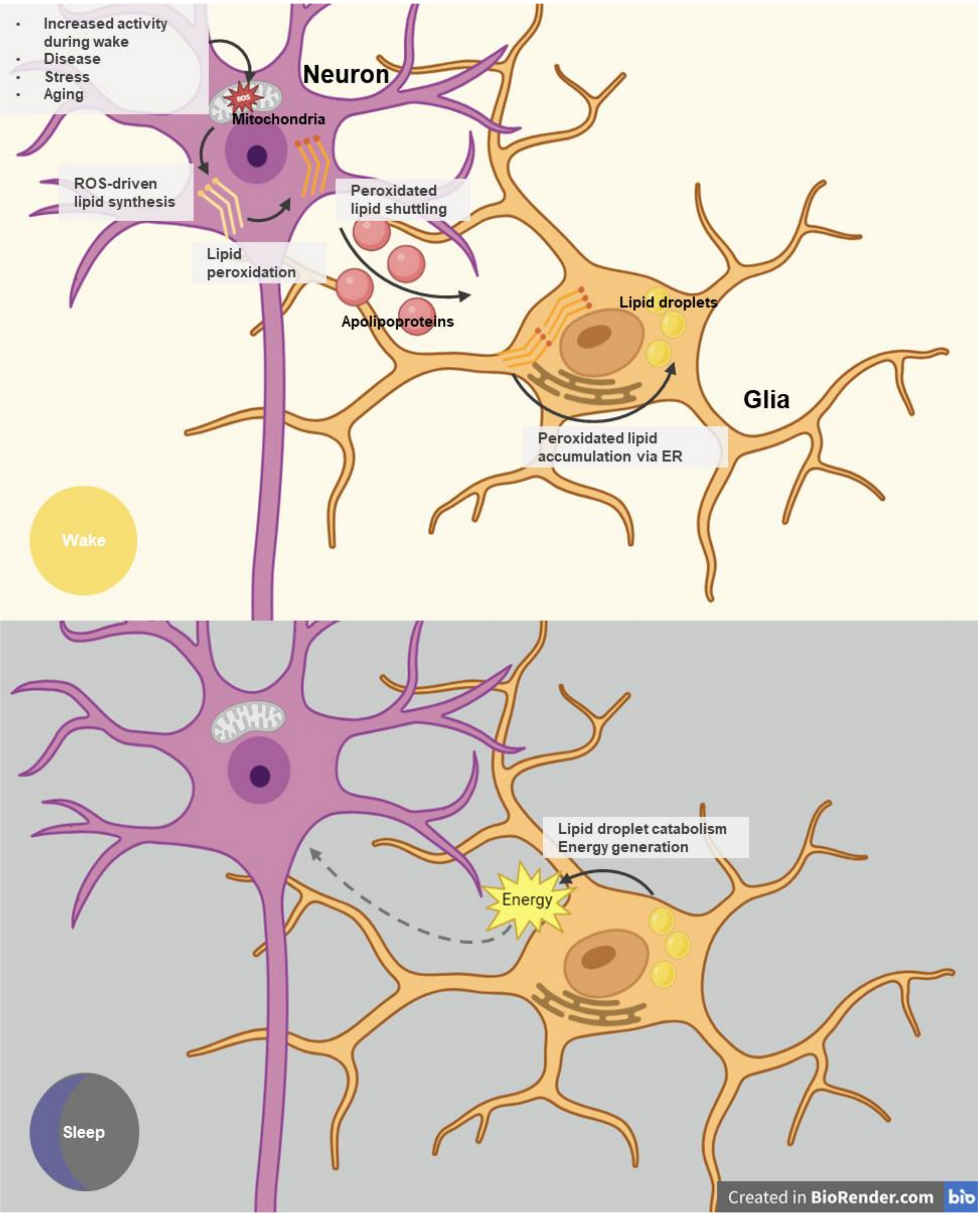

Figure 1.7. Proposed model of ROS-protective LD droplet shuttling along the neuron-glia axis. Neuronal mitochondria produce reactive oxygen species (superoxide and hydroxide radicals, hydrogen peroxide) as a response to ageing, increased activity during wake and mitochondrial dysfunction. These increase in ROS upregulates lipid synthesis, with lipids then binding and neutralising ROS, creating peroxidated lipids. The peroxidated lipids are then shuttled from neurons into glia via APOE and sequestered into lipid droplets. During sleep, the glia metabolise LD, creating energy and resolving the oxidative stress.

Figure adapted from Goodman et al. (2024) and created using BioRender.com.

Other lipid transport related proteins, namely adenosine triphosphate-binding cassette transporters 1&7 (ABCA 1&7, respectively), previously identified as AD risk genes in GWAS, have been shown to play a crucial role in this process, disruption of which leads to neurodegeneration (Figure 1.8) (Moulton et al. 2021). Moulton and colleagues have used the *Drosophila* retina model to show that neuronal expression of *ABCA1/7* fly orthologues *Eato* (Engulfment ABC Transporter in the ovary) and *Idd* (lipid droplet defective) plays a crucial role in LD transfer from neurons to glia, by preventing the glial LD formation when knocked down by RNAi. Additionally, deletion of *Abca1* was previously shown to cause Aβ accumulation and decreased lipidation in mice (Wahrle et al. 2005).

The researchers identified other genes as key in this pathway, that have also previously come up in AD GWAS, such as fly orthologues of *PICALM*, *CD2AP*. APOE receptor LRP1 and subunits of the retromer complex, which have long been thought to play a role in AD aetiology (Small and Petsko 2015; Shinohara et al. 2017), were also identified to be involved in this pathway (Figure 1.8). ABCA1 agonists restore glial LD formation in humanised APOEε4 flies to levels such of protective APOEε2 and neutral APOEε3 (Moulton et al. 2021). This provides insight into a potential mechanism of neuroprotection against ROS hallmark of AD (Goodman and Bellen 2022).

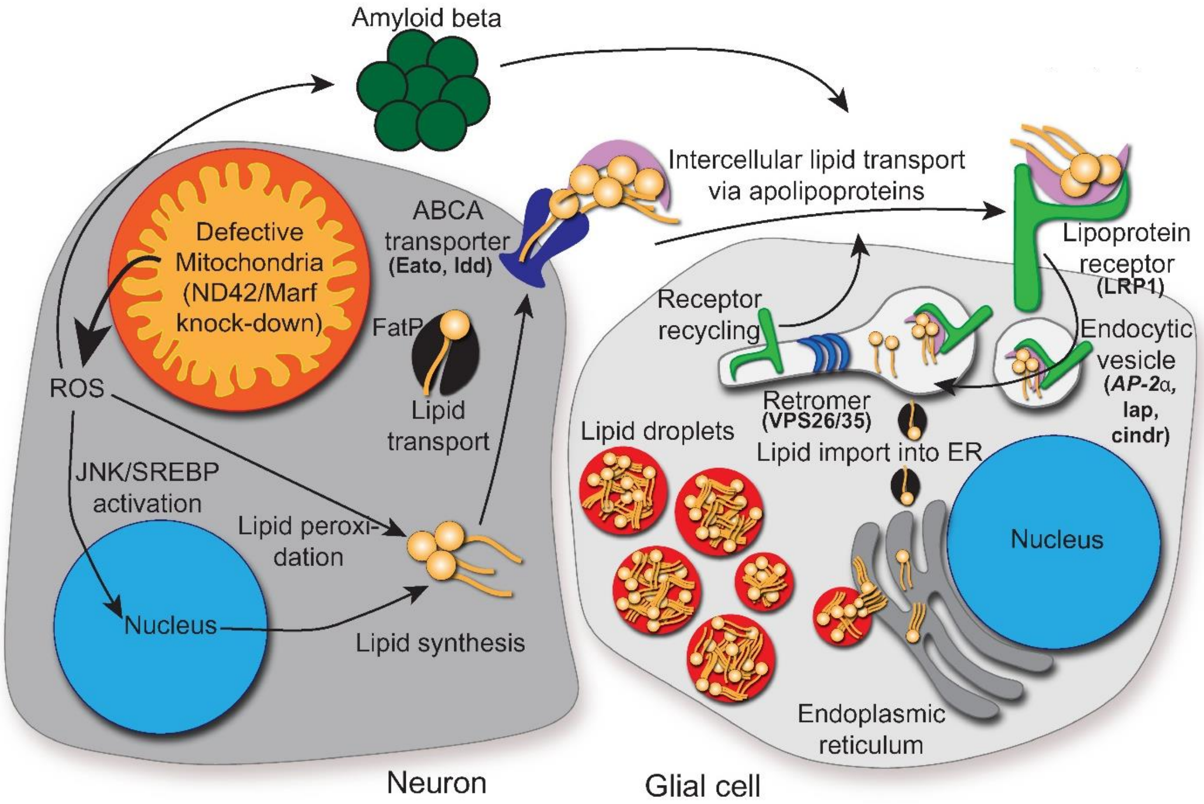

Figure 1.8. Molecular pathway of neuronal lipid transport into *Drosophila* glia.
Mitochondrial stress and dysfunction lead to increase in ROS and activation of the c-Jun N-terminal kinase/sterol regulatory element-binding protein (JNK/SREBP) pathway, resulting in increased lipid synthesis. The created lipids then undergo peroxidation by ROS and are shuttled outside of neurons via ABCA transporters (Eato *and* Idd in *Drosophila*) and apolipoproteins (no direct analogue to APOE in *Drosophila;* distinct neuronal and glial apolipoproteins instead). These lipids are then received by the lipoprotein receptor (LRP1 in *Drosophila*) and recycled through the endocytic retromer pathway, creating lipid droplets in glia. All *Drosophila* protein names in bold are orthologues of human GWAS AD-associated risk genes. Amyloid beta has been shown to synergise with this pathway, further facilitating production of glial LDs.
Figure taken from Moulton et al. (2021)

Interestingly, there is growing evidence that the LD transport from neurons to microglia is potentially detrimental to microglial activity. APOEε4 induced pluripotent stem cell (iPSC) microglia have recently been shown to undergo triglyceride lipid synthesis in response to fibrillary Aβ peptide toxicity, through an upregulation of ACSL1 (Haney et al. 2024), an important player in cholesterol and lipid metabolism (Wu et al. 2022). Haney and colleagues have also discovered that media conditioned by microglia containing excess LDs induced increased tau phosphorylation and caspase activation in APOE iPSC neurons, further underlining the interaction between these cell types in disease progression. Furthermore, it has been previously shown that microglial LD accumulation impairs their surveillance function (Victor et al. 2022), as well as renders them dysfunctional and puts them in an proinflammatory state (Marschallinger et al. 2020). This dysfunction can potentially be linked to the correlation between LD accumulation and decrease in phagocytosis in iPSC microglia expressing GWAS AD risk variant of PICALM (Duan et al. 2024), and reported phagocytic dysfunction in tau-related LD accumulating microglia (Li et al. 2024). Additionally, ACSL1 inhibition was previously reported to aid APOEε4 microglia to take a less LD-burdened homeostatic state, similar to APOEε3, dramatically reducing LD accumulation and restoring microglial surveillance (Victor et al. 2022).

Beyond microglia, APOEε4 regulation of lipid homeostasis appears to impact AD through astrocytes. It has been reported that APOEε4 isoforms impair fatty acid metabolism and transport between neurons and astrocytes, hindering the ability of the latter to eliminate excess lipids from neurons (Qi et al. 2021). Astrocytic APOEε4 has been shown to drive BBB impairment, a hallmark of AD cellular pathophysiology phase (Bell et al. 2012; Jackson et al. 2022). Glucose metabolism activity and mitochondrial respiration are also negatively affected by APOEε4 in astrocytes, hindering their metabolic support of neurons (Lee et al. 2023). Cholesterol depletion, however, has shown to restore this dysregulation, further hinting at the lipid homeostasis implication in AD.

These seemingly varied effects raise a question: what is the actual impact of neuron-glia lipid transport axis on aetiology of Alzheimer's disease? Is it specifically neuroprotective, harmful to surrounding microglia, or perhaps, a combination of both? To answer this question, a more in-depth understanding of lipid biology and its dysfunction in AD is required, referring us to the currently available models of AD research, which could potentially help us find the answer.

1.6. Models of Alzheimer’s Disease – why the fly?

Contemporary research models of AD simulate the disease by modulating already known neuropathological hallmarks of AD, such as amyloid beta plaque formation NFTs. A wide range of model types and organisms are available for AD research, ranging from human iPSC 2D and organoid cultures (Arber et al. 2017; Sharma et al. 2021), to non-transgenic animal models such as primates and dogs (Sarasa and Pesini 2009). This variety of available disease models allows us to use their unique strengths and weaknesses to investigate certain aspects of the disease, as well as compare our findings between varying models for validation. In this project, we have delved into creating a novel *Drosophila melanogaster* model for studying lipid droplet dysregulation observed in AD.

Drosophila melanogaster, commonly known as the fruit fly, has now been the choice model system for genetic experimentation by many scientists for over a century. *Drosophila* research has massively contributed to our understanding of neurodevelopment, leading to discoveries such as homeotic genes, Notch signalling pathway, neurogenesis, and many others (Bellen et al. 2010). With around 70% of human disease-related genes conserved in *Drosophila* (Fortini et al. 2000) and its genome fully sequenced (Adams et al. 2000; Myers et al. 2000), fruit flies became an essential model for studying genetics. The continuous development of genetic manipulation toolkit, a short lifespan, and a surprisingly high degree of conservation with human genome turned flies into a favoured model in research beyond neuroscience.

With just under around 200,000 neurons (Dorkenwald et al. 2023), and a range of distinct glial cell types (Freeman 2015; Kim et al. 2020) within their brains, fruit flies provide an excellent model for studying AD. A relatively short lifespan of around 3 months allows exploring AD aetiology at different life stages of a fly. Having an organism with an intact and diverse, yet easily manipulatable nervous system, allows us to study cell interactions both *in vitro* and *in vivo*, something that cell culture models are yet to fully achieve. Furthermore, this comes at a fraction of price and time, when compared to rodent models. Although, despite the relatively conserved genome, *Drosophila* are invertebrate and lack the exact analogous vertebrate glial cell types, with a nervous system less complex than of humans.

Several binary gene expression systems are available in *Drosophila*, allowing easily accessible spatiotemporal expression of transgenes of interest in any tissue, possibly the strongest feature of fruit flies as a versatile research model. Established in 1993 (Brand and Perrimon 1993), Gal4-UAS has become the most used system with tens of thousands transgenes lines available for purchase. This expression system function consists of the following machinery: tissue-specific promoter expresses a transcription activator protein

(Gal4), that binds to an expression enhancer (effector) (UAS), resulting in activation of transgene transcription (Rodríguez et al. 2011) (Figure 1.10A). Other frequently used expression systems are lexA/lexAop (Lai and Lee 2006), Q-system (QF/QS) (Potter et al. 2010), tTA/TRE (Bello et al. 1998), which follow the same principle (Figure 1.10B). Some systems also allow for transcription repression by specific molecules, such as Gal80 and QS, adding a temporal aspect to transgene expression (Figure 1.10A). All mentioned systems act independently, which creates possibility for multiple transgene expression and different tissue types. A dual binary expression model of Gal4-UAS/Q-system has been previously reviewed (Riabinina and Potter 2016) and will be utilised in the experimental design of this report.

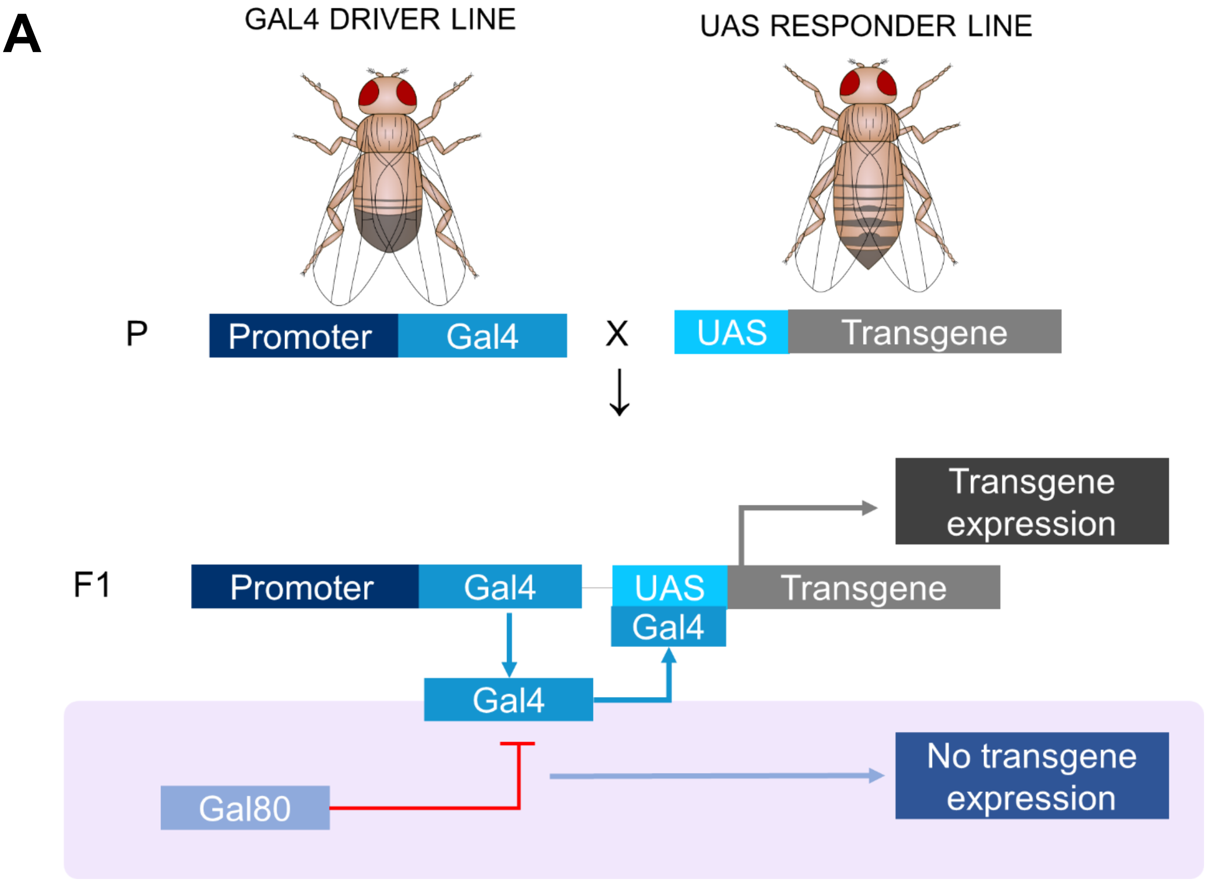

B

System	Transcriptional activator (reporter)	Effector	Suppressor of activator
Gal4/UAS	Gal4	UAS	Gal80
Q-system	QF	QUAS	QS
LexA/LexAop	LexA	LexAop	N/A
tTA/TRE	tTA	TRE	Tet

Figure 1.9. *Drosophila* binary gene expression system schematic.
A) Gal4/UAS expression system. The transcriptional activator (reporter, promoter) Gal4 is expressed in a cell-specific manner, where it then binds the effector UAS, resulting in activation of transgene expression. This process can be inhibited by suppressor of activator Gal80, resulting in ablation of transgene expression. Some systems, like Gal4/UAS have suppressors of suppressors, which in Gal4/UAS system is temperature. **B)** Table of other frequently used expression systems and their respective machinery.

Current fly models of AD are mostly based on expression of peptides that drive AD, such as Aβ42 or mutant tau, as well as disrupting mechanisms protecting from amyloid build-up (mutant *PSEN1/2*) (Jeon et al. 2020). *Appl*, the fly homologue of human *APP*, does not contain a well-conserved Aβ sequence (Luo et al. 1992; Preat and Goguel 2016), nor does fly *BACE1* orthologue have the same cleaving activity as the human secretase (Carmine-Simmen et al. 2009). Despite Aβ-like peptides reported in senile flies (Carmine-Simmen et al. 2009), this means that human Aβ42 fragments must be inserted into *Drosophila* via transgenes, usually as genetic code for the peptide itself, or coding DNA for human *APP* and *BACE1*.

Utilisation of fruit fly models when studying neurodegeneration traditionally consists of behavioural tests, such as sleep, locomotion, and memory assays, as well as tissue staining and imaging, most often performed with their brain tissue (Hirth 2010). Fly retinae have also been used to investigate the effects of neurodegeneration, as they provide an identifiable degenerative “rough eye” phenotype, an excellent neurodegeneration indicator (Iyer et al. 2016). Furthermore, the fly retinae are also made of just under a thousand of facets - ommatidia, each one of which is composed of several photoreceptors and glial supporting cells (Prüßing et al. 2013b; Cutler et al. 2015). This feature makes *Drosophila* an exceptional model for studying interaction between neurons and glia in AD, which has been utilised in recent publications on the topic (Liu et al. 2015; Liu et al. 2017; Moulton et al. 2021). However, both fly brains and retinae are extremely small and difficult to dissect, significantly slowing impact the duration of experiments and cohort sample size.

1.7. Fly wings as a new model of lipid homeostasis in AD.

Considering the gap in the literature at the time of writing this report, I have determined to create model of AD allowing to study lipid droplet homeostasis dysfunction, as well as including an option for genetic modification to assess involvement of AD risk genes on lipid droplet formation. Fly wings were picked as a suitable and easily accessible tissue. A bundle of sensory neurons run along two (L1 and L3) of the five veins of each wing, wrapped and integrated with supporting glial cells (Murray et al. 1984). This close proximity allows for studying the interaction between these two cell types, highly implicated in AD. *Drosophila* possess astrocyte-like cells, which closely resemble their vertebrate orthologues (Ma et al. 2016), however they do not have oligodendrocyte and microglia counterparts (Freeman 2015; Yildirim et al. 2019; Kim et al. 2020). Nonetheless, the ensheathing glia of *Drosophila* appear to most closely mimic microglial phagocytic activity (Doherty et al. 2009), and have more recently been shown to facilitate amyloid clearance and aggregate LDs, similar to vertebrate microglia (Sheng et al. 2023).

These characteristics of the fly wing and the flexibility of *Drosophila* have ultimately led to an establishment of a novel model for studying effects of lipid homeostasis on AD progression. The model, which utilises two expression systems, allows for a more refined spatiotemporal gene expression, allowing to more precisely mimic AD aetiology and the complex cell type interplay, which becomes more apparent in driving the disease.

1.8. Aims and hypotheses

In this project I have developed a model of analysing lipid droplet dysfunction in AD. Approaches to establish and validate this model were as follows:

1. To characterise and validate use of fluorescent reporter for LD accumulation in an accessible neuronal wing tissue as a tool of studying lipid biology dysfunction glia.
2. Investigate whether the LD phenotype displayed by LD-GFP can be altered through genetic alteration and mechanical injury.
3. To create a double expression system model of AD, allowing LD-GFP expression in glia, alongside Aβ42 expression in neurons. Aβ42 expression needs to be confirmed and its effect on fly longevity assessed.

Hypothesis: *Drosophila* wing is a reliable and malleable model to recapitulate glial LD accumulation in response to Aβ42 accumulation and neuronal injury.

1.9. Experimental design

The proposed model utilises two parallel but independent binary gene expression systems, which will be referred as “dual binary” throughout. Furthermore, I sought to investigate a wing screen for LD changes could be established with the dual binary model. I used a GFP-tagged LD-binding domain of the LD motor regulator protein *klarsicht* (*klar)* which has been previously established and described (Yu et al. 2011). Using this fluorescent marker with *Drosophila* wing imaging provides several advantages when compared to classic AD tissue imaging approaches, such as larval and adult brain imaging. Unlike the central brain, fly wings do not require tedious dissection and fixing processes and are ready to be imaged straight after collection. With readily established protocols for axon imaging (Vagnoni and Bullock 2016; Paglione et al. 2020), I have set to try and visualise LDs in glia that surround these axons. However, the neurons harboured in the fly wing belong to the peripheral nervous system (PNS), rather than central (CNS), like the brain neurons, thus might slightly differ in their fundamental biology. Nonetheless, the dual binary nature of the model would allow us to investigate the changes in glial lipid biology in response to neuronal amyloid toxicity, a frequently emerging topic of AD. Considering the described vertebrate-invertebrate glial discrepancies, a pan-glial driver *Repo* was chosen, thus looking at all glial *Drosophila* cells. Ultimately, this model could provide a useful tool for lipid biology research, specifically addressing its involvement in AD aetiology.

2. Materials and Methods

Manufacturers and identifiers (where applicable) for laboratory consumables and chemical supplies are listed in the Appendix I.

2.1. *Drosophila melanogaster* Husbandry

2.1.1. Stock maintenance

Drosophila stocks were maintained at room temperature in plastic vials containing Cornmeal-Molasses-Yeast (CMY) media (Table 2.1). Stocks were maintained by transfer to a vial with fresh media every 3 weeks. Experimental flies were kept in an incubator at 25 °C in a 12:12 light dark cycle and transferred to a fresh media every 2-3 days. For selection, genotyping, and collection, flies were anesthetised on a CO_2 pad (Diffuser Pad, Genese Scientific) and examined under a light microscope (Stemi 508, Zeiss), handled, and moved with paintbrushes.

Table 2.1. Cornmeal-Molasses-Yeast (CMY) media ingredients

Product	Amount per litre
Water	746 ml
Agar	~7 g
Yeast	23.3 g
Cornmeal	58.1 g (+ additional 186 ml of water)
Molasses	58.1 ml
Ethanol (Pure, 99.8%)	6.5 ml
Tegosept	1.3 g
Propionic acid	1.6 ml
Phosphoric acid	162.8 µl

2.1.2. Fly Stocks

Stocks, including their genotype and stock number, used for the experiments are listed in Table 2.2. Stocks were purchased from Bloomington Drosophila Stocks Centre (BDSC), Vienna Drosophila Resource Centre, or were sourced from the in-house stock collection.

Table 2.2. Fly stock list

Line	Genotype	Stock number
aos::Aβ42^{Arc} II	y[1] w[1118]; P{w[+mC]=UAS-APP.Abeta42.E693G.VTR}4	BDSC #33773
aos::Aβ42^{Arc} III	w[1118]; P{w[+mC]=UAS-APP.Abeta42.E693G.VTR}8	BDSC #33774
Double balancer	w^{-};Sp/CyO;Dr/Tm3	In house stock
LacZ II	w^{-}; LacZ/CyO; +/+	Sheppard lab
LacZ III	w^{-};+/+; LacZ/Tm3	Sheppard lab
LD-GFP (*klar*-GFP)	w^{-}; Avic\GFP$^{klar.LD.UASp}$; +/+	Welte Lab (Yu et al. 2011)
nSyb-QF2	y[1] w[1118]; P{y[+t7.7] w[+mC]=nSyb-QF2w.P}attP2	BDSC #51960
mCD8::GFP	y[1] w[*]; P{w[+mC]=UAS-mCD8::GFP.L}LL5, P{UAS-mCD8::GFP.L}2	BDSC #5137
mCD8::tdTomato	w^{-};QUAS-mCD8::tdTomato/CyO;+/+	In house stock
QUAS-Aβ42	w[1118]; P{w[+]=QUAS-Abeta42.L}4	BDSC #83347
QUAS-LacZ	y[1] w[1118]; P{w[+mC]=QUAS-nuclacZ.P}44	BDSC #30007
Repo-Gal4	w[1118]; P{w[+m*]=GAL4}repo/TM3, Sb[1]	BDSC #7415
w^{1118}	w[1118]	BDSC # 3605
attP-pJFRC2	w^{-};+/+;UAS- P{pJFRC}attp2/Tm3	In house stock
attP-PJFRC40	w^{-}; UAS-P{pJFRC}attp40/CyO;+/+	In house stock
Draper RNAi	w1118; P{GD14423}v27086	VDRC #27086
Draper OE	y[1] w[*]; P{w[+mC]=UAS-drpr.I}2	BDSC #67035

2.1.3. Binary systems

Two binary gene expression systems were used in this project: Gal4-UAS and QF2-QUAS. Both systems contain a cell-specific promoter that drives expression of transcription activator, and an enhancer, which the activator binds to, resulting in expression of protein of interest. Gal4-UAS system was utilised for RNA interference (RNAi) experiments with Aβ42 background, as well as most of tool and transgene overexpression (Figure 1.10A). QF2-QUAS system was used for building the dual binary model of Alzheimer’s disease, by overexpressing Aβ42 peptide in neurons using nSyb-QF2 promoter (Figure 2.1).

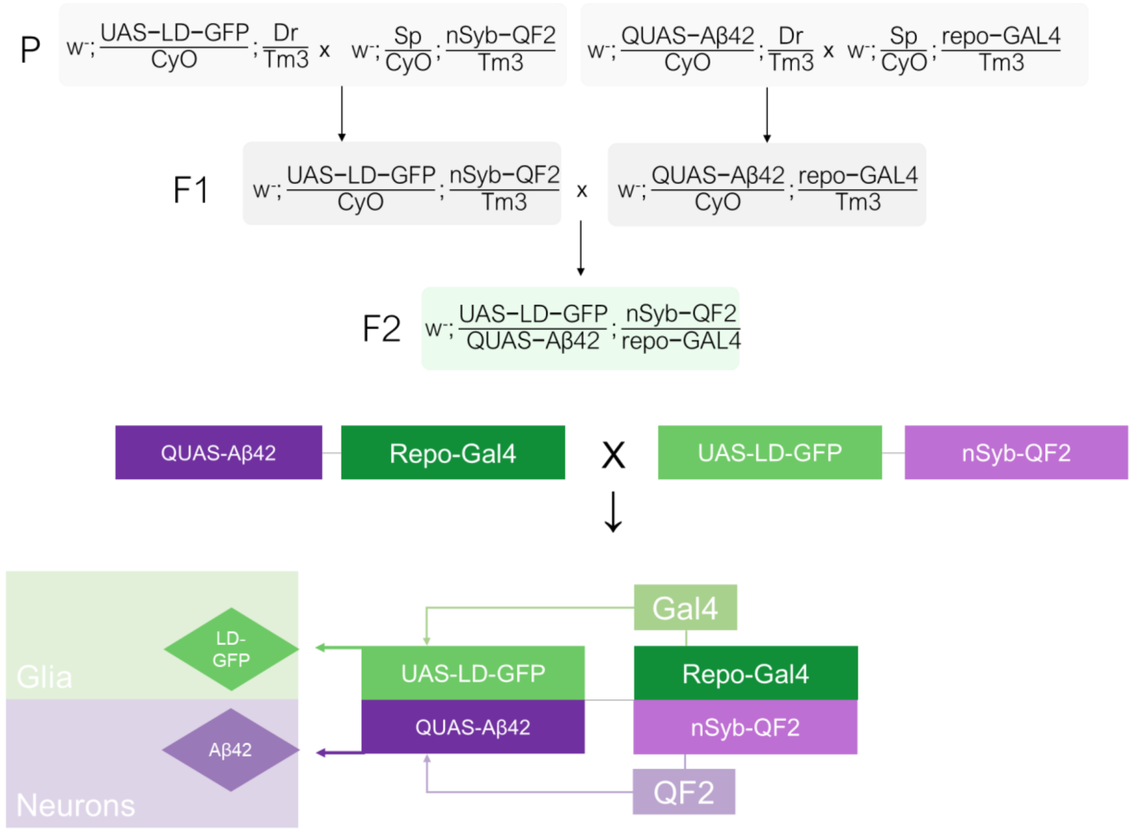

Figure 2.1. Dual binary cross and gene expression scheme.
Scheme of crosses performed to create dual binary system flies. The dual binary system utilises two gene expression systems, which in this case are Gal4-UAS and the Q-system (QF2-QUAS). Q-system works similarly to Gal4-UAS system, comprised of a QF/QF2 cell type specific promoter and QUAS binding site. Here, Gal4-UAS system is utilised to express LD-GFP in glia via Repo-Gal4, and Q-system is utilised to express Aβ42 peptide in neurons. The two systems work independently, thus allowing for two different cell type-specific expression of transgenes to occur at the same time.

2.2. *Drosophila* Assays

2.2.1. Longevity assay

For survival experiments, fly crosses were set bottles with CMY media and kept at 25 °C for 10 days, removing parent flies on day 7. The collection of experimental flies the next 10 days. The flies would be collected into narrow media tubes, varying between 10 to 20 flies per tube. A total $n \geq 50$ was collected for each genotype and condition. The experimental flies were then transferred into a tube with fresh media every 2-3 days (Mon/Wed/Fri), and the dead flies were quantified and recorded for subsequent analysis. Male and female flies were separated to account for potential impact of sex differences on survival.

2.2.2. Wing collection

For fly wing collection, experimental flies were anaesthetised on a CO_2 pad and examined for wing injuries under a dissection microscope. Flies with injured, crinkled, or deformed wings were discarded. Medical forceps and scissors were used for wing dissection: the forceps were used to gently squeeze the fly, resulting in the dorsal protraction of the fly wings, allowing to cut the wing with the scissors as close as possible to the thorax. A thin line of halocarbon oil was spread on a microscopy slide. with a paintbrush, where around 10-20 wings were placed, lined horizontally, and oriented facing the same direction. The wings were then coated with another layer of oil and covered with a cover slip to be imaged. The flies were then discarded into the fly morgue, containing 70% ethanol. Both male and female flies were pulled together into same cohorts in equal numbers, as no visible difference in wing biology was observed throughout the experiments.

2.2.3. Wing mechanical injury

For mechanical injury experiments fly wings were handled similarly to regular wing experiments and examined for damage. 7 days post eclosion (DPE) was used as a standardised injury timepoint. Left wings were chosen for mechanical injury, with right ones kept intact, serving as an internal control. Left wing tips were pinched down with forceps and gently straightened out using the blade of a scalpel. The blade was positioned on the wing, using the reflection from the blade to ensure the cut was performed at the region where longitudinal vein 1 (L1) merges into the distal edge of the wing (Figure 2.2). The flies were then placed into a fresh media tube, which was stored horizontally for 48 h, unless stated differently. At 48 h, both experimental and control wings were cut and mounted as described previously. After wing collection, the flies were discarded into the fly morgue.

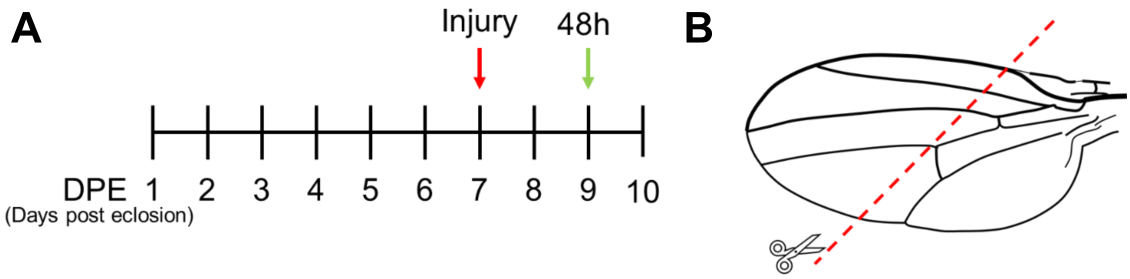

Figure 2.2. Injury experiment schematic.
A) Timescale for injury and imaging, **B)** Schematic of wing anatomy. Red dotted line represents the region where scalpel cut was performed.

2.3. Molecular Biology

2.3.1. Genomic DNA Extraction

DNA extraction buffer was used to extract gDNA for PCR genotyping. The flies were placed in Eppendorf tubes at -20 °C for 5 min and then pulverised in 50 µL of DNA extraction buffer (25 mM NaCl, 10 mM Tris-Cl, 1 mM EDTA), followed by the addition of another 100 µL of the buffer. 1 µL (4 µg/ml) of Proteinase K was added to the tubes, which were then incubated at 37 °C for 1 h, followed by an incubation at 85 °C for 10 min to deactivate the enzyme.

2.3.2. Polymerase Chain Reaction

Extracted gDNA was used for Polymerase Chain Reaction. The reagents added to each gDNA template were as shown in Table 2.3. The samples were then vortexed, spun down and placed into the thermocycler to undergo PCR. The reaction typically consisted of an initial denaturation step at 95 °C (1 min), 30-35 cycles of DNA expansion (30 s at 95 °C, 15 s at primer annealing T°, and 30 s at 72 °C) and final extension at 73 °C (5 min). Primers used for PCR are listed in Table 2.4.

Amplification of QUAS-Aβ42 insertion for Sanger sequencing was performed using PCR Protocol for Phusion® High-Fidelity DNA Polymerase. Primers for Hsp70 and Sv40 were used, as they flank the transgene insertion site on the QUAS plasmid (Table 2.4). The reaction and the thermocycler were set up according to manufacturer instructions, adding 1 µl of extracted gDNA.

Table 2.3. PCR reagent mix.

Product	Per rxn
Taq	12.5 µl
Forward primer(s)	2.5 µl
Reverse primer(s)	2.5 µl
Nuclease free H_2O	5.5 µl
Template	2 µl
TOTAL:	25 µl

Table 2.4 Primer pairs

Primer Name	Sequence	Tm (°C)	Product Size
Aβ42-F	CCGACATGACTCAGGATATGAA	54	100 bp
Aβ42-R	GCCCACCATGAGTCCAAT	56	
Hsp70-F	GAGCGCCGAGTATAAATAGAG	53	N/A
Sv40-R	CCATTCATCAGTTCCATAG	48	
QUAS-Aβ42 F	TTCTGGCTGCTCAGACCTTC	59	121 bp
QUAS-Aβ42 R	TAATCGCGCCTTTGTTCGAG	59	

2.3.3. Agarose Gel Electrophoresis

PCR products were run on 1.5% agarose gels, as the DNA fragments varied from 100-1500 bp. The gels were prepared by mixing 1.5% (w/v) of agarose in 1x TAE, microwaving until boil and the agarose fully dissolving in TAE. When the molten gel has cooled down enough to touch, 1:20000 (v/v) of SafeView DNA dye was added, mixed and gels poured into the gel mould. The gels were left to solidify and then placed in the running tank. With 10 µl of each sample loaded into the wells, including a ladder, the gel was then run at 120 V for 15-30 min, depending on the size of the gel, to separate the DNA fragments according to size. The separated fragment gels were then imaged using GeneSys (Version 1.8.60) in an UV transilluminator (G:Box Chemi XX9, Syngene)

2.3.4. Sanger Sequencing

The amplified Phusion® PCR product was purified using PureLink Quick Gel Extraction and PCR Purification Combo Kit and dsDNA concentration was measured using a spectrophotometer fluorometer (DeNovix DS-11 Fx). The product DNA was then diluted to 10-50 ng/µl. 5 µl of diluted DNA was added to 5 µl of used primer (5 µM) in a 1.5 ml Eppendorf tube and sent for Sanger sequencing GeneWiz (Azenta Life Sciences, Germany).

2.4. Histology and imaging

2.4.1. Brain dissection

For initial head dissection two pairs of forceps were used, using one to hold the anesthetised fly in place, and the head removed with the other. Heads were collected in an Eppendorf tube kept on ice until required, then fixed in 200 µl of 4% paraformaldehyde (PFA) in 0.1% Triton-X PBS (PTX). The tubes were then placed on a tube rotator for 15 min. Following fixation, the PFA was removed, and the heads were washed 5 times with 0.1% PTX by rocking 5 mins. Two pairs of forceps and a light microscope were used for brain dissection. The dissection was performed in clear glass spot well plates filled with 0.1% PTX, by removing the outer layer of the head and the retina from the brain and clearing away any visible remaining trachea fragments. Collected brains were kept in 0.1% PTX, in a separate glass well plate on ice. The dissected brains were then fixed for 15 min using 4% PFA in 0.1% PTX and washed with 0.1% PTX 5 times for 5 minutes. The brains were then immediately used for immunostaining.

2.4.2. Amyloid Beta Staining

Fixed dissected brains were first blocked for 1h in blocking solution (10% normal goat serum in 1% PTX). The brains were then stained with 1:400 primary monoclonal mouse anti-amyloid antibody in blocking solution over two nights at 4 °C with gently rocking. Samples were then washed with 0.1% PTX 5 times and then stained with 1:500 secondary anti-mouse goat Alexa Fluor 568 in blocking solution for 1 h. Samples were washed a further 5 times with 0.1% PTX prior to mounting and imaging.

2.4.3. Mounting

Two layers of double-sided tape were used to create a narrow channel (around 2 mm) on a glass coverslip. Stained washed brains were placed in Vectashield to remove residual PTX. The brains were then picked up using a pipette or gently placed on forceps and transferred into the created channel. The channel was then filled with Vectashield and a coverslip gently placed on top ready to be imaged.

2.4.4. Confocal Microscopy

All fluorescence imaging was performed on Zeiss Cell Observer Spinning Disc confocal microscope. Wings were imaged using 10x dry and 63x oil immersion objectives, EGFP channel at 500 ms exposure, 100% 488nm laser power and 2x2 binning. Z-stacks of around 12-25 slices (1 µm thick) were taken of the ROI of each wing. For dual fluorophore experiment, AF647 channel was used to image Td-Tomato signal, at 50% 633nm laser power and 150ms exposure.

Brains were imaged using 10x dry, 20x and 63x oil immersion objectives. Same laser configuration was used as for wing experiments.

2.5. Image analysis

2.5.1. ROI fluorescence analysis

For ROI (region of interest) fluorescence quantification, ROIs were selected and mean, maximum and minimum fluorescence was measured using FIJI (FIJI Is Just ImageJ; Schindelin et al. 2012). Adjusted Mean Fluorescence was calculated by subtracting minimum fluorescence (background noise) from the mean for each image. Adjusted Maximum Fluorescence change was calculated as $\frac{\text{Max. Fluorescence}-\text{Min.Fluorescence}}{\text{Initial Min.Fluorescence}} \times 100\%$ to indicate the change in fluorescence intensity over time, when compared to initial measurement.

2.5.2. Wing LD analysis

For LD visualisation, GFP-tagged LD-binding domain of *klar* was used. Orthogonal (maximum intensity) projections of each Z-stack were created using Zen Blue (Version 2.6). Projections were used for further analysis in ImageJ Fiji.

For lipid droplet analysis, image brightness was adjusted (Image> Adjust> Brightness/Contrast) (Figure 2.3A), ensuring all lipid droplets were visible. Thresholding was applied to each image (Image> Adjust> Threshold), selecting the lipid droplets within the ROI (Figure 2.3B). Images with substantial amount of lipid droplet doublets were turned into Binary (Process> Binary> Make binary) and Watershed function (Process> Binary> Watershed) was applied, separating the doublets (Figure 2.3C). Any remaining doublets were separated manually using the Pencil tool with a reference to the original fluorescence image. Any background beyond the ROI that was subject to thresholding was removed and lipid droplets measured for area and shape descriptors (Figure 2.3D). The selected droplets were then analysed (Analyse > Analyse Particles), using 0.1-Infinity μm^2 size and 0.6-1 circularity filters to eliminate noise. Overlay masks were displayed to visually check all lipid droplets were selected correctly. The length of the vein within the ROI was measured using Segmented line tool for lipid droplet number standardisation.

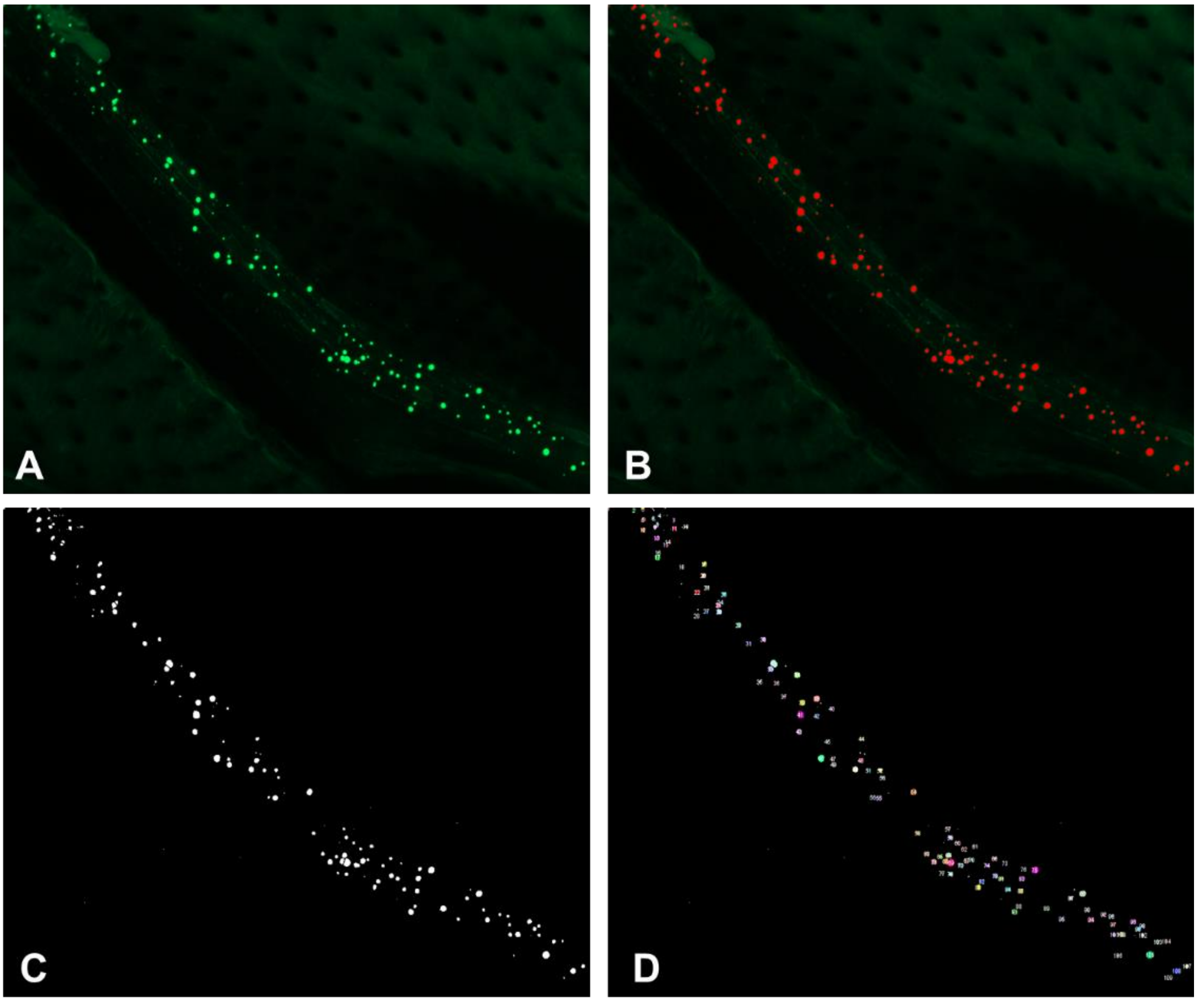

Figure 2.3. Wing LD image analysis pipeline.
A) Adjusted brightness. Lipid Droplet GFP (green) **B)** Thresholding LDs. **C)** Binary and Watershed. **D)** Measuring particles. Screenshots taken from FIJI (FIJI Is Just ImageJ, Schindelin et al. 2012).

2.6. Statistical analysis

Statistical analysis was performed in GraphPad Prism Software (Version 10.1.2). Normality of data was checked by Shapiro-Wilk tests and a P value greater than 0.05 accepted as normal distribution. Significance is represented with following notation: * = p≤0.05, ** = p≤0.01, *** = p≤0.001, **** = p≤0.0001. The following combination of statistical significance tests was used, depending on data analysed: Tukey multiple comparisons test, one-way and two-way ANOVA, Mantel-Cox test. Data is presented as Mean±SD. ANOVA factor effects are reported as “x-way ANOVA; Effect: p-value, F-number” where applicable. **Tables with statistical test results for each figure are available in Appendix II**

2.7. Software

Microsoft Office Excel was used for data storage and formatting, survival data. Graphs were created using GraphPad Prism Software, unless stated otherwise. Benchling was used for DNA sequence visualisation and Clustal Omega was used for sequence alignment.
FIJI (FIJI Is Just ImageJ; Schindelin et al. 2012) was used for LD image quantitative analysis, as well as image adjustment for creation of figures. Zen Blue software was used for taking spinning disk confocal images and creating intensity projections of wing and brain images.

3. Results

3.1. Validating *Drosophila* wing LD-GFP model.

3.1.1. Glial cells are present in *Drosophila melanogaster* wings.

The current lack of rapid LD imaging models in Drosophila called for a creation of a wing-based fly model, utilising the GFP-tagged LD marker. To begin establishing a wing model for studying glial lipid biology, a suitable region of interest (ROI), harbouring plentiful glial cells, had to be selected. Expression of membrane localised GFP peptide (UAS-mCD8::GFP) in glia (repo-Gal4) was used to visualise glia distribution in the fly wing (Figure 3.1A).

Review of glia in wings revealed strong surface expression of the GFP-tagged mCD8 peptide. This was subsequently used to identify suitable ROIs for future experiments.

The proximal aspect of the longitudinal vein 1 (L1) *(*Figure 3.1B) was chosen as a suitable ROI for successive imaging experiments due to its abundance in glia and their proximity to the bundle of neurons, running along the L1. Additional ROI, located on L3 above the anterior crossvein (acv) was initially picked, but was later abandoned, due to lack of consistency in observed LD numbers and a varying phenotype.

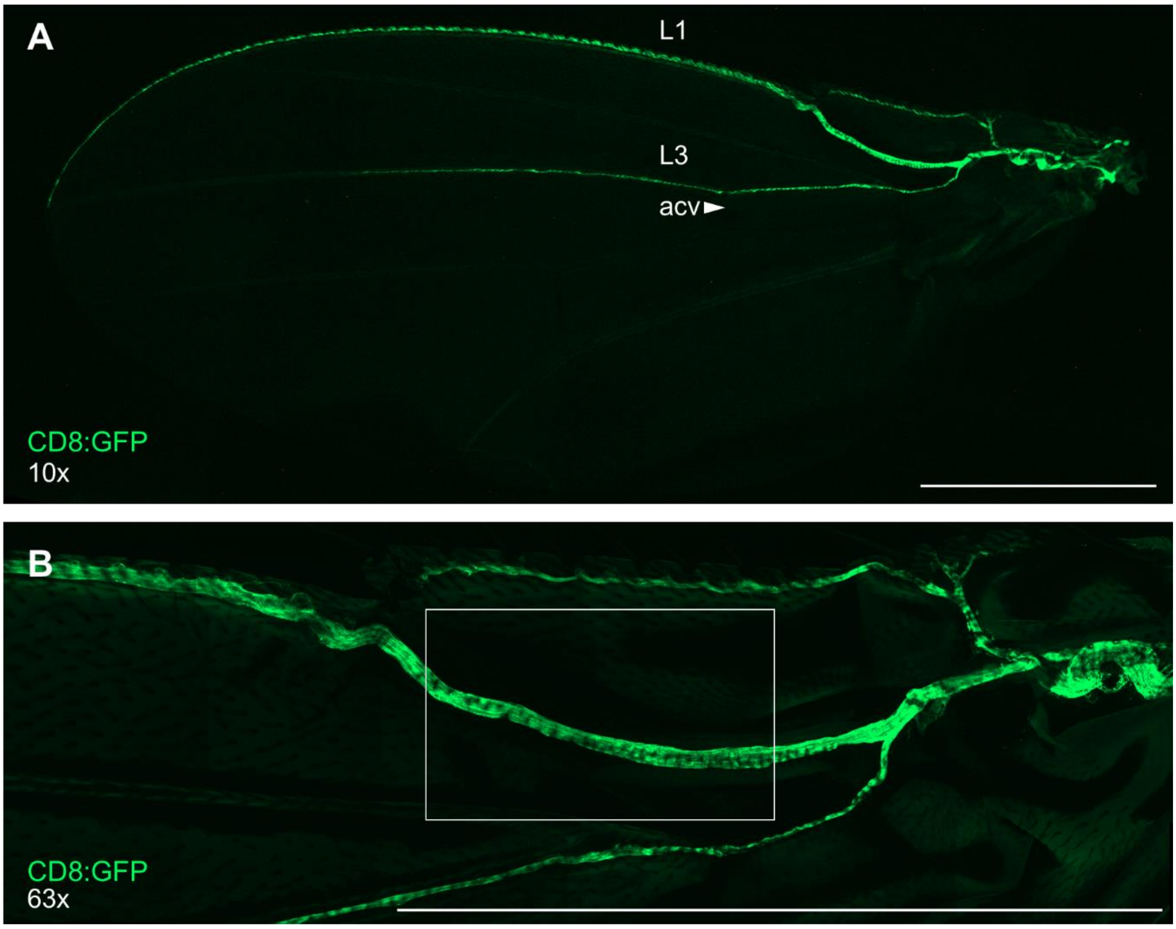

Figure 3.1. Distribution of glial cells in a *Drosophila* wing.
View of a GFP-tagged glial plasma membrane fly wing at **A)** 10x objective and **B)** 63x oil immersion. The white box represents the ROI selected for further LD biology analysis. Scale bars: 500 µm. L1&L3 – longitudinal veins 1&3, acv – anterior crossvein.

3.1.2. Lipid droplet characteristics remain stable after dissection, despite the decline in fluorescence.

Upon establishing the ROI, the expression of GFP-tagged LD-binding domain of klarsicht (klar) (LD-GFP) in glia successfully showed visible lipid droplets in the ROI. As the fluorescent marker is attached to the protein directly, this meant that the wings did not require fixing or staining for imaging and were ready to image straight after dissection. To verify the GFP-tagged protein remains visible and LD characteristics did not differ significantly over time post dissection, the stability of LD morphology was assessed over time with the same ROIs (Figure 3.2). Wings can be imaged without processing following dissection. Therefore, we assessed the stability of the LD-GFP and lipid droplets over time in flies driving UAS-LD-GFP in glia (repo-Gal4>UAS-LD-GFP).

Imaging began 15 mins after wing dissection to allow for mounting and locating and were imaged every 15 mins past that point for 120 mins. As expected, the LD fluorescence decreased over time. Adjusted Mean Fluorescence decreased with each measured timepoint, starting from 138.80±67.19 arbitrary units (a.u.), reaching statistical significance at 45 min post dissection (93.21±38.20 a.u., $p=0.0141$, Tukey multiple comparisons test, RM one-way ANOVA), reaching the lowest point at 120 min post dissection (64.55±22.62 a.u., $p=0.0095$, Tukey multiple comparisons test, RM one-way ANOVA) (Figure 3.2A). Interestingly, ROI mean fluorescence reached a plateau at around 60-100 a.u., which coincided with a decrease of SD at each timepoint, thus reducing the variation between data. Adjusted ROI maximum fluorescence comparison showed a progressive linear decrease in peak ROI fluorescence over time, with 79.24±12.46% ($p=0.0172$, Tukey multiple comparisons test, RM one-way ANOVA) of initial intensity retained at 30 minutes post dissection (Figure 3.2B). The fluorescence intensity ultimately decreased to 37.31±8.61% of the initial measurement, suggesting rapid time-related loss of LD GFP signal in wing glia post dissection. Surprisingly, the LDs were still distinguishable up to 120 minutes post dissection and could be picked up using the image analysis software, albeit the threshold had to be lowered with each subsequent timepoint (Figure 3.2C). The LD number (Figure 3.2D) and total area (Figure 3.2E) remained consistent throughout the timepoints, with only the total area difference reaching statistically significant decrease at 120 mins PI, when compared to the 15 min timepoint (58.13±12.28 μm^2 vs 50.35±13.44 μm^2, $p=0.0007$, Tukey multiple comparisons test, RM one-way ANOVA; Time: $p=0.0004$, $F(5, 35)=6.135$).

These data imply that despite the decrease in fluorescence intensity over time, the LD remain distinguishable for up to 120 minutes post dissection, thus creating a time window for preparation and imaging of several wings at a time. Despite that, it is worth pointing out that throughout all performed experiments the wings were imaged within 30 mins post dissection.

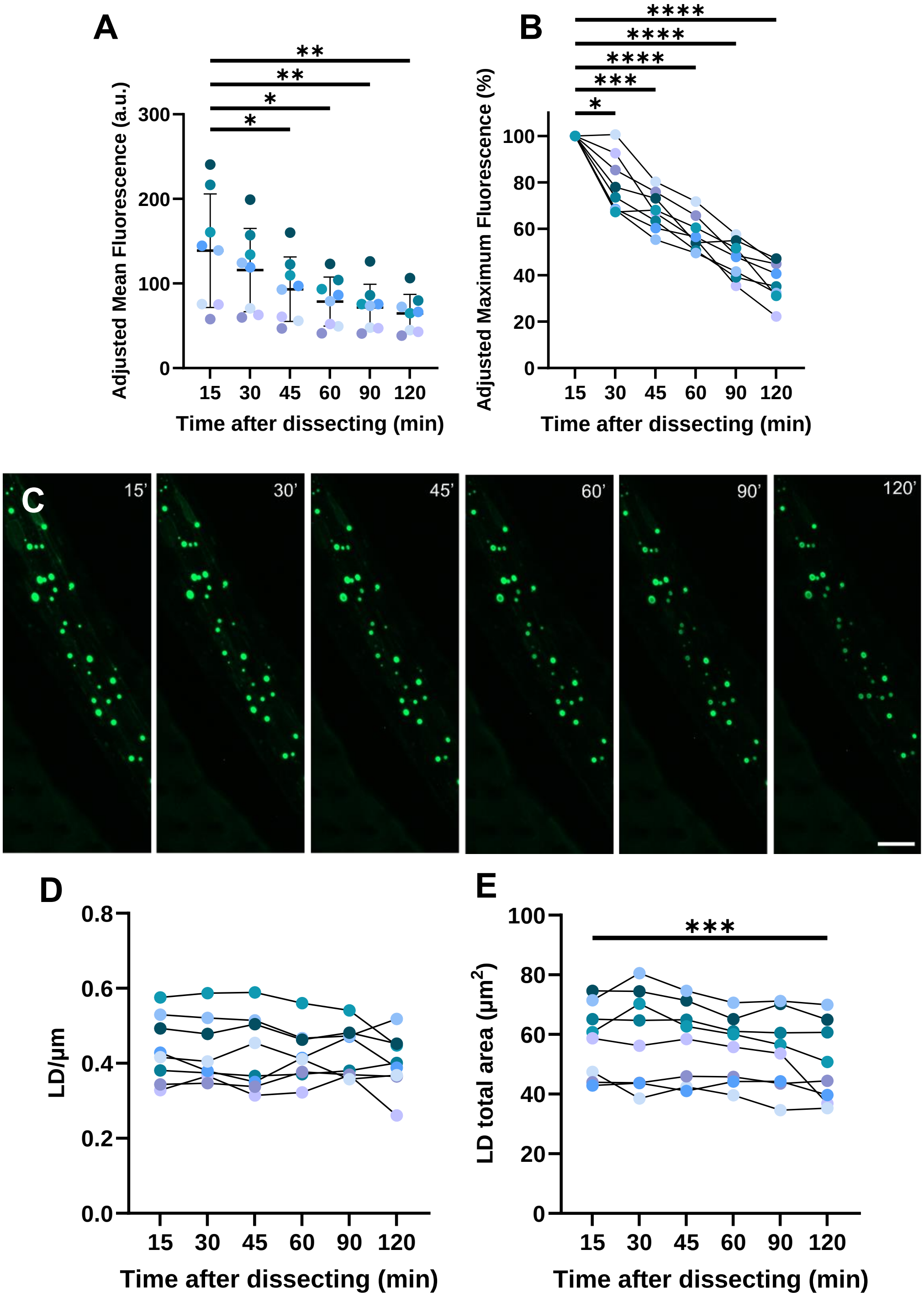

Figure 3.2. Severed wings retain distinguishable LDs over time, despite the decline in fluorescence intensity.
A) ROI mean fluorescence and **B)** ROI maximum fluorescence of an ROI imaged over time. **C)** Representative images of the same ROI taken over the experimental timepoints. 63x lens (oil), GFP. Equal thresholding (50,1500) was applied to each image. **D)** LD count per ROI micron and **E)** ROI total LD area. Genotype: ♀ w^-;UAS-LD-GFP/+;repo-Gal4/+. N=8, Repeated measures one-way ANOVA, * = p≤0.05, ** = p≤0.01, *** = p≤0.001, **** = p≤0.0001. Each data point colour represents an individual ROI. Scale bar = 10µm.

3.1.3. Acute mechanical wing axotomising injury leads to accumulation of lipid droplets in wing glial cells.

The next objective was to establish the dynamic range of the model by identifying the lipid droplet accumulation limits within the wing. Furthermore, we were interested to see whether the homeostasis of glial LDs in fly wings can be altered by mechanical or genetic modification.

Mechanical wing injury was proposed as a severe acute lesion to test the potential range of the model. It was anticipated that damage to the axons, running along the longitudinal veins of the wing, would result in severing them, leading to neuronal cell death. In turn, the glial cells were expected to uptake cellular fragments of the axons and phagocytose them, ultimately producing excess neutral lipids, which would be then stored in glia as lipid droplets.

At 7 DPE wings of flies expressing UAS-LD-GFP and UAS-LacZ in glia (via repo-Gal4 driver) (females, n=10) were cut across the midline, with the cut positioned just after the merge of L1 and the distal wing edge. UAS-LacZ insertion was used as a control for UAS-Aβ42 insertion throughout the project. After 24, 48 and 72h, the LD accumulation of severed wings was measured and analysed. Three time points were used to examine the appropriate timepoint for following experiments, ensuring the capturing of optimal phagocytic activity, and imaging conditions. Absolute number of LDs per ROI had significantly increased from 0.43±0.04 LD/µM at 24h PI to 0.66±0.04 LD/µM at 48h (p=0.0042, Tukey multiple comparisons test, one-way ANOVA) (Figure 3.3A). The number of lipid droplets per ROI then decreased to 0.45±0.04 (48h vs 72h, p=0.0087, Tukey multiple comparisons test, one-way ANOVA) at 72 hours post injury (overall, Time: p=0.0024, F(2, 27)=7.633) . Total LD area within the ROI also peaked at 48h, increasing significantly compared to the other two timepoints (24h vs 48h p=0.0331, 48h vs 72h p=0.0348, Tukey multiple comparisons test, one-way ANOVA; Time: p=0.0177, F (2, 27)=4.703) (Figure 3.3B). There was no statistically significant difference observed in the average LD size between the three timepoints (one-way ANOVA; Time: p=0.796, F(2, 27)=0.2512) (Figure 3.3C).

LDs at 24 and 72 hrs post-injury frequently appeared dimmer and were therefore harder to threshold from background autofluorescence, suggesting prime phagocytic activity happening at around 48h. As such, 48h was chosen as a standard timepoint for the subsequent experiments involving wing injury.

Next, the effect of injury was investigated with respect to uninjured control wings. This time, a cohort expressing LD-GFP and Aβ42 was also included alongside the LD-GFP/LacZ group (Figure 3.4). A dramatic increase in LD numbers in response to mechanical injury was observed across all cohorts (all $p<0.0001$, Tukey multiple comparisons test, two-way ANOVA; Injury: $p<0.0001$, $F(1, 38)=193.9$) (Figure 3.4A). A similar increase in LD total area within the ROI was also observed in all cohorts (all $p<0.0001$, Tukey multiple comparisons test, two-way ANOVA; Injury: $p<0.0001$, $F(1, 38)=374.0$) (Figure 3.4B). Furthermore, the average LD size has shown to follow a trend of larger LDs displayed by injured wings, statistically significant in both cohorts ($p<0.0001$ in Aβ42 flies and $p=0.0009$ in LacZ flies, Tukey multiple comparisons test two-way ANOVA) (Figure 3.4C). Uninjured fly wings did not show any significant difference when compared to healthy wings from naïve flies (data not shown), suggesting there is no apparent systemic effect on the healthy wings following the injury of the other one.

Generally, Aβ42 flies possessed somewhat more LDs that were larger. However, this was not observed as a significant trend. It appears to potentially be a result of an additive effect of uninjured amyloid wings normally having slightly higher LD production, possibly due to amyloid toxicity, compared to LacZ (Figure 3.5), rather than being directly modulated by it.

These findings provided an estimation of the upper limit of lipid droplets in the wing glia at a time, appearing to peak at just over 1.25 LD/μm and a 120 μm^2 of fluorescent LDs per typical ROI. Furthermore, these findings show that flies expressing both the control LacZ and the Aβ42 peptide show similar responses to mechanical injury.

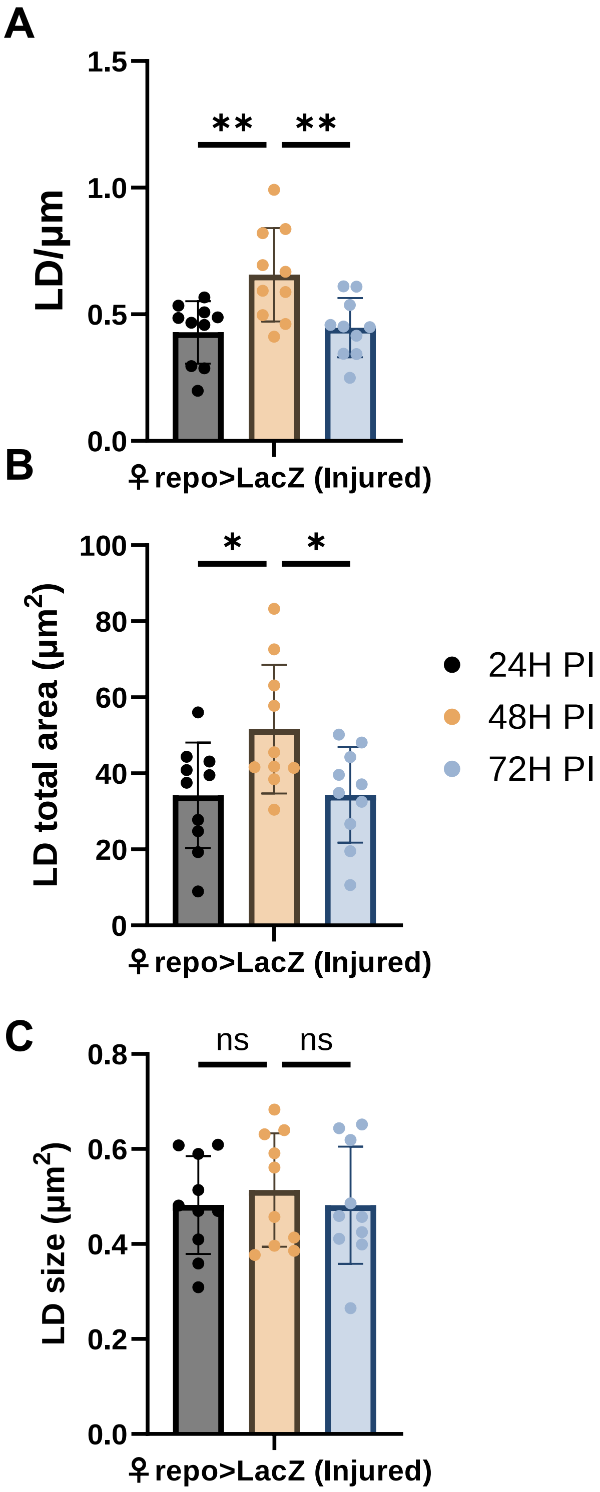

Figure 3.3. LD peak at 48H after induction of mechanical injury.
Comparison of the **A)** quantity of LDs per ROI vein micron (LD/µm), **B)** total area and **C)** average size between different timepoints post injury (PI). Genotype: ♀ w^-;UAS-LD-GFP/UAS-LacZ;repo-Gal4/+. Females, n=10. Ordinary one-way ANOVA, ns = p>0.05, * = p≤0.05, ** = p≤0.01.

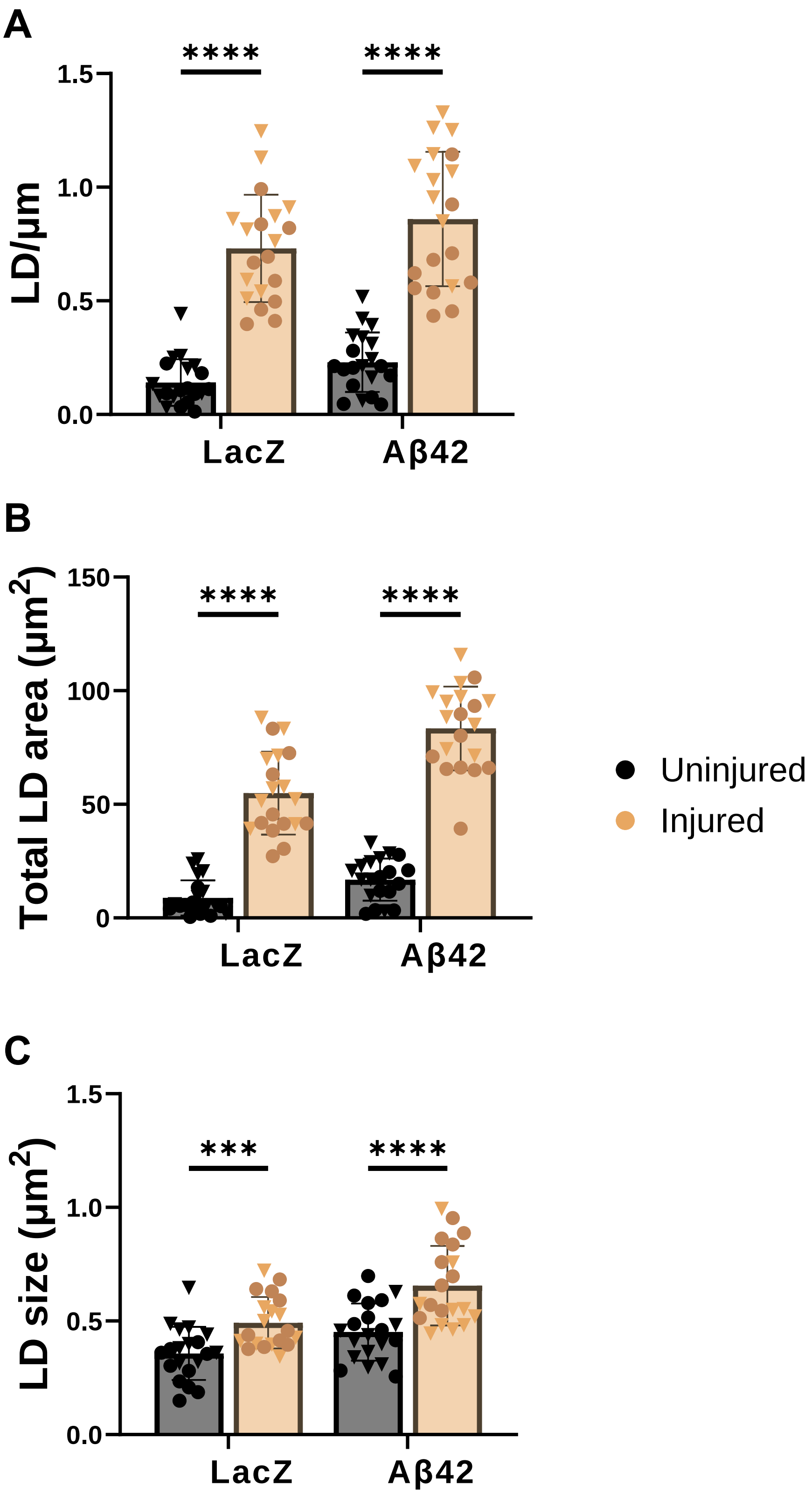

Figure 3.4. Mechanical injury of *Drosophila* wing leads to an increase in LDs.
Comparison of ROI lipid droplet **A)** number, **B)** total area, and **C)** average size, between an injured and uninjured wing of the same flies 48h post injury (PI). Genotype: ♀♂ w^-;UAS-LD-GFP/X;repo-Gal4/+, where X is either UAS-LacZ or UAS-Aβ42. N= 20 per condition (10 females and males each), darker circles represent female data points and lighter inverted triangles represent male data. Two-way repeated measures ANOVA, *** = p≤0.001, **** = p≤0.0001.

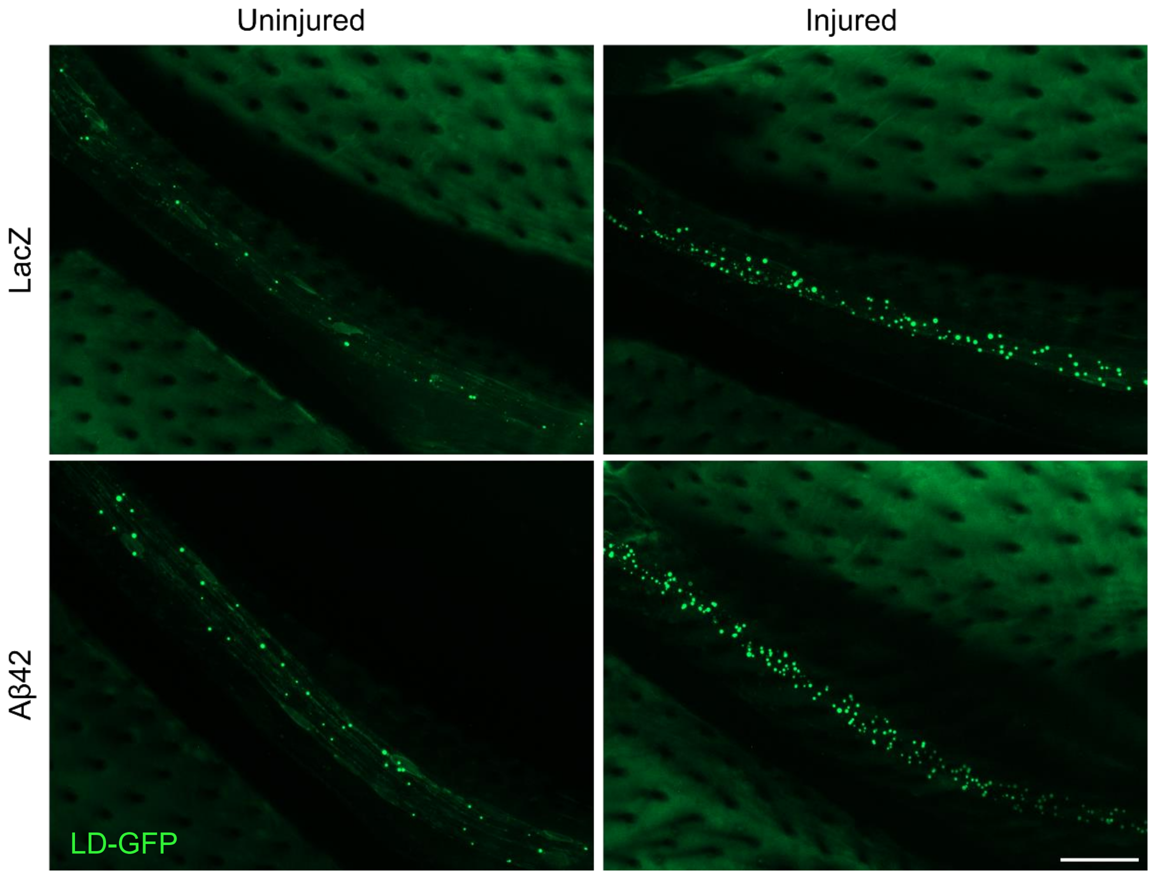

Figure 3.5. Injury effect on glial LD in *Drosophila* wings
Representative images of glial wing LDs (in green) in male experimental cohorts at 7DPE. 63x oil immersion lens. Genotype: ♀♂ w^-;UAS-LD-GFP/X;repo-Gal4/+, where X is either UAS-LacZ or UAS-Aβ42 Scale bar: 20 µm.

3.1.4. Acute mechanical injury phenotype can be modulated by *draper* expression in glial wing model

To further validate the robustness of our lipid droplet model, we next sought to modulate our phenotype by altering the expression of *draper. Draper*, orthologous to human Megf10, is a receptor expressed highly in glia, implemented in the clearance of damaged axons and apoptotic cells, and essential for engulfment of axonal debris (MacDonald et al. 2006; Ray et al. 2017). We hypothesised that changes in *draper* expression will alter lipid droplet homeostasis observed in response to axonal severance. For control, UAS-attp40-PJFRC line was used, containing an empty vector with UAS binding site and no encoded cDNA, thus not expressing any transgenes.

In flies overexpressing *draper*, lipid droplets were significantly increased compared to attp40-PJFRC controls (0.57±0.21 LD/μm to 0.88±0.42 LD/μm, $p<0.0001$, Tukey multiple comparisons test, Two-way ANOVA; overall Genotype: $p<0.0001$, $F(2, 172)=14.07$) (Figure3.6A). Similar change was observed in the total LD area, increasing from 46.11±14.77 μm^2 to 93.29±35.65 μm^2 ($p<0.0001$, Tukey multiple comparisons test, two-way ANOVA; overall Genotype: $p<0.0001$, $F(2, 172)=57.60$) (Figure 3.6B). The average LD size has significantly increased in both injured and uninjured flies overexpressing *draper* in a similar manner, when compared to the control line ($p<0.0001$ for both, Tukey multiple comparisons test, two-way ANOVA; overall Genotype: $p<0.0001$, $F(2, 172)=51.70$) (Figure 3.6C). Unlike the average size, there was no significant difference observed in LDs per micron between uninjured wings of the two cohorts ($p= 0.9835$, Tukey multiple comparisons test, two-way ANOVA). However, the total area of LD has shown a small significant increase from 12.87±10.68 μm^2 in uninjured control wings to 29.78±15.26 μm^2 in wings overexpressing *draper* ($p=0.01$, Tukey multiple comparisons test, two-way ANOVA), suggesting some potential increase in LD production under normal conditions in *draper* OE flies.

On the other hand, *draper* RNAi knockdown displayed no effect on LD homeostasis. For both uninjured and injured cohorts, LD number per micron ($p>0.999$ and $p=0.8844$, respectively; Tukey multiple comparisons test, two-way ANOVA), total area ($p=0.9602$ and $p=0.8013$, Tukey multiple comparisons test, two-way ANOVA), and average size ($p=0.0506$ and $p=0.9807$, Tukey multiple comparisons test, two-way ANOVA) did not display any significant differences when compared to control attp40-PJFRC flies. This data shows that modulating expression of *draper* can impact lipid droplet homeostasis, but also suggests that *draper* is not required for axotomy-induced LD accumulation. Nonetheless, this clearly demonstrates that wing LDs respond to introduction of transgenes and modulate their homeostasis accordingly.

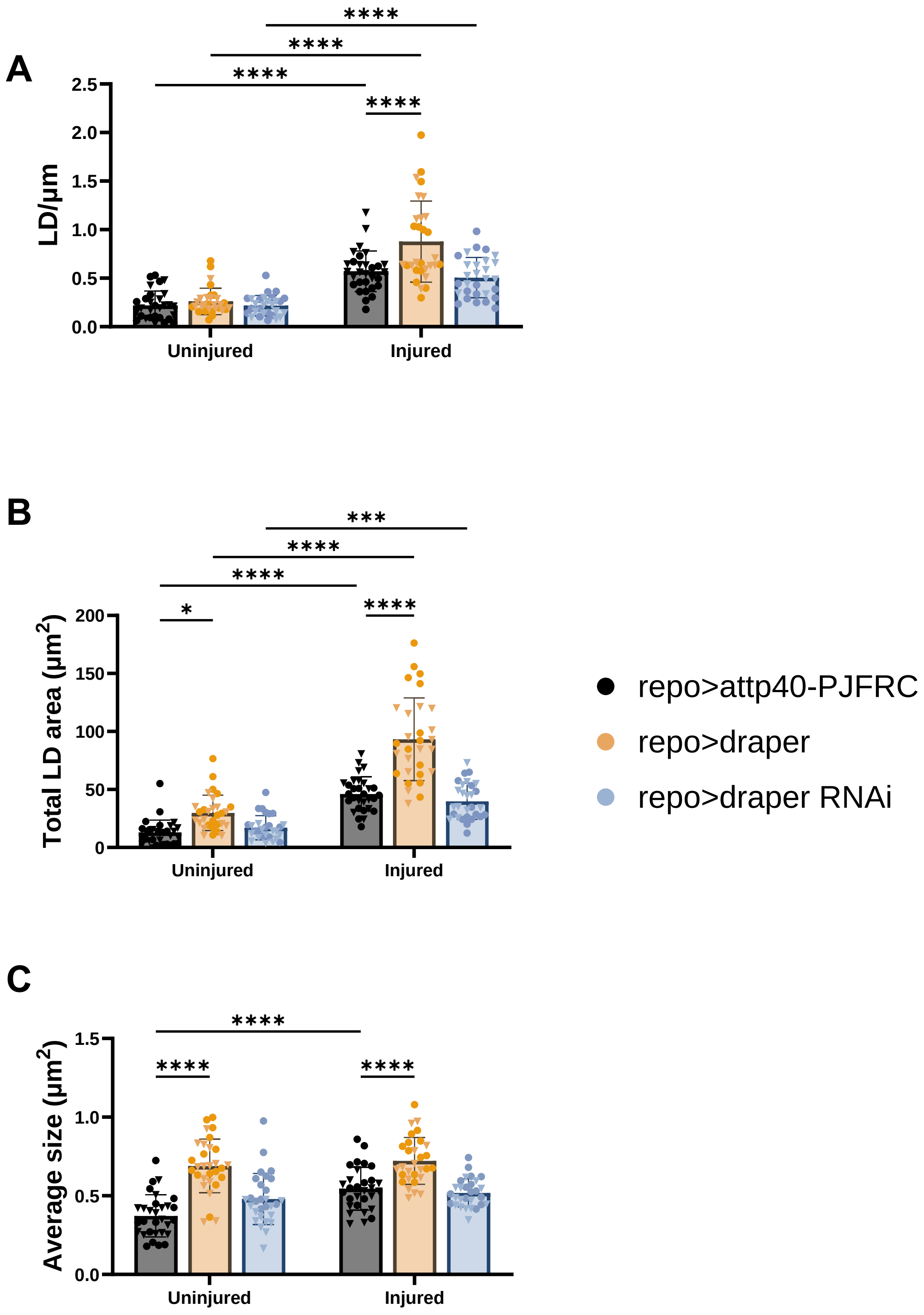

Figure 3.6. *Draper* overexpression modulates LD production in response to axon injury. Comparison of the LD **A)** number per micron, **B)** total area and **C)** average size between control (attp40-PJFRC), *draper* overexpression (OE), and *draper* RNAi knockdown lines. Genotype: ♀♂ w^{-};UAS-LD-GFP/X;repo-Gal4/+, where X is either UAS-draper or UAS-draperRNAi, or UAS-attpJFRC40 N=30 (15 males and 15 females combined), darker circles represent female data points and lighter inverted triangles represent male data, two-way ANOVA, ns = p>0.05, * = p≤0.05, *** = p≤0.001, **** = p≤ 0.0001.

3.2. Effects of glial Aβ42 toxicity on LD homeostasis in glia.

3.2.1. Control transgene expression does not appear to affect LD homeostasis.

To ensure that the increase in LD production is a direct effect of Aβ42 toxicity not LacZ expression, we sought to use another control. Similarly to UAS-attp40-PJFRC, UAS-atttP2-PJFRC would sequester available Gal4, and titrate it appropriately, similarly to LacZ, but without expressing any transgenes. We also assessed how sole expression of LD-GFP within the Gal4/UAS system impacts LD characteristics, as all of the Gal4 within the system would be available for binding the UAS transcription enhancer of the fluorescence marker. To control for that, we utilised the Q-system alongside Gal4/UAS (dual binary), allowing us to express the fluorescent LD marker in glia via Gal4/UAS and introduce LacZ expression in neurons via Q-system. Neuron-specific nSyb-QF2 driver was used as there were no Q-system glial promoters in the lab stock for this experiment.

Substitution of LacZ control with attp2-PJFRC in glia has shown no significant difference in LDs per micron (0.10±0.06 LD/μm vs 0.07±0.05 LD/μm, p=0.5730, Tukey multiple comparisons test, one-way ANOVA) (Figure 3.7A), as well as total lipid droplet area (4.88±4.50 μm^2 vs 4.54±5.82 μm^2, p=0.9984, Tukey multiple comparisons test, one-way ANOVA) (Figure 3.7B), with a slight increase seen in LD average size (0.28±0.12 μm^2 vs 0.38±0.17 μm^2, p= 0.0211, Tukey multiple comparisons test, one-way ANOVA) (Figure 3.7C).

Interestingly, LD fluorescent marker expressed on its own, and thus sequestering all of the available Gal4, has shown a dramatic increase in LD number (0.10±0.06 LD/μm vs 0.23±0.09 LD/μm, p<0.0001, one-way ANOVA) and total area (4.88±4.50 μm^2 vs 18.26±10.37 μm^2, p<0.0001, Tukey multiple comparisons test, one-way ANOVA) when compared to LD-GFP expressed alongside LacZ. Average size of lipid droplet did not show any significant differences between the two cohorts (p= 0.4850, Tukey multiple comparisons test, one-way ANOVA). The dual binary line showed a similar effect when compared to sole LD-GFP expression, however the average size of its lipid droplet was in fact significantly differing from LacZ-LD fly line (0.28±0.12 μm^2 vs 0.45±0.10 μm^2 , p<0.0001, Tukey multiple comparisons test, one-way ANOVA). Both sole LacZ and dual binary lines had no significant differences between their number of LDs per micron (0.23±0.09 LD/μm vs 0.27±0.13 LD/μm, p= 0.4377, Tukey multiple comparisons test, one-way ANOVA), and total LD area (18.26±10.37 μm^2 vs 18.89±9.80, p= 0.9914, Tukey multiple comparisons test, one-way ANOVA).

This data suggests that LacZ most likely does not play a significant role in LD homeostasis and can be used as a control when assessing the effects of Aβ42 on LD biology. Furthermore, the data show that Gal4 concentration and availability directly impacts the visible GFP-tagged LDs.

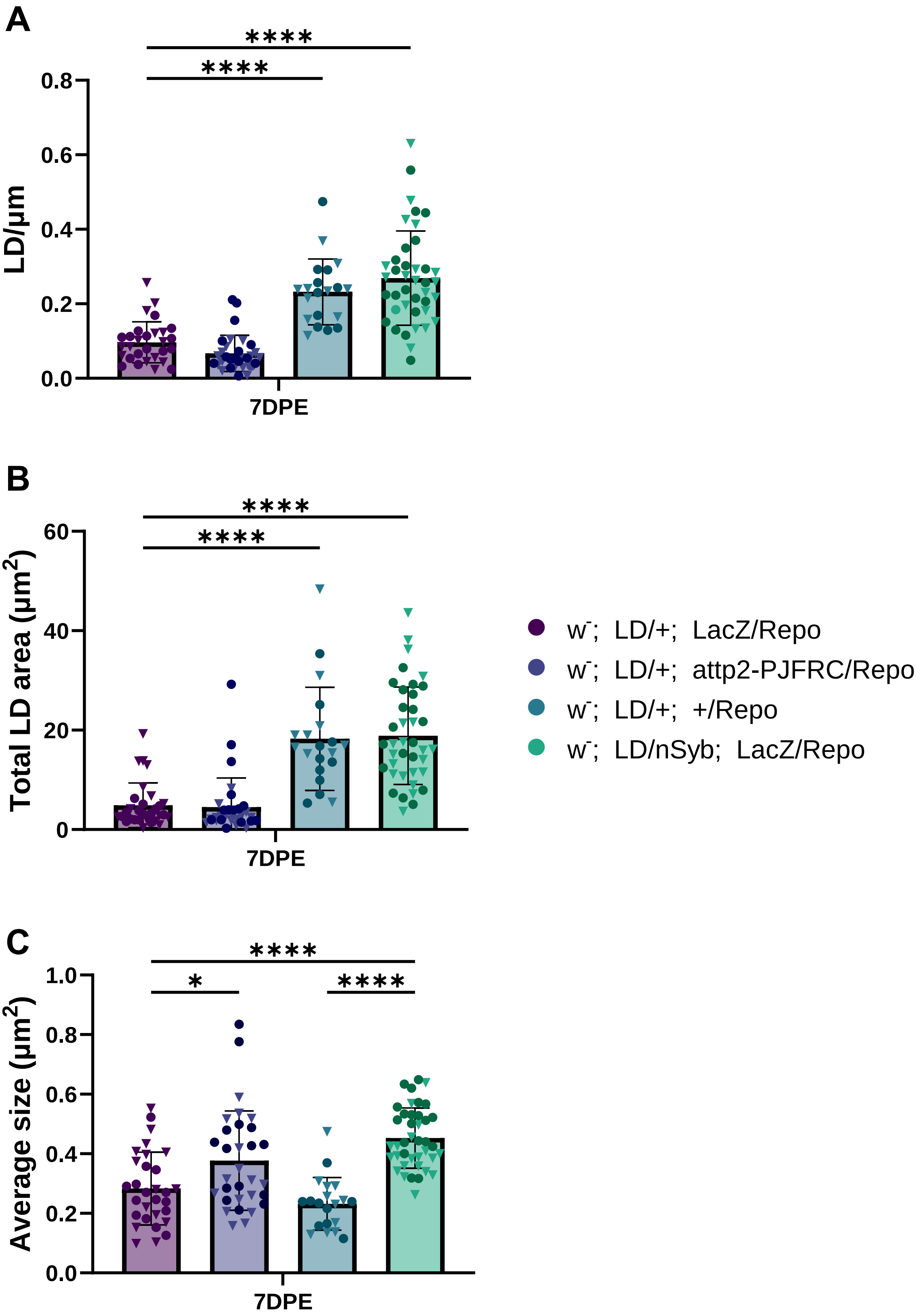

Figure 3.7. Glial LacZ expression does not affect LD characteristics in wing glia.
Comparison of LD characteristics (**A)** number per micron, **B)** total LD area, **C)** average LD size) between controls where LD-GFP is co-expressed with another transgene in the same expression system (LacZ or attp2-PJFRC) and not (LacZ and +, or LacZ in a dual binary system). N=30, 30, 20, 40 respectively (50:50 male:female ratio). Darker circles represent female data points and lighter inverted triangles represent male data. Two-way ANOVA, * = $p<0.05$, **** = $p \leq 0.0001$

3.2.2. Glial Aβ42 expression drives LD production in wing glia.

The next goal was to investigate the direct effects of glial Aβ42 peptide expression on LD homeostasis in *Drosophila* wing glia. Similarly to the previous experiment, two fly lines were used: flies with RepoGal4 driving expression of LD-GFP together with either LacZ or Aβ42. The imaged wings did not undergo mechanical injury this time, thus the differences in LD characteristics between the cohorts could be speculated to be a direct result of Aβ42 expression or lack thereof.

Aβ42 expression significantly increased the count of LDs per micron in wing glia, when compared to flies expressing LacZ in flies aged 7, 14 and 21 DPE ($p<0.0001$ for each timepoint, Tukey multiple comparisons test, two-way ANOVA; Time: $p<0.0001$, $F(5, 348)=10.42$, Genotype: $p<0.0001$, $F(1, 348)=152.4$, Interaction: $p<0.0001$, $F(5, 348)=6.671$) (Figure 3.8A). 21 DPE appeared to be the timepoint where LD quantity in both LacZ and Aβ42 flies reached its peak (0.12±0.08 LD/μm and 0.32±0.10 LD/μm respectively).

Total area of LDs followed a similar trend, however significant increase was observed at 14, 21 and 28 DPE timepoints ($p<0.0001$ for each timepoint, Tukey multiple comparisons test, two-way ANOVA; Time: $p<0.0001$, $F(5, 348)=12.34$, Genotype: $p<0.0001$, $F(1, 348)=140.7$, Interaction: $p<0.0001$, $F(5, 348)=5.324$), with a peak at 21DPE (11.94±9.36 μm^2 for LacZ vs 38.72±15.66 μm^2 for Aβ42) (Figure 3.8B). A slight increase in total LD area was also observed in Aβ42 flies at 50DPE (7.93±9.51 μm^2 vs 18.69±17.16 μm^2, $p=0.03$, Tukey multiple comparisons test, two-way ANOVA). Interestingly, LDs in LacZ flies did not follow this trend, where no significant time-dependent difference in LD total area was seen.

A similar trend was also observed in the LD average size, however average size plateaued at 21 DPE (0.48±0.21 μm^2 for LacZ and 0.74±0.20 μm^2 for Aβ42), and decreased less drastically, when compared to the other metrics (Figure 3.8C). The average size was significantly different between two cohorts at 14 DPE, 21DPE, 28DPE, and 35 DPE ($p=0.0013$, $p<0.0001$, $p<0.0001$, and $p=0.0027$ respectively, Tukey multiple comparisons test, two-way ANOVA; Time: $p<0.0001$, $F(5, 348)=22.46$, Genotype: $p<0.0001$, $F(1, 348)=95.84$, Interaction: $p=0.001$, $F(5, 348)=4.227$).

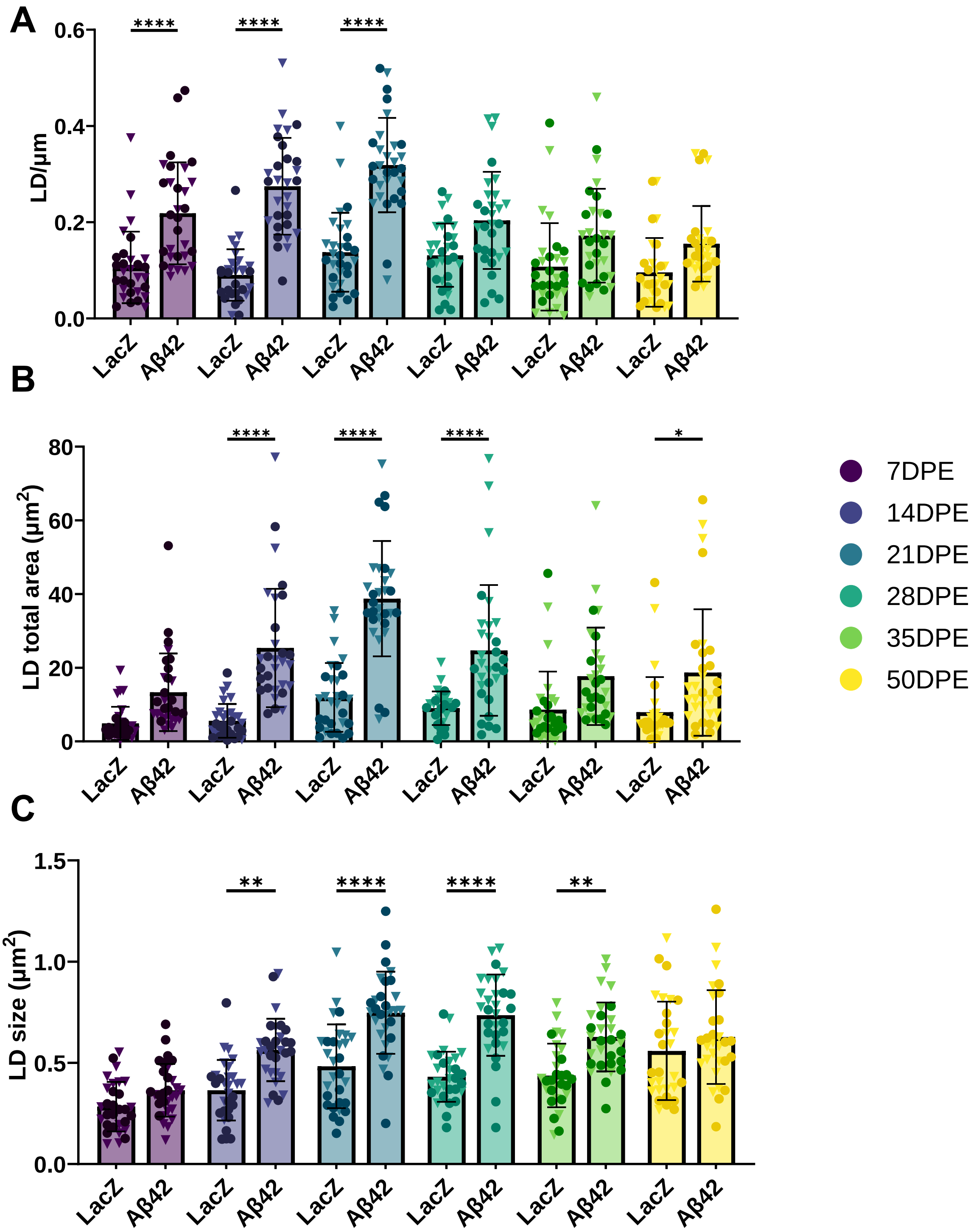

Figure 3.8. Aβ42 expression in glia drives LD production in *Drosophila* wing glia.
Comparison of LD (**A)** number per micron, **B)** total LD area, **C)** average LD size) between flies driving LacZ (control) or Aβ42 peptide, alongside LD-GFP. Genotype: ♀♂ w⁻;UAS-LD-GFP/X;repo-Gal4/+, where X is either UAS-LacZ or UAS-Aβ42 N=30 (15 females and 15 males combined). Darker circles represent female data points and lighter inverted triangles represent male data. Two-way ANOVA, * = p<0.05 ** = p≤0.01, **** = p≤0.0001.

This data clearly demonstrates that Aβ42 expression in glia affects glia LD homeostasis by increasing the number of LDs earlier in the fly lifespan, with a significantly higher peak.

Furthermore, the clear change of LD homeostasis in flies expressing Aβ42 peptide further suggest that the LD-GFP-based wing model can display phenotypic changes in response to genetic alterations, such as transgene expression. These findings led us to the development of a dual binary model, where we sought to investigate the role of neuronal amyloid toxicity on glial LD phenotype, in line with our current understanding of its involvement in AD.

3.3. Cell autonomous role for glia LD accumulation in response to neuronal amyloid

3.3.1. Dual binary model allows for unique transgene expression between wing neurons and glia.

The introduction of independent control of gene expression between neurons in glia was then implemented by utilising two expression systems, creating the dual binary model. The first objective of developing the dual binary model was to assess whether the used cell type-specific promoters are capable of differential temporospatial expression within the fly wing. We achieved that by expressing two fluorophore-tagged mCD8 proteins: UAS-mCD8::GFP in glia (via Repo-Gal4) and QUAS-mCD8::tdTomato in neurons (via nSyb-QF2).

This expression of two fluorescent markers has allowed for differential visualisation of both neuronal (in red) and glial (in green) populations (Figure 3.9). The two distinct cell types were best visible at the tip of the wing, where L1 and L3 meet (Figure 3.9A, Figure 3.9A’ green channel only, Figure 3.9A” red channel only). Sensory neuron projections into the wing bristles, as well as glial cells wrapping the axons and some of the somas were visible, a characteristic phenotype of both cell types. The two cell types were in very close proximity within the ROI typically used for LD imaging (Figure 3.9B), however it was noticed that glial cells were enwrapping the neuron bundle, characteristic of wrapping glia cells in *Drosophila*, which wrap neurons and act as insulating and ensheathing cells, similar to myelination. Furthermore, this proximity reaffirms the use of fly wings as a model of studying the interaction between these two cell types.

Additionally, we have replaced the glial mCD8::GFP with LD-GFP and performed axon severance via wing injury on flies to visualise the distribution of observed LDs and whether there were any LDs visible beyond glia (Figure 3.9C). Upon the injury, distinct glial LDs could be seen, along with visibly a disordered axon bundle, suggesting the axon severance indeed impacts the neuronal projections within the fly wing vein.

These findings showcased the ability of the dual binary construct to express distinct transgenes within different cell types and that no obvious bleed-through or non-specificity was observed, with the following step being the validation of neurodegenerative phenotype of QUAS-Aβ42 insertion.

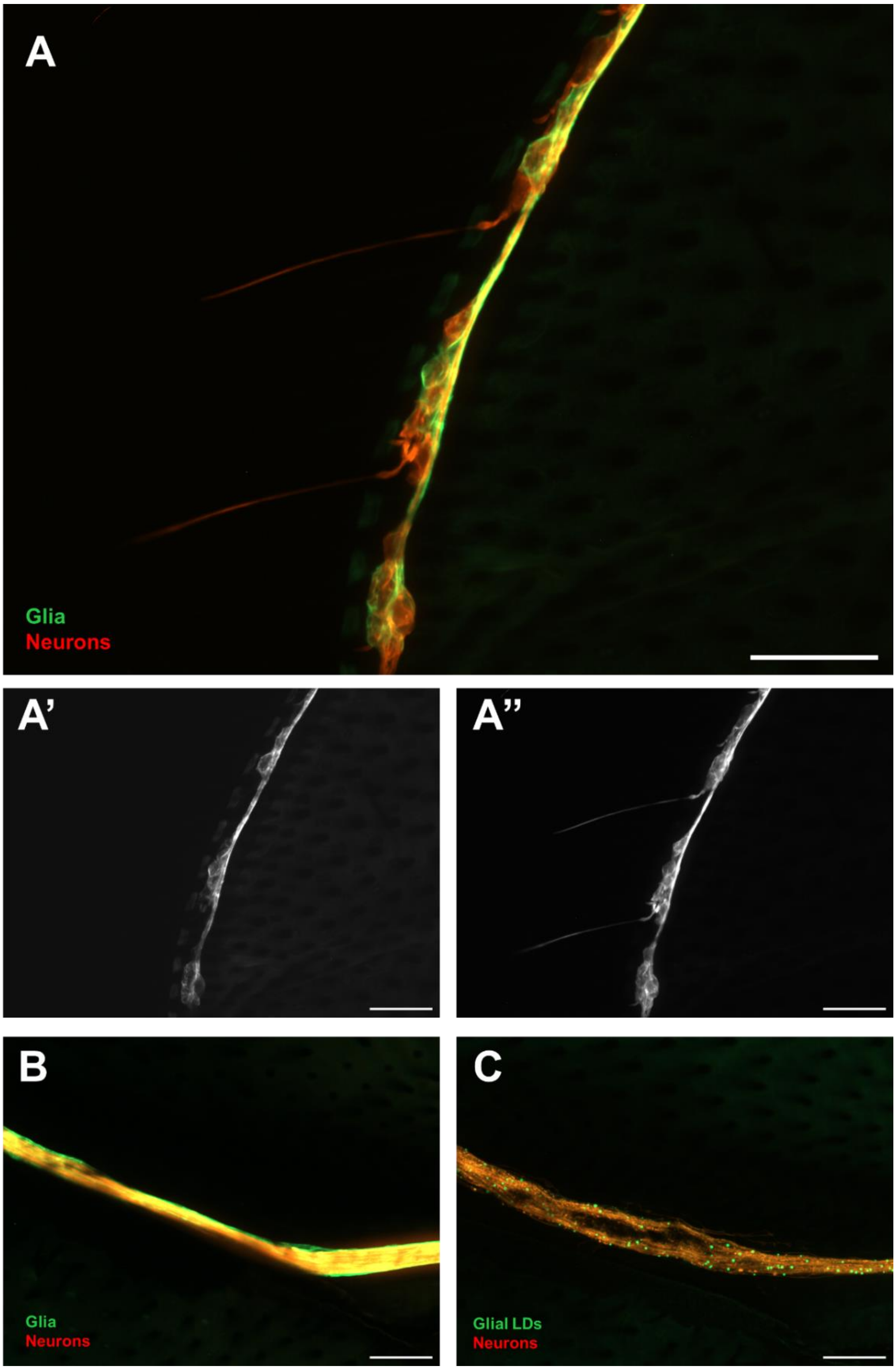

Figure 3.9. Dual binary system allows for unique transgene expression between neurons and glia.
Glial cells in green (UAS-mCD8::GFP) and neurons in red (QUAS-mCD8::tdTomato) in **A)** the L1 and L3 vein junction (with **A’)** green and **A”)** red channels visualised separately in greyscale), **B)** L1 ROI, and **C)** in injured L1 ROI female fly wing at 7DPE. 63x oil immersion lens. Genotype: ♀ w⁻; UAS-LD-GFP/QUAS-mCD8::tdTomato; nSyb-QF2/repo-Gal4. Scale bars: 20 μm.

3.3.2. QUAS-Aβ42 line contains modified DNA encoding for Aβ42 peptide.

Laboratory stock of QUAS-Aβ42, previously ordered from BDSC, was confirmed for Aβ42 insertion by running a PCR of its extracted gDNA. As flies do not contain the genetic code for Aβ42 peptide, an insertion of Aβ42 within any construct was expected to be detected by PCR. Surprisingly, no Aβ42 amplification product was observed in QUAS-Aβ42 samples when using human Aβ42 primers (Figure 3.10A). Additional PCR using primers for Hsp70 and Sv40 (plasmid regions, flanking the insertion site) was run, to ensure that the fly line retained any transgene insertion at all, which indeed was the case (Figure 3.10B). Interestingly, the product band appeared slightly shorter (around 600bp), compared to the UAS-aos::Aβ42^{arc} line, used as a default Aβ42 peptide stock in the laboratory.

After confirming that the QUAS insertion was not accidentally lost by the laboratory stocks over time, we amplified the insertion site DNA and sent for Sanger sequencing.

The sequencing proved that the insertion contained a sequence for the Aβ42 peptide, which was modified and adapted for insect codon usage bias (Figure 3.11A, sequence in Appendix III), in line with the existing literature using this fly line (Crowther et al. 2006; Li et al. 2018). The codon usage bias refers to different preference of synonymous codons in insects, which differs from humans (Behura and Severson 2013). Upon alignment with the Aβ42^{arc} insertion used in the lab, it became evident that the DNA code differed significantly to not be amplified by the Aβ42 primers in use (Figure 3.11B).

The bias change of codons was synonymous, meaning the translated peptide would have the same amino acid residues as wildtype Aβ42. It is worth noting, that the UAS-aos::Aβ42^{arc} line, used in previous glial experiments, harbours the Arctic mutation (E22G), thus actually differing from the QUAS-expressed wildtype peptide by one amino acid residue. Due to a lack of alternative QUAS-Aβ42 insertion available at the time, it was decided to proceed with the wildtype QUAS-Aβ42 insertion.

Upon clarification of the QUAS-Aβ42 insertion sequence, three primer pairs were designed for genotype validation by PCR; only one of which was specific to the insertion and used to confirm the presence of insertion in experimental flies (Table 2.4).

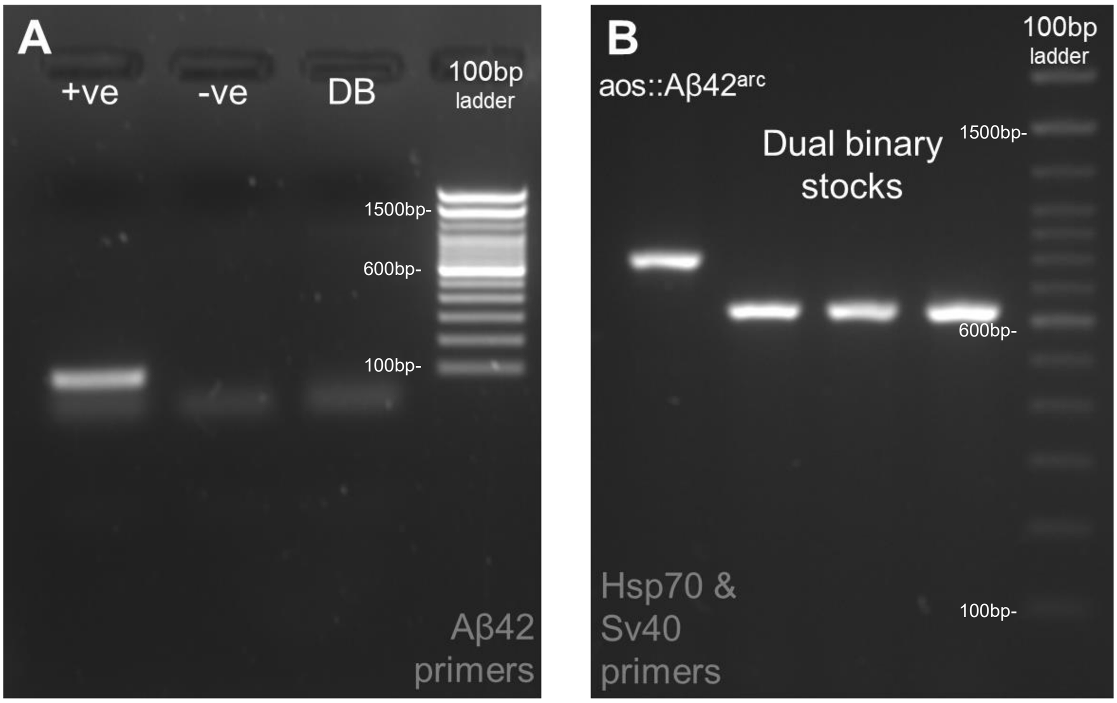

Figure 3.10. QUAS-Aβ42 line do not contain a human-specific Aβ42 sequence but contain a pQUAS/UAS insertion.
A) Gel electrophoresis of Aβ42 genotyping PCR products. Insertion-positive samples were expected to contain a 121 bp band. 1.5% agarose in TAE, 15 min at 110V. B) Gel electrophoresis of Hsp70 and Sv40 genotyping PCR products. The product length depended on the insertion between these two sites. 1.5% agarose in TAE, 30 min at 120V.

A

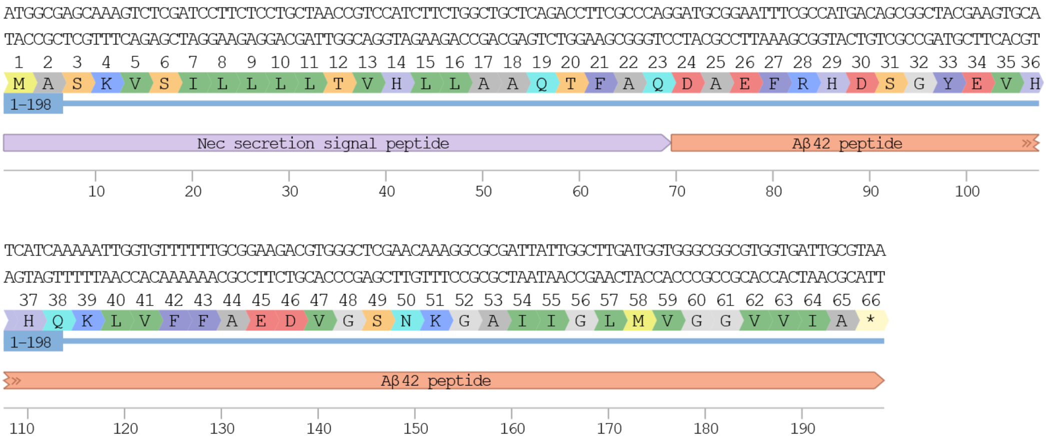

B

```
hAPP            GATGCCCGCCCTGCTGCCGACCGAGGACTGACCACTCGACCAGGTTCTGGGTTGACAAAT  1980
QUAS-Abeta42    -------------ATGGCGAGCAAAGT-------CTCGATCCTTC----TCCTGCTAACC  36
                              ** *** * * *        ***** *           **  **

hAPP            ATCAAGACGGAGGAGATCTCTGAAGTGAAGATGGATGCAGAATTCCGACATGACTCAGGA  2040
QUAS-Abeta42    GTCCATCTTCTGGCTGCTCAGACCTTCGCCCAGGATGCGGAATTTCGCCATGACAGCGGC  96
                 ** *      **            *      ****** ***** ** ******   **

hAPP            TATGAAGTTCATCATCAAAAATTGGTGTTCTTTGCAGAAGATGTGGGTTCAAACAAAGGT  2100
QUAS-Abeta42    TACGAAGTGCATCATCAAAAATTGGTGTTTTTTGCGGAAGACGTGGGCTCGAACAAAGGC  156
                ** ***** ******************** ***** ***** ***** ** ********

hAPP            GCAATCATTGGACTCATGGTGGGCGGTGTTGTCATAGCGACAGTGATCGTCATCACCTTG  2160
QUAS-Abeta42    GCGATTATTGGCTTGATGGTGGGCGGCGTGGTGATTGCGTAA------------------  198
                ** ** *****  * *********** ** ** ** ***  *
```

Figure 3.11. QUAS-Aβ42 flies express wildtype Aβ42 peptide but contain altered DNA sequence.
A) DNA and AA translation sequences of necrotic protein (nec) secretion peptide and Aβ42 insertion fragment on pQUAS of QUAS-Aβ42 flies. Visualised using Benchling **B)** Human APP cDNA and QUAS-Aβ42 amyloid peptide sequence alignment. Asterisks indicate conserved nucleotide residues. Sequences aligned and visualised using Clustal Omega.

3.3.3. Validation of QUAS-Aβ42 toxicity within dual binary model.

Before proceeding with the wing imaging experiments, we first sought to explore whether the QUAS-Aβ42 insertion had any effect on *Drosophila* survival when expressed in neurons via Q-system along with LD-GFP expression via Gal4-UAS. This would allow the validation of the efficiency of the Aβ42 insertion and strength of the neurodegenerative phenotype it causes, as well as allow the establishment of imaging timepoints based on average lifespan of experimental cohorts.

A drastic decrease in lifespan was observed in flies harbouring QUAS-Aβ42 insertion when compared to LacZ controls (Figure 3.12A). The median survival of LacZ flies (43 days for males and 44.5 for females) was effectively halved in Aβ42 flies (19 days for males and 20 days for females), showing highly significant difference when comparing the cohorts ($p<0.0001$ for both sexes, Kaplan-Meier simple survival analysis, Log rank (Mantel-Cox) test, $\chi^2=290.3$). Males and females were split into separate cohorts to ensure the was no sex-dependent phenotype variation, which appeared to be not the case.

These data indicated that the neurodegeneration driven by QUAS-Aβ42 insertion is extremely strong, proving the insertion as a suitable model of inducing AD-like neurodegenerative phenotype. This also meant that the timepoints for wing imaging had to be adjusted, considering over half of Aβ42 flies are dead past around 20 DPE, which is considerably sooner when compared to previous experimental cohorts.

With the evident effect of QUAS-Aβ42 insertion on fly longevity observed, we then sought to verify whether these flies accumulate amyloid peptides in the brain, a critical hallmark of AD.

Brains of dual binary flies expressing either QUAS-LacZ or QUAS-Aβ42, alongside UAS-LD-GFP were dissected and stained for Aβ42 peptides (Figure 3.12B-C). The images showcased a clear difference between LacZ flies (Figure 3.12B) and QUAS-Aβ42 flies (Figure 3.12C), with the latter showing a pattern of amyloid aggregation similar to UAS-aos::Aβ42^{arc} line, previously observed in the laboratory (data not shown).

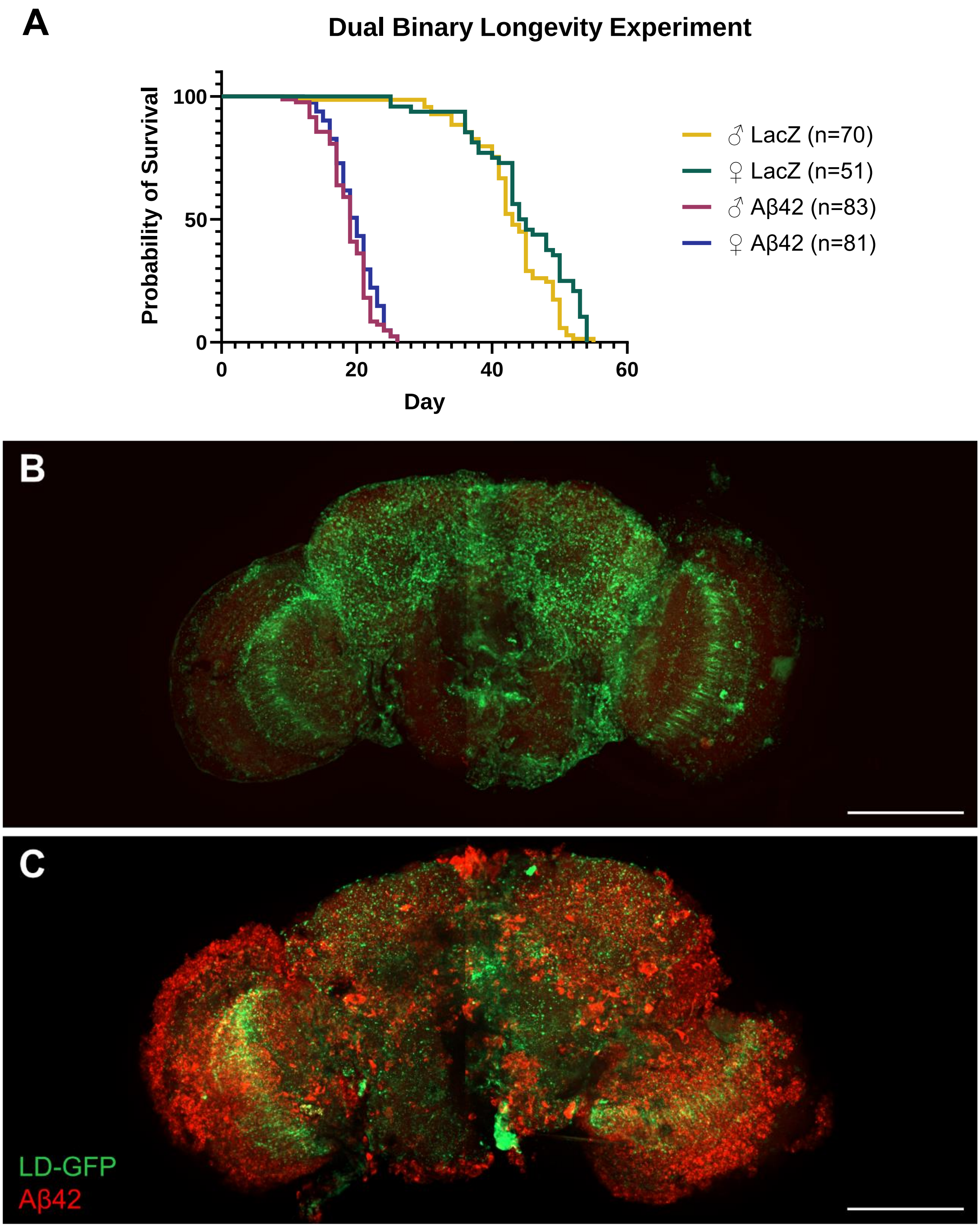

Figure 3.12 Validation of QUAS-Aβ42 insertion.
A) QUAS-Aβ42 expression affects *Drosophila* longevity. Survival curves dual binary flies expressing neuronal (nSyb-QF2) LacZ (control) and Aβ42 via Q-system for both male and female cohorts. Genotype: ♀♂ w^-;UAS-LD-GFP/X;repo-Gal4/nSyb-QF2, where X is either QUAS-LacZ or QUAS-Aβ42 **** = $p \leq 0.0001$, Kaplan-Meier simple survival analysis, Log-rank (Mantel-Cox) test. **B)** Brain deposition of Aβ42 peptides in dual binary flies. Fluorescent images of dissected fly brains stained for Aβ42 peptide aggregates (in red), alongside GFP-tagged glial LDs (in green). A) control LacZ dual binary fly brain and B) Aβ42 dual binary fly brain. Females, 18DPE. 20x lens, 2x1 tile stitching Z stack orthogonal projection. Scale bars: 100 μm

3.3.4. Neuronal expression of Aβ42 drives LD accumulation in *Drosophila* wing glia.

We next sought to determine whether the effects of neuronal Aβ42 toxicity on glial LD homeostasis can be detected using the dual binary model. Similar to the previous experiment, two cohorts of flies were used; flies expressing either Aβ42 or LacZ in neurons via Q-system, along with LD-GFP expressed in glia via Gal4-UAS system.

Indeed, Aβ42 dual binary flies displayed increases in LD characteristics at several timepoints (Figure 3.13). Both number per micron and total area of LD appeared to gradually increase and peak at 7-14DPE in both Aβ42 and LacZ. The number of LD per micron revealed no significant difference at 3 DPE (0.16±0.13 LD/μm for LacZ vs 0.10±0.09 LD/μm for Aβ42, p= 0.6215, Tukey multiple comparisons test, two-way ANOVA) and 18 DPE (0.33±0.11 LD/μm vs 0.28±0.14 LD/μm, P=0.9696, Tukey multiple comparisons test, two-way ANOVA) flies (overall, Time: p<0.0001, F(3, 432)=71.42, Genotype: p<0.0001, F(1, 432)=34.74, Interaction: p<0.0001, F(3, 432)=33.34) (Figure 3.13A). Contrastingly, Aβ42 flies display a significant increase in LDs per micron at both 7 DPE(0.23±0.09 LD/μm vs 0.60±0.31 LD/μm, p<0.0001, Tukey multiple comparisons test, two-way ANOVA) and 14 DPE (0.35±0.13 LD/μm vs 0.53±0.29 LD/μm, p<0.0001, Tukey multiple comparisons test, two-way ANOVA).

Total LD area followed a similar trend, however there was no significant difference observed between the two cohorts at 14 DPE (36.90±17.16 μm^2 vs 41.16±22.10 μm^2, p= 0.7635, Tukey multiple comparisons test, two-way ANOVA) (Figure 3.13B). LacZ flies displayed a higher area of LDs at 18 DPE (39.53±13.92 μm^2 vs 23.25±13.42 μm^2, p= 0.0006, Tukey multiple comparisons test, two-way ANOVA). Furthermore, Aβ42 flies were found to possess a greater LD total area at 7 DPE, when compared to LacZ flies (14.94±6.47 μm^2 vs 43.23±22.22 μm^2, p<0.0001, Tukey multiple comparisons test, two-way ANOVA) (overall, Time: p<0.0001, F(3, 432)=116.2, Genotype: p=0.0172, F(1, 432)=5.717, Interaction: p<0.0001, F(3, 432)=36.97).

The average LD size steadily increased in both cohorts, reaching its peak from 14 DPE and plateauing from there (Figure 3.13C). Interestingly, LacZ flies displayed significantly larger LDs at 14 (0.65±0.16 μm^2 vs 0.50±0.14 μm^2, p<0.0001, Tukey multiple comparisons test, two-way ANOVA) and 18 days (0.75±0.17 μm^2 vs 0.53±0.09 μm^2, p<0.0001, Tukey multiple comparisons test, two-way ANOVA) (overall, Time: p<0.0001, F(3, 432)=224.9, Genotype: p<0.0001, F(1, 432)=50.63, Interaction: p<0.0001, F(3, 432)=24.49).

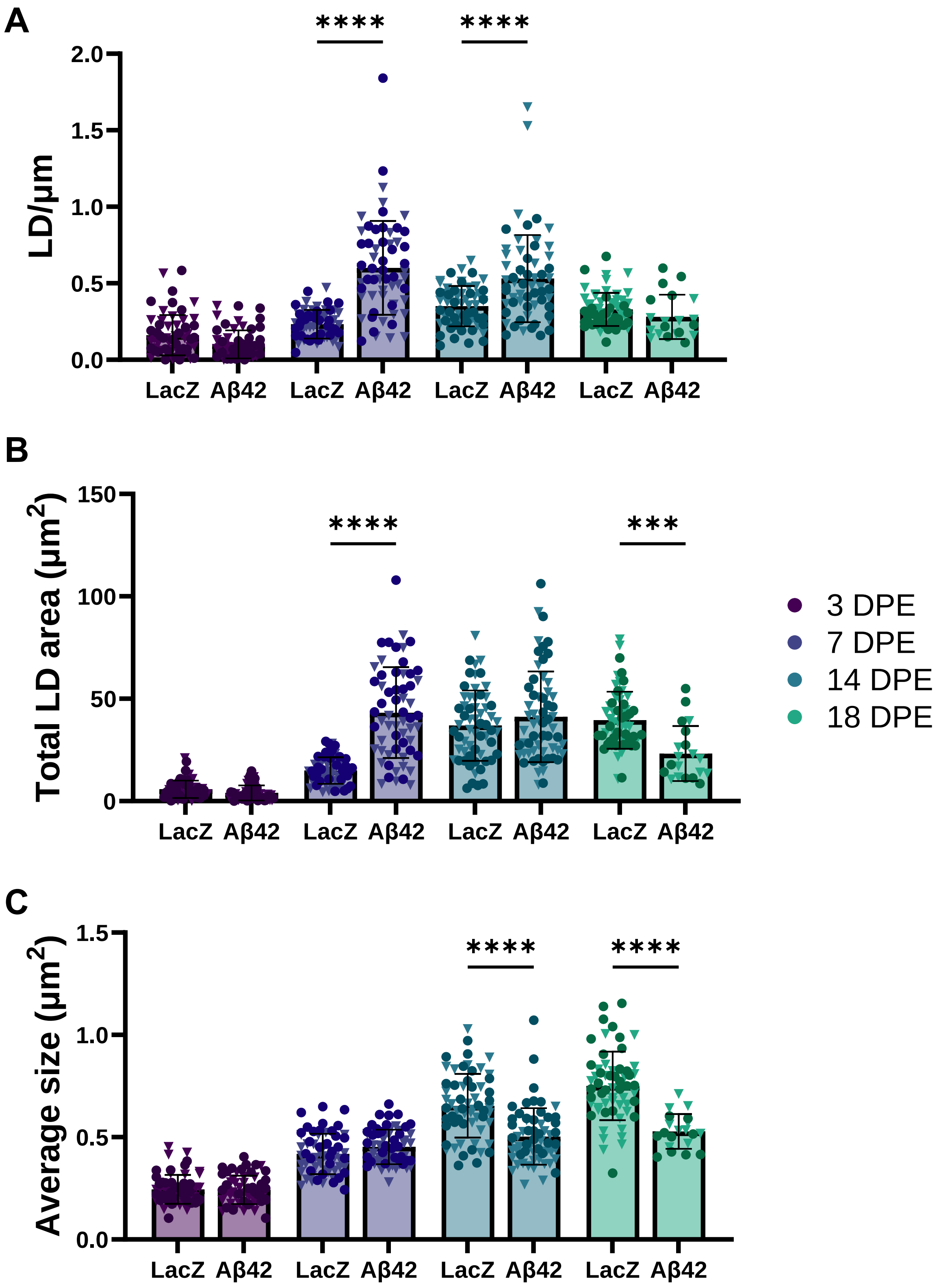

Figure 3.13. Neuronal Aβ42 toxicity affects glia LD homeostasis.
Comparison of glial LD characteristics (**A)** number per micron, **B)** total LD area, **C)** average LD size) when co-expressed with either LacZ or Aβ42 transgenes in neurons. Genotype: ♀♂ w⁻;UAS-LD-GFP/X;repo-Gal4/nSyb-QF2, where X is either QUAS-LacZ or QUAS-Aβ42 N=60 (30 males, 30 females) for all cohorts besides 18DPE Aβ42 (N=20, 10 males, 10 females). Darker circles represent female data points and lighter upturned triangles represent male data. Two-way ANOVA, ns = p>0.05, *** = p≤0.001, **** = p≤0.0001

These results show a similar trend, seen previously in glial expression experiments, with the LD starting off relatively low in early timepoints, increasing and peaking at around midway in the cohorts' lifetime and then decreasing and/or hitting a plateau as the flies reach older timepoints. Aβ42 flies appear to reach their LD peak earlier in their life, and drop quicker compared to LacZ, possibly due to their shorter lifespan.

Despite rather conflicting results, these data suggest that the dual binary model is a valid for studying the effects of neuronal amyloid toxicity on glial LD biology and the intricate interplay of these two cell types in AD aetiology.

4. Discussion

4.1. Overview

In this thesis I established and validated a novel *Drosophila* wing model of lipid droplet homeostasis in glia, in response to amyloid toxicity in AD. I have found that this model is not only responsive to mechanical acute injury and genetic stimuli, but also supports the current research on the role of glial LDs in AD pathology.

Drosophila melanogaster models are widely used in neuroscience research as they present a highly customisable system to interrogate biological processes in a range of diseases. A complete nervous system with a compact, yet relatively complex brain, allowing investigation of AD aetiology in the context of the whole organism, providing an easily modifiable *in vivo* model.

Current methodologies to interrogate LD biology involve timely dissection and staining protocols that do not benefit rapid genetic screening. Here, we developed a fly model that could circumvent this tedious method and provide an alternative way to studying what impact does the interplay between glia and neurons have on lipid homeostasis in AD. We established a novel LD model which takes advantage of readily available GFP constructs, and the convenient and accessible Drosophila fly wing. We found that lipid droplets can be visualised and analysed in a robust manner, which could allow for subsequent screening for lipid-related hit genes implicated in AD pathology. With readily established protocols for axon imaging (Vagnoni and Bullock 2016; Paglione et al. 2020), we established a robust method to visualise LDs in glia that surround these axons. Finally, we have shown that the utilisation of LD-GFP as a fluorescent LD marker creates a viable model for looking at LD changes in fly wing, demonstrating that wing lipid droplets are responsive to mechanical injury and stress, and the effects of amyloid toxicity in accumulation of LDs.

4.2. Pros and Cons of the dual binary model

Drosophila wings are made up of two cuticle sheets fused together along the entirety of the wing, besides the 5 longitudinal veins (L1-L5), with only L1 and L3 containing bundles of mechanosensory neurons accompanied by glial cells. We successfully visualised both of these structures using cell membrane fluorescence staining and picked a suitable ROI for future experiments using LD-GFP (Figure 3.1)

The construct, consisting of UAS-regulated LD-binding domain of *klarsicht* fused with GFP was shown to associate specifically with LDs in *Drosophila* (Yu et al. 2011). The LD-binding domain of *klar* is essential for appropriate LD transport, however without the rest of the protein LD-GFP is functionally inept, albeit still binds to LDs in a similar distribution manner as GFP-tagged *klar*. This suggests that LD-GFP overexpression theoretically should not modulate LD production. Here, we observe significantly more GFP-tagged LDs in dual binary flies and flies solely expressing LD-GFP, when compared to flies expressing LD-GFP alongside another transgene, such as LacZ or Aβ42 within one expression system (Figure 3.7). These findings suggest that availability of transcription activator proteins (Gal4 or QF2) has a direct impact on LD characteristics observed, such as number and total area. We hypothesise that this is likely due to Gal4 binding competition between transgenes, caused by multiple transgene expression by the same activator. This could potentially reduce the efficiency of transgene expression, however existing literature on this topic is limited (Xu et al. 1995; Qiao et al. 2018).

Additionally, a visible variation of fluorescence intensity between different droplets mentioned in Chapter 3.2.1. was also observed previously in the original paper (Yu et al. 2011). Yu et al. (2011) argue that this could be due to the reporter being sequestered by the LDs once they are created and does not readily replenish or move once incorporated into the droplet. Alternatively, LD-GFP could have varied affinity to different lipid droplets, resulting in variation of fluorescent signal, even between neighbouring LDs, possibly due to variation in multiple LD characteristics, such as lipidome and proteome, integrity and aggregates (Welte 2015; Bresgen et al. 2023). Regardless, this could explain the Gal4-related variation described in this thesis and is something that has to be considered when designing experiments using LD-GFP, such as appropriate biological controls. Cuticle hardening and maturation in older flies could also potentially interfere with imaging, preventing the laser light from properly penetrating the surface of the wing.

Original validation of LD-GFP shows that its fluorescence signal largely localises with Nile Red staining, a common histologic stain used for staining neutral lipids (Greenspan et al. 1985; Yu et al. 2011). However, unlike the solid LD staining with Nile Red, LD-GFP appears to form a ring around LDs, as it binds the membrane of the LD and is not able to penetrate into the organelle (Yu et al. 2011), which we have also noticed with bigger or less bright LDs (best evident at Figure 3.2). This difference in visualisation may impact the area data readout, hence another way of quantifying LDs could be beneficial to verify the findings using this model. There is no existing literature describing staining of adult fly wings with antibodies or histology stains. This is likely due to the low permeability and hydrophobic properties of chitin, which composes the fly wing, which would prevent any stains from permeating into the wing beyond its surface (Gonil and Sajomsang 2012). Some staining agents could potentially access the veins through the area where the wing is cut, but it would take a long time for diffusion down the wing, given that it is possible in the first place. Despite extensive literature available on pupal wing staining (Bolatto et al. 2017; Thuma et al. 2018), this timepoint might not be suitable for studying neurodegeneration, as we shown that Aβ42 neurotoxicity effect does not manifest itself fully during the early stages of the fly imago life cycle.

As an alternative to wing staining, the findings of this model could be also validated by traditional brain staining, as well as lipid quantification assays, using fly head lysates. This method could be used to assess levels of neutral and peroxidated lipids. Although LD-GFP appears to be LD-specific, another method of LD staining could be a crucial control measure, ensuring specificity of the fluorescence output, especially when introducing transgenes. These limitations in staining and visualising adult fly wings further highlights this model as a potential method of lipid droplet homeostasis research.

Fluorescence intensity of LD-GFP in the wing presented with variability (Figure 3.2) with no obvious causative factor driving this variance. This ultimately led to an inability to set any specific thresholding during analysis, which could help in remaining consistent between samples. Some LDs would be dimmer, yet still distinguishable from the background, with other images being significantly brighter overall. Subsequently parameters for detecting fluorescence intensity values could not be standardised, introducing potential areas for bias in analysis. When thresholding for LD selection, deciding on the lowest fluorescence value to be considered as a LD can cause slight variation in the overall highlighted area, potentially skewing LD readouts. This was combated by increasing the number of flies for each experiment, phenotype blinding, measuring for several LD characteristics, and being cautious regarding weak differences between phenotypes. This issue could also be addressed by attempting to use different analysis software, for example Ilastik (Ilastik team, Berg et al. 2019). Ilastik is analysis software allowing for algorithmic separation of cells and other structures, such as organelles (Berg et al. 2019), which utilizes machine learning and has previously been successfully used for LD quantification in cell and *Drosophila* models (Dumesnil et al. 2023; Grepper et al. 2023; Li et al. 2023; Haynes et al. 2024). Utilisation of machine learning could provide a more accurate quantification method, considering the variability in LD brightness and our inability to select them properly via thresholding (Sheneman et al. 2021).

Three LD characteristics were measured the wing micrographs: quantity (number per micron of the vein within the ROI), area (within the ROI), and average LD size. The number of LDs was quantified specifically per ROI as wings would occasionally tilt when the coverslip was mounted, resulting in less vein visible within the ROI. Average size data was also prone to potential skewing, as fewer large LDs were present relative to the mean LD size. More LD metrics increase the likelihood of an observed result being due to changes in LDs rather than data skewness or any other error, thus when drawing conclusions, we considered all three metrics used in the thesis.

Another possible caveat of utilising the wing model in neurodegeneration research is that fly wing neurons are sensory, thus belonging to the PNS (Murray et al. 1984). Albeit useful and accessible, this neurodegeneration model might not be suitable for studying cellular mechanisms specific for the central nervous system CNS, which has to be considered during experimental design. For example, the recent findings by Haynes et al. suggest that sleep deprivation in *Drosophila* prevents the peroxidated lipid shuttling from glia to neurons, which appears to happen during sleep (Haynes et al. 2024). It is not clear how well these findings could translate to our wing model, as it is not certain that sensory neurons would experience a similar effect from prolonged wake. If this factor is a major contributor towards LD homeostasis disturbance, our proposed model would likely have severe limitations when used to investigate this mechanism. However, this means that our wing model could also be utilised to look at peripheral axon disorders, such as Hereditary sensory neuropathy type 1 (HSN-1) (Marshall et al. 2014) and Charcot-Marie Tooth type 2B (CMT2B) peripheral neuropathy (Giudetti et al. 2020; Prior et al. 2023), with lipid metabolism, homeostasis and myelin structural integrity highly dysregulated in both disorders.

Despite the shortcomings, this wing imaging model still offers a flexible and high-throughput way to study glial lipid droplet biology. We show that LDs are visible, and their characteristics do not undergo significant changes for up to 120 mins after dissection (Figure 3.2), providing ample time for sample preparation and imaging in larger cohorts. It is also worth mentioning that some of this decrease can be attributed to fluorescence photobleaching, as the same ROIs were imaged every 15 mins, potentially causing some of GFP to degrade in the process. Up to 20 wings at a time were imaged during this project and no significant inconsistencies between first and last wings of the batch were apparent. This, taken with the comparatively easy procedure of dissecting wings and no requirement for fixation and additional staining, allows to drastically increase the sample size, when compared to conventional imaging approaches such as using the *Drosophila* brain. Ultimately, we envision the utilisation of this model in gene screening, for example, investigation of the effects that AD GWAS risk gene expression might have on LD homeostasis in the context of AD pathology. It is becoming evident that several genes are directly linked to lipid metabolism and transport (Kawade and Yamanaka 2024), in addition to apolipoprotein transporter APOEε4, which is the largest risk factor of LOAD discovered so far (Genin et al. 2011; Bellenguez et al. 2022). Recent findings suggesting involvement of neuronal tauopathy to glial LD accumulation (Li et al. 2024), similarly to amyloid toxicity, could be further investigated by introducing tau to our dual binary wing model. Furthermore, the LD-GFP model could be utilised when researching other lipid homeostasis dysfunction-related diseases, such as Niemann-Pick Type C1 (Cruz et al. 2000).

4.3. Modelling Wallerian degeneration via axotomy

Fly wing injury experiment were utilised as a means to validate the responses of this model to acute injury. The injury, involving perpendicularly cutting the wing in half, results in a drastic increase in LD number and total area in all tested cohorts at 48h post injury (Figure 3.4). The LD could be observed at earlier (24h PI) and later (72h PI) timepoints (Figure 3.3), however with a decrease in some LD characteristics when compared to 48h PI, as well as more LDs appearing dimmer on fluorescence images. This could be attributed to a potential temporal delay of wing glia engulfing neuronal debris and processing it, reaching their prime phagocytic activity at around 48h PI. Overall, these results shown that the LD-GFP wing model of LD homeostasis is responsive to external stimuli and extreme acute injury, demonstrating the responsiveness of the model.

This phenotype was hypothesised to be caused by axon severance in fly wing veins neuron bundles leading to Wallerian degeneration (Rotshenker 2011), which would subsequently initiate the uptake of neuronal debris by glia and increase the LD production. Wallerian degeneration (WD) is a mechanism of axonal death, leading to axonal fragmentation and subsequent glial engulfment, dysregulation of which is thought to be involved in several neurodegenerative diseases, including AD (Wang et al. 2012; Coleman and Höke 2020; Dan and Zhang 2023). Furthermore, it was previously shown that loss of function of TREM2, a major mediator of lipid sensing and myelin debris phagocytosis in microglia, as well as an AD risk gene, negatively impacts the ability of microglia to cope with and clear accumulating cholesterol esters produced as a result (Damisah et al. 2020; Nugent et al. 2020). Successful establishing of a model for studying glial engulfment of neuronal debris could allow us to further investigate this process, unravelling the involvement of this mechanism is AD pathology.

4.4. Regulation of glial phagocytosis by *draper*

With acute injury effect on LD homeostasis proven in the wing model, we sought to examine whether this phenotype could be modulated by altering *draper* expression, a key regulator of phagocytosis in *Drosophila*. Published literature suggests that *draper* is essential for glial clearance of severed axons in *Drosophila* ventral nerve cord (MacDonald et al. 2006; Purice et al. 2017), is dependent on PI3K signalling (Purice et al. 2016), and activates JNK signalling in fly glia (Lu et al. 2017) initiating phagocytosis. We discovered that overexpression of *draper* in wing glia, along with LD-GFP, led to an increased LD accumulation response to injury when compared to injured control wings (Figure 3.6). Interestingly, RNAi knockdown of *draper* did not impact the LD homeostasis upon injury (Figure 3.6). Considering the importance of *draper* in the glial response to WD, these results could imply several possibilities. The knockdown strength of the RNAi line must be assessed by qPCR, albeit proven effective in previous laboratory experiments, and other knockdown methods tested to validate these findings. To observe an effect on glial phagocytosis, a stronger knockdown of *draper* is potentially required, with null allele knockout fly lines commercially available. Further investigation of WD processes could clarify these findings, the effects of which on LD homeostasis could be explored using our wing model. WD prevention via Wld^S introduction (Coleman and Freeman 2010), Sarm1 knockdown (Gilley et al. 2017) and NMNAT overexpression (Sasaki et al. 2016), and their effect on glial LD homeostasis would be the first steps in exploring the relevancy of this mechanism in AD pathology. Improved understanding the molecular mechanisms behind WD could provide useful insight on injury-related illnesses, such as traumatic brain injury, as well as neurodegenerative diseases, such as Parkinson's (Loring and Thompson 2020).

As an injury modelling method, wing dissection was proven to be a reliable basic method of injury induction, that does not require reagents or elaborate laboratory equipment to perform. Reproducibility was one of the shortcomings of this method, as it was difficult to accurately make incisions across wing ROIs, hence some variability in the majority LD localisation within the ROI was expected, as they were mostly found in close proximity to the injury region.

4.5. Modelling amyloid toxicity

The response of the model to a more gradual neurodegenerative insult was assessed by introducing Aβ42 expression in glia, alongside LD-GFP. Subsequently, the introduction of two binary expression systems allowed for differential spatiotemporal transgene expression has not been previously addressed in the existing literature, adding an extra level of flexibility and customisation to this model. It has also enabled us to examine how this model fits within our current understanding of lipid biology dysfunction in AD, namely the neuron-glia interaction aspect.

Our results show a trend, where LD accumulation peaks around midlife in Aβ42 flies and decreases towards the end of their lifespan, showing significantly higher peaks compared to LacZ controls. This trend was observed in both flies expressing Aβ42/LacZ in glia (Figure 3.8) and neurons (Figure 3.13). These findings, in line with the current hypothesis on LD pathophysiology, could potentially suggest that increase in amyloid toxicity renders neurons unable to cope with ROS and facilitate adequate transport of LDs to glia, thus eliminating a mechanism of ROS efflux, ultimately leading to neurodegeneration.

The trend, which was also observed in sole glial expression experiments, would not make as much sense, however, a decrease in LD homeostasis could be a hallmark of aging in *Drosophila*. Recent study suggest that a depletion in lipid storage is observed in moribund flies (Hofbauer et al. 2021), thus it can be speculated that a decrease in LDs could be observed in aged flies. Furthermore, increasing thickness of the wing chitin over time could potentially restrict fluorescence imaging, decreasing the number and area of visible LDs as the flies age. Wing "wear and tear" is also to be expected in older flies, as *Drosophila* actively utilise wings for multiple behavioural actions, such as courting and aggression (Bennet-Clark and Ewing 1968; Davis et al. 2018), which could lead to accumulative damage to the wings, especially in male flies.

Interestingly, smaller LDs were observed in Aβ42 dual binary flies, when compared to the LacZ controls, contrary to sole glial expression, where Aβ42 flies generally displayed larger LDs. Several studies investigating LDs in hepatocytes and adipocytes report LDs regulating their size and morphology in response to a variety of stimuli, such as increase synthesis of neutral lipids, lysosomal activity and lipolysis (Yang et al. 2012; Schott et al. 2019). With lipophagy involvement in AD remaining unclear, it would be an interesting prospect

Ultimately, the final major findings of this thesis show that both glial and neuronal expression of Aβ42 leads to accumulation of LD in fly wing glia at higher numbers of LDs and earlier timepoints, when compared to control flies (Figures 3.8 & 3.13). These results are in line with our current understanding that LDs accumulate in glial cells as a result of increased peroxidation of lipids in neurons and their subsequent efflux into microglia and astrocytes by APOE in form of LDs (Ioannou et al. 2019; Lee et al. 2021; Moulton et al. 2021; Windham et al. 2023; Haynes et al. 2024). The harmful increase in neuronal ROS through amyloid toxicity and mitochondrial dysfunction is regulated in neurons by increased lipid production, which in turn react with these radicals, and reduces the overall oxidative stress and shifting it to glial cells. It appears that disruption of this shuttling between neurons and glia results in neurotoxicity and neurodegeneration, a hallmark of AD (Liu et al. 2017). Interestingly, it was recently shown that the accumulation of LDs by microglia in response to tau aggregation, another crucial hallmark of AD, is controlled by AMP-activated protein kinase (AMPK) expression in neurons (Li et al. 2024). Inhibition of neuronal AMPK promoted LD accumulation and microglia-induced inflammation, suggesting a neuroprotective effect of the kinase activity. Liver X receptor (LXR) agonists and Abca1 overexpression were also shown to alleviate tau-induced neurodegeneration and accumulation of LDs (Litvinchuk et al. 2024). Together with previously established effect of Abca1 activity on LD homeostasis (Moulton et al. 2021), it becomes clear that lipid metabolism and transport, namely their efflux from neurons, is a key modulating factor of neurodegeneration in AD.

Most recent published work, suggests that this peroxidated lipid shuttling to glia happens at night and alleviates the build-up of oxidative stress, that accumulates in neurons during the wake due to an increased activity (Goodman et al. 2024; Haynes et al. 2024). On the other hand, recent studies show that in fact this glial LD accumulation leads to increased glial reactivity, which could be damaging to neurons (Haney et al. 2024). Furthermore, increased accumulation of glial LD has been shown to impair microglial surveillance and interaction with neurons (Victor et al. 2022). Altogether, it is clear that the role of glial lipid homeostasis is a complex multifaceted mechanism which is not entirely understood thus, highlighting the requirement for more refined models to explore mechanism.

4.6. Future directions

Further characterisation of the model is the main priority in the future work. Although the findings using our wing model align with our current understanding of LD dysfunction in AD, it is important to validate these findings via other systems. This characterisation is especially important, considering PNS neurons utilised in this model, and their possible discrepancies from CNS neurons. Once a complimentary lipid quantification assay is established, and the outputs of the model are validated, it can then be used as a more standalone method of LD homeostasis analysis, allowing to further investigate glial lipid-associated AD pathology using *Drosophila* wings.

The machinery of the dual binary model needs to be reintroduced on different chromosomes, to allow for more flexibility when selecting transgenes for expression. Currently, the model is limited to transgene insertion on the 3rd chromosome, however further line building could allow for 2nd chromosome insertion, thus incorporating more commercially available *Drosophila* transgenes. The cell type expressing Aβ42 could also be changed, for example, allowing for investigation whether glial amyloid toxicity has any effect on neuronal health. Additionally, use of more specific glial drivers, such as GMR86E01-Gal4 for astrocyte-like glia and GMR56F03-Gal4 for ensheathing glia, could allow for use of the dual binary model in dissecting the exact roles of these cell types in AD (Kremer et al. 2017; Sheng et al. 2023). Furthermore, the binary system gene expression machinery is introduced into both copies of the 2nd and 3rd chromosomes, which significantly limits the potential for introducing additional transgenes. Therefore, homologous recombination must be performed to combine the expression system components onto the same chromosome, freeing space for more insertions. Ultimately this could refine the model, further increasing its flexibility and utility.

Once these steps are completed we are looking to utilise this model as a part of an AD risk gene RNAi screen, examining how knockdown of lipid-related risk genes affects LD homeostasis in the context of Aβ42 and tau toxicity.

4.7. Conclusions

I have successfully established a model for studying effects of Aβ42 toxicity and peripheral nerve injury on glial LD homeostasis using *Drosophila* wing imaging. The model utilises two gene expression systems, allowing for flexible spatiotemporal expression of transgenes in distinct cell types. The observed LD phenotype was responsive to mechanical axotomy and amyloid toxicity, proving this model suitable for screening and is in line with the current consensus in the field. Further refinement of this model would allow its utilisation in high-throughput genetic screening of the effects of AD risk genes on lipid droplet homeostasis and its involvement in neurodegeneration.

References

Adams, M.D. et al. 2000. The genome sequence of Drosophila melanogaster. *Science (New York, N.Y.)* 287(5461), pp. 2185–2195. doi: 10.1126/science.287.5461.2185.

Al-Ghraiybah, N.F., Wang, J., Alkhalifa, A.E., Roberts, A.B., Raj, R., Yang, E. and Kaddoumi, A. 2022. Glial Cell-Mediated Neuroinflammation in Alzheimer's Disease. *International Journal of Molecular Sciences* 23(18), p. 10572. doi: 10.3390/ijms231810572.

Alvarez, J.I., Katayama, T. and Prat, A. 2013. Glial influence on the Blood Brain Barrier. *Glia* 61(12), pp. 1939–1958. doi: 10.1002/glia.22575.

Arber, C., Lovejoy, C. and Wray, S. 2017. Stem cell models of Alzheimer's disease: progress and challenges. *Alzheimer's Research & Therapy* 9(1), p. 42. doi: 10.1186/s13195-017-0268-4.

Atri, A. 2019. The Alzheimer's Disease Clinical Spectrum: Diagnosis and Management. *Medical Clinics* 103(2), pp. 263–293. doi: 10.1016/j.mcna.2018.10.009.

Bales, K.R. et al. 1997. Lack of apolipoprotein E dramatically reduces amyloid beta-peptide deposition. *Nature Genetics* 17(3), pp. 263–264. doi: 10.1038/ng1197-263.

Bateman, R.J. et al. 2012. Clinical and Biomarker Changes in Dominantly Inherited Alzheimer's Disease. *The New England journal of medicine* 367(9), pp. 795–804. doi: 10.1056/NEJMoa1202753.

Behura, S.K. and Severson, D.W. 2013. Codon usage bias: causative factors, quantification methods and genome-wide patterns: with emphasis on insect genomes. *Biological Reviews of the Cambridge Philosophical Society* 88(1), pp. 49–61. doi: 10.1111/j.1469-185X.2012.00242.x.

Bélanger, M., Allaman, I. and Magistretti, P.J. 2011. Brain Energy Metabolism: Focus on Astrocyte-Neuron Metabolic Cooperation. *Cell Metabolism* 14(6), pp. 724–738. doi: 10.1016/j.cmet.2011.08.016.

Bell, R.D. et al. 2012. Apolipoprotein E controls cerebrovascular integrity via cyclophilin A. *Nature* 485(7399), pp. 512–516. doi: 10.1038/nature11087.

Bellen, H.J., Tong, C. and Tsuda, H. 2010. 100 years of Drosophila research and its impact on vertebrate neuroscience: a history lesson for the future. *Nature Reviews Neuroscience* 11(7), pp. 514–522. doi: 10.1038/nrn2839.

Bellenguez, C. et al. 2022. New insights into the genetic etiology of Alzheimer's disease and related dementias. *Nature Genetics* 54(4), pp. 412–436. doi: 10.1038/s41588-022-01024-z.

Bello, B., Resendez-Perez, D. and Gehring, W.J. 1998. Spatial and temporal targeting of gene expression in Drosophila by means of a tetracycline-dependent transactivator system. *Development (Cambridge, England)* 125(12), pp. 2193–2202. doi: 10.1242/dev.125.12.2193.

Bennet-Clark, H.C. and Ewing, A.W. 1968. The Wing Mechanism Involved in the Courtship of Drosophila. *Journal of Experimental Biology* 49(1), pp. 117–128. doi: 10.1242/jeb.49.1.117.

Berchtold, N.C. and Cotman, C.W. 1998. Evolution in the Conceptualization of Dementia and Alzheimer's Disease: Greco-Roman Period to the 1960s. *Neurobiology of Aging* 19(3), pp. 173–189. doi: 10.1016/S0197-4580(98)00052-9.

Berg, S. et al. 2019. ilastik: interactive machine learning for (bio)image analysis. *Nature Methods* 16(12), pp. 1226–1232. doi: 10.1038/s41592-019-0582-9.

Blanchard, J.W. et al. 2022. APOE4 impairs myelination via cholesterol dysregulation in oligodendrocytes. *Nature* 611(7937), pp. 769–779. doi: 10.1038/s41586-022-05439-w.

Bolatto, C., Parada, C. and Colmenares, V. 2017. A Rapid and Efficient Method to Dissect Pupal Wings of Drosophila Suitable for Immunodetections or PCR Assays. *Journal of Visualized Experiments : JoVE* (130), p. 55854. doi: 10.3791/55854.

Boyles, J.K., Notterpek, L.M. and Anderson, L.J. 1990. Accumulation of apolipoproteins in the regenerating and remyelinating mammalian peripheral nerve. Identification of apolipoprotein D, apolipoprotein A-IV, apolipoprotein E, and apolipoprotein A-I. *Journal of Biological Chemistry* 265(29), pp. 17805–17815. doi: 10.1016/S0021-9258(18)38235-8.

Braak, H. and Braak, E. 1985. On areas of transition between entorhinal allocortex and temporal isocortex in the human brain. Normal morphology and lamina-specific pathology in Alzheimer's disease. *Acta Neuropathologica* 68(4), pp. 325–332. doi: 10.1007/BF00690836.

Braak, H. and Braak, E. 1991. Neuropathological stageing of Alzheimer-related changes. *Acta Neuropathologica* 82(4), pp. 239–259. doi: 10.1007/BF00308809.

Brand, A.H. and Perrimon, N. 1993. Targeted gene expression as a means of altering cell fates and generating dominant phenotypes. *Development* 118(2), pp. 401–415. doi: 10.1242/dev.118.2.401.

Bresgen, N., Kovacs, M., Lahnsteiner, A., Felder, T.K. and Rinnerthaler, M. 2023. The Janus-Faced Role of Lipid Droplets in Aging: Insights from the Cellular Perspective. *Biomolecules* 13(6), p. 912. doi: 10.3390/biom13060912.

Brzecka, A. et al. 2018. Sleep Disorders Associated With Alzheimer's Disease: A Perspective. *Frontiers in Neuroscience* 12, p. 330. doi: 10.3389/fnins.2018.00330.

Busche, M.A. and Hyman, B.T. 2020. Synergy between amyloid-β and tau in Alzheimer's disease. *Nature Neuroscience* 23(10), pp. 1183–1193. doi: 10.1038/s41593-020-0687-6.

Byrns, C.N. et al. 2024. Senescent glia link mitochondrial dysfunction and lipid accumulation. *Nature* 630(8016), pp. 475–483. doi: 10.1038/s41586-024-07516-8.

Carmine-Simmen, K., Proctor, T., Tschäpe, J., Poeck, B., Triphan, T., Strauss, R. and Kretzschmar, D. 2009. Neurotoxic effects induced by the Drosophila amyloid-β peptide suggest a conserved toxic function. *Neurobiology of disease* 33(2), pp. 274–281. doi: 10.1016/j.nbd.2008.10.014.

Chen, G., Xu, T., Yan, Y., Zhou, Y., Jiang, Y., Melcher, K. and Xu, H.E. 2017. Amyloid beta: structure, biology and structure-based therapeutic development. *Acta Pharmacologica Sinica* 38(9), pp. 1205–1235. doi: 10.1038/aps.2017.28.

Cline, E.N., Bicca, M.A., Viola, K.L. and Klein, W.L. 2018. The Amyloid-β Oligomer Hypothesis: Beginning of the Third Decade. *Journal of Alzheimer's Disease* 64(Suppl 1), pp. S567–S610. doi: 10.3233/JAD-179941.

Coleman, M.P. and Freeman, M.R. 2010. Wallerian Degeneration, WldS, and Nmnat. *Annual review of neuroscience* 33, pp. 245–267. doi: 10.1146/annurev-neuro-060909-153248.

Coleman, M.P. and Höke, A. 2020. Programmed axon degeneration: from mouse to mechanism to medicine. *Nature Reviews Neuroscience* 21(4), pp. 183–196. doi: 10.1038/s41583-020-0269-3.

Corder, E.H. et al. 1993. Gene Dose of Apolipoprotein E Type 4 Allele and the Risk of Alzheimer’s Disease in Late Onset Families. *Science* 261(5123), pp. 921–923. doi: 10.1126/science.8346443.

Crowther, D.C., Page, R., Chandraratna, D. and Lomas, D.A. 2006. A Drosophila model of Alzheimer’s disease. *Methods in Enzymology* 412, pp. 234–255. doi: 10.1016/S0076-6879(06)12015-7.

Cruz, J.C., Sugii, S., Yu, C. and Chang, T.-Y. 2000. Role of Niemann-Pick Type C1 Protein in Intracellular Trafficking of Low Density Lipoprotein-derived Cholesterol*. *Journal of Biological Chemistry* 275(6), pp. 4013–4021. doi: 10.1074/jbc.275.6.4013.

Cummings, J. 2023. Anti-Amyloid Monoclonal Antibodies are Transformative Treatments that Redefine Alzheimer’s Disease Therapeutics. *Drugs* 83(7), pp. 569–576. doi: 10.1007/s40265-023-01858-9.

Cutler, T. et al. 2015. Drosophila Eye Model to Study Neuroprotective Role of CREB Binding Protein (CBP) in Alzheimer’s Disease. *PLoS ONE* 10(9), p. e0137691. doi: 10.1371/journal.pone.0137691.

Damisah, E.C., Rai, A. and Grutzendler, J. 2020. TREM2: Modulator of Lipid Metabolism in Microglia. *Neuron* 105(5), pp. 759–761. doi: 10.1016/j.neuron.2020.02.008.

Dan, L. and Zhang, Z. 2023. Alzheimer’s disease: an axonal injury disease? *Frontiers in Aging Neuroscience* 15. Available at: https://www.frontiersin.org/articles/10.3389/fnagi.2023.1264448 [Accessed: 2 May 2024].

Davis, S.M., Thomas, A.L., Liu, L., Campbell, I.M. and Dierick, H.A. 2018. Isolation of Aggressive Behavior Mutants in Drosophila Using a Screen for Wing Damage. *Genetics* 208(1), pp. 273–282. doi: 10.1534/genetics.117.300292.

De Strooper, B. et al. 1998. Deficiency of presenilin-1 inhibits the normal cleavage of amyloid precursor protein. *Nature* 391(6665), pp. 387–390. doi: 10.1038/34910.

De Strooper, B. and Karran, E. 2016. The Cellular Phase of Alzheimer’s Disease. *Cell* 164(4), pp. 603–615. doi: 10.1016/j.cell.2015.12.056.

DeTure, M.A. and Dickson, D.W. 2019. The neuropathological diagnosis of Alzheimer’s disease. *Molecular Neurodegeneration* 14(1), p. 32. doi: 10.1186/s13024-019-0333-5.

Diaz, A.L. and Gleeson, J.G. 2009. The Molecular and Genetic Mechanisms of Neocortex Development. *Clinics in Perinatology* 36(3), pp. 503–512. doi: 10.1016/j.clp.2009.06.008.

Doherty, J., Logan, M.A., Taşdemir, O.E. and Freeman, M.R. 2009. Ensheathing glia function as phagocytes in the adult Drosophila brain. *The Journal of Neuroscience: The Official Journal of the Society for Neuroscience* 29(15), pp. 4768–4781. doi: 10.1523/JNEUROSCI.5951-08.2009.

Dorkenwald, S. et al. 2023. Neuronal wiring diagram of an adult brain. p. 2023.06.27.546656. Available at: https://www.biorxiv.org/content/10.1101/2023.06.27.546656v2 [Accessed: 5 February 2024].

Duan, J. et al. 2024. Alzheimer's disease risk allele of PICALM causes detrimental lipid droplets in microglia. Available at: https://www.researchsquare.com/article/rs-4407146/v1 [Accessed: 27 May 2024].

Dumesnil, C. et al. 2023. Cholesterol esters form supercooled lipid droplets whose nucleation is facilitated by triacylglycerols. *Nature Communications* 14(1), p. 915. doi: 10.1038/s41467-023-36375-6.

Farias, S.T., Mungas, D., Reed, B.R., Harvey, D. and DeCarli, C. 2009. Progression of Mild Cognitive Impairment to Dementia in Clinic- vs Community-Based Cohorts. *Archives of neurology* 66(9), pp. 1151–1157. doi: 10.1001/archneurol.2009.106.

Farmer, B.C., Walsh, A.E., Kluemper, J.C. and Johnson, L.A. 2020. Lipid Droplets in Neurodegenerative Disorders. *Frontiers in Neuroscience* 14. Available at: https://www.frontiersin.org/journals/neuroscience/articles/10.3389/fnins.2020.00742/full [Accessed: 24 May 2024].

Fitz, N.F. et al. 2021. Phospholipids of APOE lipoproteins activate microglia in an isoform-specific manner in preclinical models of Alzheimer's disease. *Nature Communications* 12(1), p. 3416. doi: 10.1038/s41467-021-23762-0.

Fortea, J. et al. 2024. APOE4 homozygozity represents a distinct genetic form of Alzheimer's disease. *Nature Medicine* 30(5), pp. 1284–1291. doi: 10.1038/s41591-024-02931-w.

Fortini, M.E., Skupski, M.P., Boguski, M.S. and Hariharan, I.K. 2000. A survey of human disease gene counterparts in the Drosophila genome. *The Journal of Cell Biology* 150(2), pp. F23-30. doi: 10.1083/jcb.150.2.f23.

Freeman, M.R. 2015. Drosophila Central Nervous System Glia. *Cold Spring Harbor Perspectives in Biology* 7(11), p. a020552. doi: 10.1101/cshperspect.a020552.

Fujimoto, T. and Parton, R.G. 2011. Not Just Fat: The Structure and Function of the Lipid Droplet. *Cold Spring Harbor Perspectives in Biology* 3(3), p. a004838. doi: 10.1101/cshperspect.a004838.

Genin, E. et al. 2011. APOE and Alzheimer disease: a major gene with semi-dominant inheritance. *Molecular Psychiatry* 16(9), pp. 903–907. doi: 10.1038/mp.2011.52.

Gilley, J., Ribchester, R.R. and Coleman, M.P. 2017. Sarm1 Deletion, but Not WldS, Confers Lifelong Rescue in a Mouse Model of Severe Axonopathy. *Cell Reports* 21(1), pp. 10–16. doi: 10.1016/j.celrep.2017.09.027.

Giudetti, A.M. et al. 2020. An altered lipid metabolism characterizes Charcot-Marie-Tooth type 2B peripheral neuropathy. *Biochimica Et Biophysica Acta. Molecular and Cell Biology of Lipids* 1865(12), p. 158805. doi: 10.1016/j.bbalip.2020.158805.

Goate, A. et al. 1991. Segregation of a missense mutation in the amyloid precursor protein gene with familial Alzheimer's disease. *Nature* 349(6311), pp. 704–706. doi: 10.1038/349704a0.

Gonil, P. and Sajomsang, W. 2012. Applications of magnetic resonance spectroscopy to chitin from insect cuticles. *International Journal of Biological Macromolecules* 51(4), pp. 514–522. doi: 10.1016/j.ijbiomac.2012.06.025.

Goodman, L.D. and Bellen, H.J. 2022. Recent insights into the role of glia and oxidative stress in Alzheimer's disease gained from Drosophila. *Current Opinion in Neurobiology* 72, pp. 32–38. doi: 10.1016/j.conb.2021.07.012.

Goodman, L.D., Moulton, M.J. and Bellen, H.J. 2024. Glial lipid droplets resolve ROS during sleep. *Nature Neuroscience* 27(4), pp. 610–612. doi: 10.1038/s41593-023-01546-7.

Graff-Radford, N.R. et al. 2007. Association of low plasma Abeta42/Abeta40 ratios with increased imminent risk for mild cognitive impairment and Alzheimer disease. *Archives of Neurology* 64(3), pp. 354–362. doi: 10.1001/archneur.64.3.354.

Gravina, S.A. et al. 1995. Amyloid beta protein (A beta) in Alzheimer's disease brain. Biochemical and immunocytochemical analysis with antibodies specific for forms ending at A beta 40 or A beta 42(43). *The Journal of Biological Chemistry* 270(13), pp. 7013–7016. doi: 10.1074/jbc.270.13.7013.

Greenberg, S.M., Bacskai, B.J., Hernandez-Guillamon, M., Pruzin, J., Sperling, R. and van Veluw, S.J. 2020. Cerebral amyloid angiopathy and Alzheimer disease — one peptide, two pathways. *Nature Reviews Neurology* 16(1), pp. 30–42. doi: 10.1038/s41582-019-0281-2.

Greenspan, P., Mayer, E.P. and Fowler, S.D. 1985. Nile red: a selective fluorescent stain for intracellular lipid droplets. *The Journal of Cell Biology* 100(3), pp. 965–973. doi: 10.1083/jcb.100.3.965.

Grepper, D., Tabasso, C., Aguettaz, A.K.F., Martinotti, A., Ebrahimi, A., Lagarrigue, S. and Amati, F. 2023. Methodological advancements in organ-specific ectopic lipid quantitative characterization: Effects of high fat diet on muscle and liver intracellular lipids. *Molecular Metabolism* 68, p. 101669. doi: 10.1016/j.molmet.2023.101669.

Hampel, H. et al. 2021. The Amyloid-β Pathway in Alzheimer's Disease. *Molecular Psychiatry* 26(10), pp. 5481–5503. doi: 10.1038/s41380-021-01249-0.

Haney, M.S. et al. 2024. APOE4/4 is linked to damaging lipid droplets in Alzheimer's disease microglia. *Nature* 628(8006), pp. 154–161. doi: 10.1038/s41586-024-07185-7.

Hansen, D.V., Hanson, J.E. and Sheng, M. 2018. Microglia in Alzheimer's disease. *The Journal of Cell Biology* 217(2), pp. 459–472. doi: 10.1083/jcb.201709069.

Hardy, J. and Selkoe, D.J. 2002. The Amyloid Hypothesis of Alzheimer's Disease: Progress and Problems on the Road to Therapeutics. *Science* 297(5580), pp. 353–356. doi: 10.1126/science.1072994.

Hardy, J.A. and Higgins, G.A. 1992. Alzheimer's Disease: The Amyloid Cascade Hypothesis. *Science* 256(5054), pp. 184–185. doi: 10.1126/science.1566067.

Haruwaka, K. et al. 2019. Dual microglia effects on blood brain barrier permeability induced by systemic inflammation. *Nature Communications* 10(1), p. 5816. doi: 10.1038/s41467-019-13812-z.

Haynes, P.R. et al. 2024. A neuron–glia lipid metabolic cycle couples daily sleep to mitochondrial homeostasis. *Nature Neuroscience* 27(4), pp. 666–678. doi: 10.1038/s41593-023-01568-1.

He, Z. et al. 2018. Amyloid-β plaques enhance Alzheimer's brain tau-seeded pathologies by facilitating neuritic plaque tau aggregation. *Nature Medicine* 24(1), pp. 29–38. doi: 10.1038/nm.4443.

Herrera-Rivero, M. 2013. Late-Onset Alzheimer's Disease: Risk Factors, Clinical Diagnosis and the Search for Biomarkers. In: *Neurodegenerative Diseases*. IntechOpen. Available at: https://www.intechopen.com/chapters/44528 [Accessed: 6 July 2023].

Hickman, S.E., Allison, E.K. and Khoury, J.E. 2008. Microglial Dysfunction and Defective β-Amyloid Clearance Pathways in Aging Alzheimer's Disease Mice. *Journal of Neuroscience* 28(33), pp. 8354–8360. doi: 10.1523/JNEUROSCI.0616-08.2008.

Hickman, S.E., Kingery, N.D., Ohsumi, T.K., Borowsky, M.L., Wang, L., Means, T.K. and El Khoury, J. 2013. The microglial sensome revealed by direct RNA sequencing. *Nature Neuroscience* 16(12), pp. 1896–1905. doi: 10.1038/nn.3554.

Hirth, F. 2010. Drosophila melanogaster in the Study of Human Neurodegeneration. *CNS & Neurological Disorders Drug Targets* 9(4), pp. 504–523. doi: 10.2174/187152710791556104.

Hof, P.R., Bouras, C., Perl, D.P., Sparks, D.L., Mehta, N. and Morrison, J.H. 1995. Age-related distribution of neuropathologic changes in the cerebral cortex of patients with Down's syndrome. Quantitative regional analysis and comparison with Alzheimer's disease. *Archives of Neurology* 52(4), pp. 379–391. doi: 10.1001/archneur.1995.00540280065020.

Hofbauer, H.F., Heier, C., Sen Saji, A.K. and Kühnlein, R.P. 2021. Lipidome remodeling in aging normal and genetically obese *Drosophila* males. *Insect Biochemistry and Molecular Biology* 133, p. 103498. doi: 10.1016/j.ibmb.2020.103498.

Holtzman, D.M., Herz, J. and Bu, G. 2012. Apolipoprotein E and Apolipoprotein E Receptors: Normal Biology and Roles in Alzheimer Disease. *Cold Spring Harbor Perspectives in Medicine* 2(3), p. a006312. doi: 10.1101/cshperspect.a006312.

Hong, S. et al. 2016. Complement and microglia mediate early synapse loss in Alzheimer mouse models. *Science (New York, N.Y.)* 352(6286), pp. 712–716. doi: 10.1126/science.aad8373.

Ioannou, M.S. et al. 2019. Neuron-Astrocyte Metabolic Coupling Protects against Activity-Induced Fatty Acid Toxicity. *Cell* 177(6), pp. 1522-1535.e14. doi: 10.1016/j.cell.2019.04.001.

Iyer, J. et al. 2016. Quantitative Assessment of Eye Phenotypes for Functional Genetic Studies Using Drosophila melanogaster. *G3 (Bethesda, Md.)* 6(5), pp. 1427–1437. doi: 10.1534/g3.116.027060.

Jack, C.R. et al. 2010. Hypothetical model of dynamic biomarkers of the Alzheimer's pathological cascade. *The Lancet Neurology* 9(1), pp. 119–128. doi: 10.1016/S1474-4422(09)70299-6.

Jack, C.R. and Holtzman, D.M. 2013. Biomarker Modeling of Alzheimer's Disease. *Neuron* 80(6), pp. 1347–1358. doi: 10.1016/j.neuron.2013.12.003.

Jackson, R.J., Meltzer, J.C., Nguyen, H., Commins, C., Bennett, R.E., Hudry, E. and Hyman, B.T. 2022. APOE4 derived from astrocytes leads to blood–brain barrier impairment. *Brain* 145(10), pp. 3582–3593. doi: 10.1093/brain/awab478.

Jeon, Y., Lee, J.H., Choi, B., Won, S.-Y. and Cho, K.S. 2020. Genetic Dissection of Alzheimer's Disease Using Drosophila Models. *International Journal of Molecular Sciences* 21(3). Available at: https://www.ncbi.nlm.nih.gov/pmc/articles/PMC7037931/ [Accessed: 5 February 2024].

Jones, L. et al. 2010. Genetic Evidence Implicates the Immune System and Cholesterol Metabolism in the Aetiology of Alzheimer's Disease. *PLOS ONE* 5(11), p. e13950. doi: 10.1371/journal.pone.0013950.

Kanekiyo, T., Xu, H. and Bu, G. 2014. ApoE and Aβ in Alzheimer's disease: accidental encounters or partners? *Neuron* 81(4), pp. 740–754. doi: 10.1016/j.neuron.2014.01.045.

Karch, C.M. and Goate, A.M. 2015. Alzheimer's disease risk genes and mechanisms of disease pathogenesis. *Biological psychiatry* 77(1), pp. 43–51. doi: 10.1016/j.biopsych.2014.05.006.

Karran, E., Mercken, M. and Strooper, B.D. 2011. The amyloid cascade hypothesis for Alzheimer's disease: an appraisal for the development of therapeutics. *Nature Reviews Drug Discovery* 10(9), pp. 698–712. doi: 10.1038/nrd3505.

Kawade, N. and Yamanaka, K. 2024. Novel insights into brain lipid metabolism in Alzheimer's disease: Oligodendrocytes and white matter abnormalities. *FEBS open bio* 14(2), pp. 194–216. doi: 10.1002/2211-5463.13661.

Kayed, R., Head, E., Thompson, J.L., McIntire, T.M., Milton, S.C., Cotman, C.W. and Glabe, C.G. 2003. Common structure of soluble amyloid oligomers implies common mechanism of pathogenesis. *Science (New York, N.Y.)* 300(5618), pp. 486–489. doi: 10.1126/science.1079469.

Keep, R.F., Zhou, N., Xiang, J., Andjelkovic, A.V., Hua, Y. and Xi, G. 2014. Vascular disruption and blood–brain barrier dysfunction in intracerebral hemorrhage. *Fluids and Barriers of the CNS* 11(1), p. 18. doi: 10.1186/2045-8118-11-18.

Kelley, B.J. and Petersen, R.C. 2007. Alzheimer's Disease and Mild Cognitive Impairment. *Neurologic clinics* 25(3), pp. 577–v. doi: 10.1016/j.ncl.2007.03.008.

Khachiyants, N., Trinkle, D., Son, S.J. and Kim, K.Y. 2011. Sundown Syndrome in Persons with Dementia: An Update. *Psychiatry Investigation* 8(4), pp. 275–287. doi: 10.4306/pi.2011.8.4.275.

Kim, T., Song, B. and Lee, I.-S. 2020. Drosophila Glia: Models for Human Neurodevelopmental and Neurodegenerative Disorders. *International Journal of Molecular Sciences* 21(14), p. 4859. doi: 10.3390/ijms21144859.

Koychev, I., Hofer, M. and Friedman, N. 2020. Correlation of Alzheimer Disease Neuropathologic Staging with Amyloid and Tau Scintigraphic Imaging Biomarkers. *Journal of Nuclear Medicine* 61(10), pp. 1413–1418. doi: 10.2967/jnumed.119.230458.

Kremer, M.C., Jung, C., Batelli, S., Rubin, G.M. and Gaul, U. 2017. The glia of the adult Drosophila nervous system. *Glia* 65(4), pp. 606–638. doi: 10.1002/glia.23115.

Kuhn, A.J., Abrams, B.S., Knowlton, S. and Raskatov, J.A. 2020. The Alzheimer's Disease "non-amyloidogenic" p3 peptide revisited: a case for Amyloid-α. *ACS chemical neuroscience* 11(11), pp. 1539–1544. doi: 10.1021/acschemneuro.0c00160.

Lai, S.-L. and Lee, T. 2006. Genetic mosaic with dual binary transcriptional systems in Drosophila. *Nature Neuroscience* 9(5), pp. 703–709. doi: 10.1038/nn1681.

Leduc, V., Jasmin-Bélanger, S. and Poirier, J. 2010. APOE and cholesterol homeostasis in Alzheimer’s disease. *Trends in Molecular Medicine* 16(10), pp. 469–477. doi: 10.1016/j.molmed.2010.07.008.

Lee, H. et al. 2023. ApoE4-dependent lysosomal cholesterol accumulation impairs mitochondrial homeostasis and oxidative phosphorylation in human astrocytes. *Cell Reports* 42(10), p. 113183. doi: 10.1016/j.celrep.2023.113183.

Lee, J.A., Hall, B., Allsop, J., Alqarni, R. and Allen, S.P. 2021. Lipid metabolism in astrocytic structure and function. *Seminars in Cell & Developmental Biology* 112, pp. 123–136. doi: 10.1016/j.semcdb.2020.07.017.

Leng, F. and Edison, P. 2021. Neuroinflammation and microglial activation in Alzheimer disease: where do we go from here? *Nature Reviews Neurology* 17(3), pp. 157–172. doi: 10.1038/s41582-020-00435-y.

Li, N., Liu, K., Qiu, Y., Ren, Z., Dai, R., Deng, Y. and Qing, H. 2016. Effect of Presenilin Mutations on APP Cleavage; Insights into the Pathogenesis of FAD. *Frontiers in Aging Neuroscience* 8, p. 51. doi: 10.3389/fnagi.2016.00051.

Li, X. et al. 2023. A fluorogenic complementation tool kit for interrogating lipid droplet-organelle interaction. *bioRxiv*, p. 2023.11.29.569289. doi: 10.1101/2023.11.29.569289.

Li, X.-L., Hu, N., Tan, M.-S., Yu, J.-T. and Tan, L. 2014. Behavioral and psychological symptoms in Alzheimer’s disease. *BioMed Research International* 2014, p. 927804. doi: 10.1155/2014/927804.

Li, Y. et al. 2024. Microglial lipid droplet accumulation in tauopathy brain is regulated by neuronal AMPK. *Cell Metabolism*. Available at: https://www.sciencedirect.com/science/article/pii/S1550413124001189 [Accessed: 6 May 2024].

Li, Y.X., Sibon, O.C.M. and Dijkers, P.F. 2018. Inhibition of NF-κB in astrocytes is sufficient to delay neurodegeneration induced by proteotoxicity in neurons. *Journal of Neuroinflammation* 15(1), p. 261. doi: 10.1186/s12974-018-1278-2.

Lian, Y. et al. 2023. Clarity on the blazing trail: clearing the way for amyloid-removing therapies for Alzheimer’s disease. *Molecular Psychiatry*, pp. 1–9. doi: 10.1038/s41380-023-02324-4.

Liao, F., Yoon, H. and Kim, J. 2017. Apolipoprotein E metabolism and functions in brain and its role in Alzheimer’s disease. *Current Opinion in Lipidology* 28(1), pp. 60–67. doi: 10.1097/MOL.0000000000000383.

Linnerbauer, M., Wheeler, M.A. and Quintana, F.J. 2020. Astrocyte Crosstalk in CNS Inflammation. *Neuron* 108(4), pp. 608–622. doi: 10.1016/j.neuron.2020.08.012.

Litvinchuk, A. et al. 2024. Amelioration of Tau and ApoE4-linked glial lipid accumulation and neurodegeneration with an LXR agonist. *Neuron* 112(3), pp. 384-403.e8. doi: 10.1016/j.neuron.2023.10.023.

Liu, L. et al. 2015. Glial lipid droplets and ROS induced by mitochondrial defects promote neurodegeneration. *Cell* 160(1–2), pp. 177–190. doi: 10.1016/j.cell.2014.12.019.

Liu, L., MacKenzie, K.R., Putluri, N., Maletić-Savatić, M. and Bellen, H.J. 2017. The Glia-Neuron Lactate Shuttle and Elevated ROS Promote Lipid Synthesis in Neurons and Lipid Droplet Accumulation in Glia via APOE/D. *Cell Metabolism* 26(5), pp. 719-737.e6. doi: 10.1016/j.cmet.2017.08.024.

Liu, Q. et al. 2010. Neuronal LRP1 Knockout in Adult Mice Leads to Impaired Brain Lipid Metabolism and Progressive, Age-Dependent Synapse Loss and Neurodegeneration. *The Journal of Neuroscience* 30(50), pp. 17068–17078. doi: 10.1523/JNEUROSCI.4067-10.2010.

López, O.L. and DeKosky, S.T. 2008. Clinical symptoms in Alzheimer's disease. In: *Handbook of Clinical Neurology*. Dementias. Elsevier, pp. 207–216. Available at: https://www.sciencedirect.com/science/article/pii/S0072975207012195 [Accessed: 4 February 2024].

Loring, H.S. and Thompson, P.R. 2020. Emergence of SARM1 as a Potential Therapeutic Target for Wallerian-type Diseases. *Cell Chemical Biology* 27(1), pp. 1–13. doi: 10.1016/j.chembiol.2019.11.002.

Lu, T.-Y., MacDonald, J.M., Neukomm, L.J., Sheehan, A.E., Bradshaw, R., Logan, M.A. and Freeman, M.R. 2017. Axon degeneration induces glial responses through Draper-TRAF4-JNK signalling. *Nature Communications* 8(1), p. 14355. doi: 10.1038/ncomms14355.

Luo, L., Tully, T. and White, K. 1992. Human amyloid precursor protein ameliorates behavioral deficit of flies deleted for Appl gene. *Neuron* 9(4), pp. 595–605. doi: 10.1016/0896-6273(92)90024-8.

Ma, Z., Stork, T., Bergles, D.E. and Freeman, M.R. 2016. Neuromodulators signal through astrocytes to alter neural circuit activity and behaviour. *Nature* 539(7629), pp. 428–432. doi: 10.1038/nature20145.

MacDonald, J.M., Beach, M.G., Porpiglia, E., Sheehan, A.E., Watts, R.J. and Freeman, M.R. 2006. The Drosophila Cell Corpse Engulfment Receptor Draper Mediates Glial Clearance of Severed Axons. *Neuron* 50(6), pp. 869–881. doi: 10.1016/j.neuron.2006.04.028.

Maitre, M., Jeltsch-David, H., Okechukwu, N.G., Klein, C., Patte-Mensah, C. and Mensah-Nyagan, A.-G. 2023. Myelin in Alzheimer's disease: culprit or bystander? *Acta Neuropathologica Communications* 11(1), p. 56. doi: 10.1186/s40478-023-01554-5.

Marschallinger, J. et al. 2020. Lipid-droplet-accumulating microglia represent a dysfunctional and proinflammatory state in the aging brain. *Nature Neuroscience* 23(2), pp. 194–208. doi: 10.1038/s41593-019-0566-1.

Marshall, L.L., Stimpson, S.E., Hyland, R., Coorssen, J.R. and Myers, S.J. 2014. Increased lipid droplet accumulation associated with a peripheral sensory neuropathy. *Journal of Chemical Biology* 7(2), pp. 67–76. doi: 10.1007/s12154-014-0108-y.

Meyers, A., Chourey, K., Weiskittel, T.M., Pfiffner, S., Dunlap, J.R., Hettich, R.L. and Dalhaimer, P. 2017. The protein and neutral lipid composition of lipid droplets isolated from the fission yeast, Schizosaccharomyces pombe. *Journal of Microbiology (Seoul, Korea)* 55(2), pp. 112–122. doi: 10.1007/s12275-017-6205-1.

Miranda, A., Montiel, E., Ulrich, H. and Paz, C. 2021. Selective Secretase Targeting for Alzheimer's Disease Therapy. *Journal of Alzheimer's disease: JAD* 81(1), pp. 1–17. doi: 10.3233/JAD-201027.

Moulton, M.J. et al. 2021. Neuronal ROS-induced glial lipid droplet formation is altered by loss of Alzheimer's disease–associated genes. *Proceedings of the National Academy of Sciences* 118(52), p. e2112095118. doi: 10.1073/pnas.2112095118.

Müller, U.C. and Zheng, H. 2012. Physiological Functions of APP Family Proteins. *Cold Spring Harbor Perspectives in Medicine* 2(2), p. a006288. doi: 10.1101/cshperspect.a006288.

Muralidar, S., Ambi, S.V., Sekaran, S., Thirumalai, D. and Palaniappan, B. 2020. Role of tau protein in Alzheimer's disease: The prime pathological player. *International Journal of Biological Macromolecules* 163, pp. 1599–1617. doi: 10.1016/j.ijbiomac.2020.07.327.

Murray, M.A., Schubiger, M. and Palka, J. 1984. Neuron differentiation and axon growth in the developing wing of *Drosophila melanogaster*. *Developmental Biology* 104(2), pp. 259–273. doi: 10.1016/0012-1606(84)90082-4.

Myers, E.W. et al. 2000. A whole-genome assembly of Drosophila. *Science (New York, N.Y.)* 287(5461), pp. 2196–2204. doi: 10.1126/science.287.5461.2196.

Nugent, A.A. et al. 2020. TREM2 Regulates Microglial Cholesterol Metabolism upon Chronic Phagocytic Challenge. *Neuron* 105(5), pp. 837-854.e9. doi: 10.1016/j.neuron.2019.12.007.

Oliveira, J.M., Henriques, A.G., Martins, F., Rebelo, S. and da Cruz e Silva, O.A.B. 2015. Amyloid-β Modulates Both AβPP and Tau Phosphorylation. *Journal of Alzheimer's disease: JAD* 45(2), pp. 495–507. doi: 10.3233/JAD-142664.

Onal, G., Kutlu, O., Gozuacik, D. and Dokmeci Emre, S. 2017. Lipid Droplets in Health and Disease. *Lipids in Health and Disease* 16(1), p. 128. doi: 10.1186/s12944-017-0521-7.

Paglione, M., Rosell, A.L., Chatton, J.-Y. and Neukomm, L.J. 2020. Morphological and Functional Evaluation of Axons and their Synapses during Axon Death in Drosophila melanogaster. *JoVE (Journal of Visualized Experiments)* (157), p. e60865. doi: 10.3791/60865.

Panza, F., Lozupone, M., Logroscino, G. and Imbimbo, B.P. 2019. A critical appraisal of amyloid-β-targeting therapies for Alzheimer disease. *Nature Reviews Neurology* 15(2), pp. 73–88. doi: 10.1038/s41582-018-0116-6.

Parbo, P. et al. 2018. Does inflammation precede tau aggregation in early Alzheimer's disease? A PET study. *Neurobiology of Disease* 117, pp. 211–216. doi: 10.1016/j.nbd.2018.06.004.

Pini, L. et al. 2016. Brain atrophy in Alzheimer's Disease and aging. *Ageing Research Reviews* 30, pp. 25–48. doi: 10.1016/j.arr.2016.01.002.

Pol, A., Gross, S.P. and Parton, R.G. 2014. Biogenesis of the multifunctional lipid droplet: Lipids, proteins, and sites. *Journal of Cell Biology* 204(5), pp. 635–646. doi: 10.1083/jcb.201311051.

Potter, C.J., Tasic, B., Russler, E.V., Liang, L. and Luo, L. 2010. The Q System: A Repressible Binary System for Transgene Expression, Lineage Tracing, and Mosaic Analysis. *Cell* 141(3), pp. 536–548. doi: 10.1016/j.cell.2010.02.025.

Potter, H., Granic, A. and Caneus, J. 2016. Role of Trisomy 21 Mosaicism in Sporadic and Familial Alzheimer's Disease. *Current Alzheimer Research* 13(1), pp. 7–17. doi: 10.2174/156720501301151207100616.

Preat, T. and Goguel, V. 2016. Role of Drosophila Amyloid Precursor Protein in Memory Formation. *Frontiers in Molecular Neuroscience* 9. Available at: https://www.frontiersin.org/articles/10.3389/fnmol.2016.00142 [Accessed: 6 February 2024].

Prince, M, Knapp, M, Guerchet, M, McCrone, P, Prina, M, and Comas-Herrera, A. 2014. *Dementia UK: Update*. Alzheimer's Society. Available at: https://kclpure.kcl.ac.uk/ws/portalfiles/portal/35828472/P326_AS_Dementia_Report_WEB2.pdf [Accessed: 21 June 2023].

Prior, R. et al. 2023. Defective Schwann cell lipid metabolism alters plasma membrane dynamics in Charcot-Marie-Tooth disease 1A. p. 2023.04.02.535224. Available at: https://www.biorxiv.org/content/10.1101/2023.04.02.535224v1 [Accessed: 10 June 2024].

Prüßing, K., Voigt, A. and Schulz, J.B. 2013a. Drosophila melanogaster as a model organism for Alzheimer's disease. *Molecular Neurodegeneration* 8, p. 35. doi: 10.1186/1750-1326-8-35.

Prüßing, K., Voigt, A. and Schulz, J.B. 2013b. Drosophila melanogaster as a model organism for Alzheimer's disease. *Molecular Neurodegeneration* 8, p. 35. doi: 10.1186/1750-1326-8-35.

Purice, M.D., Ray, A., Münzel, E.J., Pope, B.J., Park, D.J., Speese, S.D. and Logan, M.A. 2017. A novel Drosophila injury model reveals severed axons are cleared through a Draper/MMP-1 signaling cascade. Stevens, B. ed. *eLife* 6, p. e23611. doi: 10.7554/eLife.23611.

Purice, M.D., Speese, S.D. and Logan, M.A. 2016. Delayed glial clearance of degenerating axons in aged Drosophila is due to reduced PI3K/Draper activity. *Nature Communications* 7(1), p. 12871. doi: 10.1038/ncomms12871.

Qi, G., Mi, Y., Shi, X., Gu, H., Brinton, R.D. and Yin, F. 2021. ApoE4 Impairs Neuron-Astrocyte Coupling of Fatty Acid Metabolism. *Cell Reports* 34(1), p. 108572. doi: 10.1016/j.celrep.2020.108572.

Qiao, H.-H. et al. 2018. An efficient and multiple target transgenic RNAi technique with low toxicity in Drosophila. *Nature Communications* 9(1), p. 4160. doi: 10.1038/s41467-018-06537-y.

Ralhan, I. et al. 2023. Autolysosomal exocytosis of lipids protect neurons from ferroptosis. *Journal of Cell Biology* 222(6), p. e202207130. doi: 10.1083/jcb.202207130.

Ramanan, V.K. and Day, G.S. 2023. Anti-amyloid therapies for Alzheimer disease: finally, good news for patients. *Molecular Neurodegeneration* 18(1), p. 42. doi: 10.1186/s13024-023-00637-0.

Rasband, M.N. 2016. Glial Contributions to Neural Function and Disease. *Molecular & Cellular Proteomics : MCP* 15(2), pp. 355–361. doi: 10.1074/mcp.R115.053744.

Raulin, A.-C., Doss, S.V., Trottier, Z.A., Ikezu, T.C., Bu, G. and Liu, C.-C. 2022. ApoE in Alzheimer's disease: pathophysiology and therapeutic strategies. *Molecular Neurodegeneration* 17(1), p. 72. doi: 10.1186/s13024-022-00574-4.

Ray, A., Speese, S.D. and Logan, M.A. 2017. Glial Draper Rescues Aβ Toxicity in a Drosophila Model of Alzheimer's Disease. *The Journal of Neuroscience* 37(49), pp. 11881–11893. doi: 10.1523/JNEUROSCI.0862-17.2017.

Riabinina, O. and Potter, C.J. 2016. The Q-System: A Versatile Expression System for Drosophila. In: Dahmann, C. ed. *Drosophila: Methods and Protocols*. Methods in Molecular Biology. New York, NY: Springer, pp. 53–78. Available at: https://doi.org/10.1007/978-1-4939-6371-3_3 [Accessed: 6 February 2024].

Rodríguez, A. del V., Didiano, D. and Desplan, C. 2011. Power tools for gene expression and clonal analysis in Drosophila. *Nature methods* 9(1), pp. 47–55. doi: 10.1038/nmeth.1800.

Rodríguez-Gómez, J.A. et al. 2020. Microglia: Agents of the CNS Pro-Inflammatory Response. *Cells* 9(7), p. 1717. doi: 10.3390/cells9071717.

Roses, A.D. 1996. Apolipoprotein E alleles as risk factors in Alzheimer's disease. *Annual Review of Medicine* 47, pp. 387–400. doi: 10.1146/annurev.med.47.1.387.

Rotshenker, S. 2011. Wallerian degeneration: the innate-immune response to traumatic nerve injury. *Journal of Neuroinflammation* 8(1), p. 109. doi: 10.1186/1742-2094-8-109.

Sarasa, M. and Pesini, P. 2009. Natural Non-Trasgenic Animal Models for Research in Alzheimer's Disease. *Current Alzheimer Research* 6(2), pp. 171–178. doi: 10.2174/156720509787602834.

Sasaki, Y., Nakagawa, T., Mao, X., DiAntonio, A. and Milbrandt, J. 2016. NMNAT1 inhibits axon degeneration via blockade of SARM1-mediated NAD+ depletion. Chao, M. V. ed. *eLife* 5, p. e19749. doi: 10.7554/eLife.19749.

Scheuner, D. et al. 1996. Secreted amyloid β–protein similar to that in the senile plaques of Alzheimer's disease is increased in vivo by the presenilin 1 and 2 and APP mutations linked to familial Alzheimer's disease. *Nature Medicine* 2(8), pp. 864–870. doi: 10.1038/nm0896-864.

Schindelin, J. et al. 2012. Fiji: an open-source platform for biological-image analysis. *Nature Methods* 9(7), pp. 676–682. doi: 10.1038/nmeth.2019.

Schott, M.B., Weller, S.G., Schulze, R.J., Krueger, E.W., Drizyte-Miller, K., Casey, C.A. and McNiven, M.A. 2019. Lipid droplet size directs lipolysis and lipophagy catabolism in hepatocytes. *Journal of Cell Biology* 218(10), pp. 3320–3335. doi: 10.1083/jcb.201803153.

Schultz, H., Sommer, T. and Peters, J. 2015. The Role of the Human Entorhinal Cortex in a Representational Account of Memory. *Frontiers in Human Neuroscience* 9, p. 628. doi: 10.3389/fnhum.2015.00628.

Serrano-Pozo, A., Mielke, M.L., Gómez-Isla, T., Betensky, R.A., Growdon, J.H., Frosch, M.P. and Hyman, B.T. 2011. Reactive Glia not only Associates with Plaques but also Parallels Tangles in Alzheimer's Disease. *The American Journal of Pathology* 179(3), pp. 1373–1384. doi: 10.1016/j.ajpath.2011.05.047.

Sharma, N.S., Karan, A., Lee, D., Yan, Z. and Xie, J. 2021. Advances in Modeling Alzheimer's Disease In Vitro. *Advanced NanoBiomed Research* 1(12), p. 2100097. doi: 10.1002/anbr.202100097.

Sheneman, L., Stephanopoulos, G. and Vasdekis, A.E. 2021. Deep learning classification of lipid droplets in quantitative phase images. *PLoS ONE* 16(4), p. e0249196. doi: 10.1371/journal.pone.0249196.

Sheng, L. et al. 2023. Ensheathing glia promote increased lifespan and healthy brain aging. *Aging Cell* 22(5), p. e13803. doi: 10.1111/acel.13803.

Shinohara, M., Tachibana, M., Kanekiyo, T. and Bu, G. 2017. Role of LRP1 in the pathogenesis of Alzheimer’s disease: evidence from clinical and preclinical studies: Thematic Review Series: ApoE and Lipid Homeostasis in Alzheimer’s Disease. *Journal of Lipid Research* 58(7), pp. 1267–1281. doi: 10.1194/jlr.R075796.

Sims, J.R. et al. 2023. Donanemab in Early Symptomatic Alzheimer Disease: The TRAILBLAZER-ALZ 2 Randomized Clinical Trial. *JAMA* 330(6), pp. 512–527. doi: 10.1001/jama.2023.13239.

Small, S.A. and Petsko, G.A. 2015. Retromer in Alzheimer disease, Parkinson disease and other neurological disorders. *Nature Reviews Neuroscience* 16(3), pp. 126–132. doi: 10.1038/nrn3896.

Sperling, R.A. et al. 2011. Toward defining the preclinical stages of Alzheimer’s disease: Recommendations from the National Institute on Aging-Alzheimer’s Association workgroups on diagnostic guidelines for Alzheimer’s disease. *Alzheimer’s & dementia : the journal of the Alzheimer’s Association* 7(3), pp. 280–292. doi: 10.1016/j.jalz.2011.03.003.

Stelzmann, R.A., Norman Schnitzlein, H. and Reed Murtagh, F. 1995. An english translation of alzheimer’s 1907 paper, “über eine eigenartige erkankung der hirnrinde”. *Clinical Anatomy* 8(6), pp. 429–431. doi: 10.1002/ca.980080612.

Strittmatter, W.J. and Roses, A.D. 1996. Apolipoprotein E and Alzheimer’s disease. *Annual Review of Neuroscience* 19, pp. 53–77. doi: 10.1146/annurev.ne.19.030196.000413.

Swaddiwudhipong, N., Whiteside, D.J., Hezemans, F.H., Street, D., Rowe, J.B. and Rittman, T. 2023. Pre-diagnostic cognitive and functional impairment in multiple sporadic neurodegenerative diseases. *Alzheimer’s & Dementia* 19(5), pp. 1752–1763. doi: 10.1002/alz.12802.

Takata, F., Nakagawa, S., Matsumoto, J. and Dohgu, S. 2021. Blood-Brain Barrier Dysfunction Amplifies the Development of Neuroinflammation: Understanding of Cellular Events in Brain Microvascular Endothelial Cells for Prevention and Treatment of BBB Dysfunction. *Frontiers in Cellular Neuroscience* 15. Available at: https://www.frontiersin.org/articles/10.3389/fncel.2021.661838 [Accessed: 17 May 2024].

Tang, F., Lane, S., Korsak, A., Paton, J.F.R., Gourine, A.V., Kasparov, S. and Teschemacher, A.G. 2014. Lactate-mediated glia-neuronal signalling in the mammalian brain. *Nature Communications* 5, p. 3284. doi: 10.1038/ncomms4284.

TCW, J. and Goate, A.M. 2017. Genetics of β-Amyloid Precursor Protein in Alzheimer’s Disease. *Cold Spring Harbor Perspectives in Medicine* 7(6), p. a024539. doi: 10.1101/cshperspect.a024539.

Terry, R.D. et al. 1991. Physical basis of cognitive alterations in Alzheimer’s disease: synapse loss is the major correlate of cognitive impairment. *Annals of Neurology* 30(4), pp. 572–580. doi: 10.1002/ana.410300410.

Thuma, L., Carter, D., Weavers, H. and Martin, P. 2018. Drosophila immune cells extravasate from vessels to wounds using Tre1 GPCR and Rho signaling. *Journal of Cell Biology* 217(9), pp. 3045–3056. doi: 10.1083/jcb.201801013.

Uffelmann, E. et al. 2021. Genome-wide association studies. *Nature Reviews Methods Primers* 1(1), pp. 1–21. doi: 10.1038/s43586-021-00056-9.

Vagnoni, A. and Bullock, S.L. 2016. A simple method for imaging axonal transport in aging neurons using the adult Drosophila wing. *Nature Protocols* 11(9), pp. 1711–1723. doi: 10.1038/nprot.2016.112.

Vercruysse, P., Vieau, D., Blum, D., Petersén, Å. and Dupuis, L. 2018. Hypothalamic Alterations in Neurodegenerative Diseases and Their Relation to Abnormal Energy Metabolism. *Frontiers in Molecular Neuroscience* 11, p. 2. doi: 10.3389/fnmol.2018.00002.

Verma, M., Vats, A. and Taneja, V. 2015. Toxic species in amyloid disorders: Oligomers or mature fibrils. *Annals of Indian Academy of Neurology* 18(2), pp. 138–145. doi: 10.4103/0972-2327.144284.

Victor, M.B. et al. 2022. Lipid accumulation induced by APOE4 impairs microglial surveillance of neuronal-network activity. *Cell Stem Cell* 29(8), pp. 1197-1212.e8. doi: 10.1016/j.stem.2022.07.005.

Wagner, B., Natarajan, A., Grünaug, S., Kroismayr, R., Wagner, E.F. and Sibilia, M. 2006. Neuronal survival depends on EGFR signaling in cortical but not midbrain astrocytes. *The EMBO journal* 25(4), pp. 752–762. doi: 10.1038/sj.emboj.7600988.

Wahrle, S.E., Jiang, H., Parsadanian, M., Hartman, R.E., Bales, K.R., Paul, S.M. and Holtzman, D.M. 2005. Deletion of Abca1 Increases Aβ Deposition in the PDAPP Transgenic Mouse Model of Alzheimer Disease *. *Journal of Biological Chemistry* 280(52), pp. 43236–43242. doi: 10.1074/jbc.M508780200.

Wang, J.T., Medress, Z.A. and Barres, B.A. 2012. Axon degeneration: Molecular mechanisms of a self-destruction pathway. *The Journal of Cell Biology* 196(1), pp. 7–18. doi: 10.1083/jcb.201108111.

Welte, M.A. 2015. As the fat flies: the dynamic lipid droplets of Drosophila embryos. *Biochimica et biophysica acta* 1851(9), pp. 1156–1185. doi: 10.1016/j.bbalip.2015.04.002.

Wimo, A. et al. 2023. The worldwide costs of dementia in 2019. *Alzheimer's & Dementia: The Journal of the Alzheimer's Association* 19(7), pp. 2865–2873. doi: 10.1002/alz.12901.

Windham, I.A., Ragusa, J.V., Wallace, E.D., Wagner, C.H., White, K.K. and Cohen, S. 2023. APOE traffics to astrocyte lipid droplets and modulates triglyceride saturation and droplet size. *bioRxiv: The Preprint Server for Biology*, p. 2023.04.28.538740. doi: 10.1101/2023.04.28.538740.

Wu, Z., Sun, J., Liao, Z., Qiao, J., Chen, C., Ling, C. and Wang, H. 2022. An update on the therapeutic implications of long-chain acyl-coenzyme A synthetases in nervous system diseases. *Frontiers in Neuroscience* 16, p. 1030512. doi: 10.3389/fnins.2022.1030512.

Xu, H.E., Kodadek, T. and Johnston, S.A. 1995. A single GAL4 dimer can maximally activate transcription under physiological conditions. *Proceedings of the National Academy of Sciences of the United States of America* 92(17), pp. 7677–7680.

Yan, R. et al. 1999. Membrane-anchored aspartyl protease with Alzheimer's disease β-secretase activity. *Nature* 402(6761), pp. 533–537. doi: 10.1038/990107.

Yang, H., Galea, A., Sytnyk, V. and Crossley, M. 2012. Controlling the size of lipid droplets: lipid and protein factors. *Current Opinion in Cell Biology* 24(4), pp. 509–516. doi: 10.1016/j.ceb.2012.05.012.

Yildirim, K., Petri, J., Kottmeier, R. and Klämbt, C. 2019. Drosophila glia: Few cell types and many conserved functions. *Glia* 67(1), pp. 5–26. doi: 10.1002/glia.23459.

Yu, Y.V., Li, Z., Rizzo, N.P., Einstein, J. and Welte, M.A. 2011. Targeting the motor regulator Klar to lipid droplets. *BMC Cell Biology* 12, p. 9. doi: 10.1186/1471-2121-12-9.

Zhang, Y., Chen, H., Li, R., Sterling, K. and Song, W. 2023. Amyloid β-based therapy for Alzheimer's disease: challenges, successes and future. *Signal Transduction and Targeted Therapy* 8(1), pp. 1–26. doi: 10.1038/s41392-023-01484-7.

Zhang, Y., Wu, K.-M., Yang, L., Dong, Q. and Yu, J.-T. 2022. Tauopathies: new perspectives and challenges. *Molecular Neurodegeneration* 17(1), p. 28. doi: 10.1186/s13024-022-00533-z.

Zhao, J., Liu, X., Xia, W., Zhang, Y. and Wang, C. 2020. Targeting Amyloidogenic Processing of APP in Alzheimer's Disease. *Frontiers in Molecular Neuroscience* 13. Available at: https://www.frontiersin.org/articles/10.3389/fnmol.2020.00137 [Accessed: 18 May 2024].

Appendix

Appendix I. Table of materials

Item	Manufacturer	Identifier	Batch
100 bp DNA ladder	Invitrogen	15628019	01339502
16% Paraformaldehyde solution	Thermo Scientific	28908	XB340632
Agarose	Fisher Bioreagents	BP1356-500	215866
Ceramic Coated Forceps	Fine Science Tools	11252-50	5HDC
Disposable scalpel	Swann-Morton	0503	7662307
Glass Cover Slips 22x40mm	Academy	400-08-18	N/A
Goat anti-Mouse IgG Secondary Antibody, Alexa Fluor™ 647	Invitrogen	A21235	1915807
GoTaq® Green Master Mix	Promega	M712	0000572247
Halocarbon oil 27	Sigma Aldrich	H8773-100ML	MKCK9161
Normal Goat Serum	Vector Laboratories	S-1000	ZJ1010
PBS pH 7.4 10X	Gibco	70011-044	2323018
Phusion® High-Fidelity DNA Polymerase	New England Biolabs	M0530L	10058481
Proteinase K	Ambion	AM2546	1907003
PureLink Quick Gel Extraction and PCR Purification Combo Kit	Invitrogen	K220001	00808514
Purified anti-β-Amyloid, 1-16 Antibody, mouse	Biolegend	8030001	B319159 Clone 6E10
PYREX® 9 Depression Glass Spot Plates	Corning	7220-85	N/A
Safeview	NBS Biologicals	NBS-SV	P1024
Superfrost TM Microscope Slides	Epredia	AA00008332E01MNZ10	120221507
TAE 50x	Fisher Bioreagents	BP1332-1	216217
Triton X-100	MP Biomedicals	807426	Q5237
Vannas Spring Scissors - 2mm Cutting Edge	Fine Science Tools	15000-04	05K
VECTASHIELD Antifade Mounting Medium	Vector Laboratories	H-1000	ZJ0927

Appendix II. Table of statistical analyses and comparisons

	P value	Summary	F number (DFn, DFd)
Figure 3.2A			
RM one-way ANOVA:			
Timepoint	0.0017	***	F (1.103, 7.723) = 21.12
Comparisons:			
15 vs. 30	0.0520	ns	
15 vs. 45	0.0141	*	
15 vs. 60	0.0118	*	
15 vs. 90	0.0098	**	
15 vs. 120	0.0095	**	
Figure 3.2B			
RM one-way ANOVA:			
Timepoint	<0.0001	****	F (2.282, 15.97) = 99.44
Comparisons:			
15 vs. 30	0.0172	*	
15 vs. 45	0.0001	***	
15 vs. 60	<0.0001	****	
15 vs. 90	<0.0001	****	
15 vs. 120	<0.0001	****	
Figure 3.2D			
RM one-way ANOVA:			
Timepoint	0.2948	ns	F (5, 35) = 1.279
Comparisons:			
15 vs. 30	0.9984	ns	
15 vs. 45	0.9811	ns	
15 vs. 60	0.8608	ns	
15 vs. 90	0.9917	ns	
15 vs. 120	0.1153	ns	
Figure 3.2E			
RM one-way ANOVA:			
Timepoint	0.0004	***	F (5, 35) = 6.135
Comparisons:			
15 vs. 30	0.9828	ns	
15 vs. 45	0.9996	ns	
15 vs. 60	0.4046	ns	
15 vs. 90	0.1654	ns	
15 vs. 120	0.0007	***	

	P value	Summary	F number (DFn, DFd)
Ordinary one-way ANOVA:			
Timepoint	0.0024	**	F (2, 27) = 7.633
Comparisons:			
24H PI vs. 48H PI	0.0043	**	
24H PI vs. 72H PI	0.9585	ns	
48H PI vs. 72H PI	0.0087	**	
Ordinary one-way ANOVA:			
Timepoint	0.0177	*	F (2, 27) = 4.703
Comparisons:			
24H PI vs. 48H PI	0.0331	*	
24H PI vs. 72H PI	0.9997	ns	
48H PI vs. 72H PI	0.0348	*	
Ordinary one-way ANOVA:			
Timepoint	0.7796	ns	F (2, 27) = 0.2512
Comparisons:			
24H PI vs. 48H PI	0.8154	ns	
24H PI vs. 72H PI	>0.9999	ns	
48H PI vs. 72H PI	0.8123	ns	

	P value	**Summary**	**F number (DFn, DFd)**
Figure 3.4A			
RM two-way ANOVA:			
Interaction	0.6516	ns	F (1, 38) = 0.2071
Genotype	0.0302	*	F (1, 38) = 5.070
Injury	<0.0001	****	F (1, 38) = 193.9
Comparisons:			
♂ LacZ Uninjured vs. Injured	<0.0001	****	
♂ Aβ42 Uninjured vs. Injured	<0.0001	****	
Uninjured ♂ LacZ vs. ♂ Aβ42	0.1765	ns	
Injured ♂ LacZ vs. ♂ Aβ42	0.0519	ns	
Figure 3.4B			
RM two-way ANOVA:			
Interaction	0.0011	**	F (1, 38) = 12.41
Genotype	<0.0001	****	F (1, 38) = 27.86
Injury	<0.0001	****	F (1, 38) = 374.0
Comparisons:			
♂ LacZ Uninjured vs. Injured	<0.0001	****	
♂ Aβ42 Uninjured vs. Injured	<0.0001	****	
Uninjured ♂ LacZ vs. ♂ Aβ42	0.0806	ns	
Injured ♂ LacZ vs. ♂ Aβ42	<0.0001	****	
Figure 3.4C			
RM two-way ANOVA:			
Interaction	0.1741	ns	F (1, 38) = 1.918
Genotype	0.0007	***	F (1, 38) = 13.73
Injury	<0.0001	****	F (1, 38) = 46.62
Comparisons:			
♂ LacZ Uninjured vs. Injured	0.0004	***	
♂ Aβ42 Uninjured vs. Injured	<0.0001	****	
Uninjured ♂ LacZ vs. ♂ Aβ42	0.0304	*	
Injured ♂ LacZ vs. ♂ Aβ42	0.0003	****	

	P value	Summary	F number (DFn, DFd)
Figure 3.6A			
Two-way ANOVA:			
Interaction	0.0003	***	F (2, 172) = 8.568
Injury	<0.0001	****	F (1, 172) = 149.0
Genotype	<0.0001	****	F (2, 172) = 14.07
Comparisons:			
Uninjured:repo>attp40-PJFRC vs. Uninjured:repo>draper	0.9835	ns	
Uninjured:repo>attp40-PJFRC vs. Uninjured:repo>draper RNAi	>0.9999	ns	
Uninjured:repo>attp40-PJFRC vs. Injured:repo>attp40PJFRC	<0.0001	****	
Uninjured:repo>draper vs. Injured:repo>draper	<0.0001	****	
Uninjured:repo>draper RNAi vs. Injured:repo>draper RNAi	<0.0001	****	
Injured:repo>attp40-PJFRC vs. Injured:repo>draper	<0.0001	****	
Injured:repo>attp40-PJFRC vs. Injured:repo>draper RNAi	0.8844	ns	
Figure 3.6B			
Two-way ANOVA:			
Interaction	<0.0001	****	F (2, 172) = 18.13
Injury	<0.0001	****	F (1, 172) = 192.6
Genotype	<0.0001	****	F (2, 172) = 57.60
Comparisons:			
Uninjured:repo>attp40-PJFRC vs. Uninjured:repo>draper	0.0100	*	
Uninjured:repo>attp40-PJFRC vs. Uninjured:repo>draper RNAi	0.9602	ns	
Uninjured:repo>attp40-PJFRC vs. Injured:repo>attp40-PJFRC	<0.0001	****	
Uninjured:repo>draper vs. Injured:repo>draper	<0.0001	****	
Uninjured:repo>draper RNAi vs. Injured:repo>draper RNAi	0.0002	***	
Injured:repo>attp40-PJFRC vs. Injured:repo>draper	<0.0001	****	
Injured:repo>attp40-PJFRC vs. Injured:repo>draper RNAi	0.8013	ns	
Figure 3.6C			
Two-way ANOVA:			
Interaction	0.0114	*	F (2, 172) = 4.589
Injury	0.0002	***	F (1, 172) = 14.54
Genotype	<0.0001	****	F (2, 172) = 51.70
Comparisons:			
Uninjured:repo>attp40-PJFRC vs. Uninjured:repo>draper	<0.0001	****	
Uninjured:repo>attp40-PJFRC vs. Uninjured:repo>draper RNAi	0.0506	ns	
Uninjured:repo>attp40-PJFRC vs. Injured:repo>attp40-PJFRC	<0.0001	****	
Uninjured:repo>draper vs. Injured:repo>draper	0.9514	ns	
Uninjured:repo>draper RNAi vs. Injured:repo>draper RNAi	0.8980	ns	
Injured:repo>attp40-PJFRC vs. Injured:repo>draper	<0.0001	****	
Injured:repo>attp40-PJFRC vs. Injured:repo>draper RNAi	0.9807	ns	

	P value	**Summary**	**F number (DFn, DFd)**
Figure 3.7A			
Ordinary one-way ANOVA:			
Genotype	<0.0001	****	F (3, 116) = 39.83
Comparisons:			
w^-; LD/+; LacZ/Repo vs. w^-; LD/+; attp2-PJFRC/Repo	0.5730	ns	
w^-; LD/+; LacZ/Repo vs. w^-; LD/+; +/Repo	<0.0001	****	
w^-; LD/+; LacZ/Repo vs. w^-; LD/nSyb; LacZ/Repo	<0.0001	****	
w^-; LD/+; attp2-PJFRC/Repo vs. w^-; LD/+; +/Repo	<0.0001	****	
w^-; LD/+; attp2-PJFRC/Repo vs. w^-; LD/nSyb; LacZ/Repo	<0.0001	****	
w^-; LD/+; +/Repo vs. w^-; LD/nSyb; LacZ/Repo	0.4377	ns	
Figure 3.7B			
Ordinary one-way ANOVA:			
Genotype	<0.0001	****	F (3, 116) = 31.08
Comparisons:			
w^-; LD/+; LacZ/Repo vs. w^-; LD/+; attp2-PJFRC/Repo	0.9984	ns	
w^-; LD/+; LacZ/Repo vs. w^-; LD/+; +/Repo	<0.0001	****	
w^-; LD/+; LacZ/Repo vs. w^-; LD/nSyb; LacZ/Repo	<0.0001	****	
w^-; LD/+; attp2-PJFRC/Repo vs. w^-; LD/+; +/Repo	<0.0001	****	
w^-; LD/+; attp2-PJFRC/Repo vs. w^-; LD/nSyb; LacZ/Repo	<0.0001	****	
w^-; LD/+; +/Repo vs. w^-; LD/nSyb; LacZ/Repo	0.9914	ns	
Figure 3.7C			
Ordinary one-way ANOVA:			
Genotype	<0.0001	****	F (3, 117) = 18.28
Comparisons:			
w^-; LD/+; LacZ/Repo vs. w^-; LD/+; attp2-PJFRC/Repo	0.0211	*	
w^-; LD/+; LacZ/Repo vs. w^-; LD/+; +/Repo	0.4850	ns	
w^-; LD/+; LacZ/Repo vs. w^-; LD/nSyb; LacZ/Repo	<0.0001	****	
w^-; LD/+; attp2-PJFRC/Repo vs. w^-; LD/+; +/Repo	0.0005	***	
w^-; LD/+; attp2-PJFRC/Repo vs. w^-; LD/nSyb; LacZ/Repo	0.0592	ns	
w^-; LD/+; +/Repo vs. w^-; LD/nSyb; LacZ/Repo	<0.0001	****	

	P value	Summary	F number (DFn, DFd)
Figure 3.8A			
Two-way ANOVA:			
Interaction	<0.0001	****	F (5, 348) = 6.671
Genotype	<0.0001	****	F (1, 348) = 152.4
Timepoint	<0.0001	****	F (5, 348) = 10.42
Comparisons:			
LacZ:7DPE vs. LacZ:14DPE	>0.9999	ns	
LacZ:7DPE vs. LacZ:21DPE	>0.9999	ns	
LacZ:7DPE vs. LacZ:28DPE	>0.9999	ns	
LacZ:7DPE vs. LacZ:35DPE	>0.9999	ns	
LacZ:7DPE vs. LacZ:50DPE	>0.9999	ns	
LacZ:7DPE vs. Aβ42:7DPE	<0.0001	****	
LacZ:14DPE vs. Aβ42:14DPE	<0.0001	****	
LacZ:21DPE vs. Aβ42:21DPE	<0.0001	****	
LacZ:28DPE vs. Aβ42:28DPE	0.0816	ns	
LacZ:35DPE vs. Aβ42:35DPE	0.2348	ns	
LacZ:50DPE vs. Aβ42:50DPE	0.4149	ns	
Aβ42:7DPE vs. Aβ42:14DPE	0.5668	ns	
Aβ42:7DPE vs. Aβ42:21DPE	0.0006	***	
Aβ42:7DPE vs. Aβ42:28DPE	>0.9999	ns	
Aβ42:7DPE vs. Aβ42:35DPE	0.9194	ns	
Aβ42:7DPE vs. Aβ42:50DPE	0.2685	ns	
Figure 3.8B			
Two-way ANOVA:			
Interaction	<0.0001	****	F (5, 348) = 5.324
Genotype	<0.0001	****	F (1, 348) = 140.7
Timepoint	<0.0001	****	F (5, 348) = 12.34
Comparisons:			
LacZ:7DPE vs. LacZ:14DPE	>0.9999	ns	
LacZ:7DPE vs. LacZ:21DPE	0.5031	ns	
LacZ:7DPE vs. LacZ:28DPE	0.9749	ns	
LacZ:7DPE vs. LacZ:35DPE	0.9887	ns	
LacZ:7DPE vs. LacZ:50DPE	0.998	ns	
LacZ:7DPE vs. Aβ42:7DPE	0.2241	ns	
LacZ:14DPE vs. Aβ42:14DPE	<0.0001	****	
LacZ:21DPE vs. Aβ42:21DPE	<0.0001	****	
LacZ:28DPE vs. Aβ42:28DPE	<0.0001	****	
LacZ:35DPE vs. Aβ42:35DPE	0.1418	ns	
LacZ:50DPE vs. Aβ42:50DPE	0.0301	*	
Aβ42:7DPE vs. Aβ42:14DPE	0.0073	**	
Aβ42:7DPE vs. Aβ42:21DPE	<0.0001	****	
Aβ42:7DPE vs. Aβ42:28DPE	0.016	*	
Aβ42:7DPE vs. Aβ42:35DPE	0.9636	ns	
Aβ42:7DPE vs. Aβ42:50DPE	0.8584	ns	
Figure 3.8C			
Two-way ANOVA:			
Interaction	0.0010	***	F (5, 348) = 4.227
Genotype	<0.0001	****	F (1, 348) = 95.84
Timepoint	<0.0001	****	F (5, 348) = 22.46
Comparisons:			
LacZ:7DPE vs. LacZ:14DPE	0.8436	ns	
LacZ:7DPE vs. LacZ:21DPE	0.0013	**	
LacZ:7DPE vs. LacZ:28DPE	0.0671	ns	
LacZ:7DPE vs. LacZ:35DPE	0.0448	*	
LacZ:7DPE vs. LacZ:50DPE	<0.0001	****	
LacZ:7DPE vs. Aβ42:7DPE	0.8407	ns	
LacZ:14DPE vs. Aβ42:14DPE	0.0013	**	
LacZ:21DPE vs. Aβ42:21DPE	<0.0001	****	
LacZ:28DPE vs. Aβ42:28DPE	<0.0001	****	
LacZ:35DPE vs. Aβ42:35DPE	0.0027	**	
LacZ:50DPE vs. Aβ42:50DPE	0.9449	ns	
Aβ42:7DPE vs. Aβ42:14DPE	0.0013	**	
Aβ42:7DPE vs. Aβ42:21DPE	<0.0001	****	
Aβ42:7DPE vs. Aβ42:28DPE	<0.0001	****	
Aβ42:7DPE vs. Aβ42:35DPE	<0.0001	****	
Aβ42:7DPE vs. Aβ42:50DPE	<0.0001	****	

Figure 3.12A				
Log-rank (Mantel-Cox) test				
Chi square	290.3			
df	3			
P value	<0.0001			
P value summary	****			
Genotype	♀ LacZ (n=51)	♂ LacZ (n=70)	♀ Aβ42 (n=81)	♂ Aβ42 (n=83)
Median survival	44.5	43	20	19

		P value	**Summary**	**F number (DFn, DFd)**
Figure 3.13A				
Two-way ANOVA:				
Interaction		<0.0001	****	F (3, 432) = 33.34
Genotype		<0.0001	****	F (1, 432) = 34.74
Timepoint		<0.0001	****	F (3, 432) = 71.42
Comparisons:				
LacZ:3 DPE vs. LacZ:7 DPE		0.3921	ns	
LacZ:3 DPE vs. LacZ:14 DPE		<0.0001	****	
LacZ:3 DPE vs. LacZ:18 DPE		<0.0001	****	
LacZ:3 DPE vs. Aβ42:3 DPE		0.6215	ns	
LacZ:7 DPE vs. Aβ42:7 DPE		<0.0001	****	
LacZ:14 DPE vs. Aβ42:14 DPE		<0.0001	****	
LacZ:18 DPE vs. Aβ42:18 DPE		0.9696	ns	
Aβ42:3 DPE vs. Aβ42:14 DPE		<0.0001	****	
Aβ42:3 DPE vs. Aβ42:18 DPE		0.0038	**	
Aβ42:7 DPE vs. Aβ42:14 DPE		0.4221	ns	
Aβ42:7 DPE vs. Aβ42:18 DPE		<0.0001	****	
Figure 3.13B				
Two-way ANOVA:				
Interaction		<0.0001	****	F (3, 432) = 36.97
Genotype		0.0172	*	F (1, 432) = 5.717
Timepoint		<0.0001	****	F (3, 432) = 116.2
Comparisons:				
LacZ:3 DPE vs. LacZ:7 DPE		0.0188	*	
LacZ:3 DPE vs. LacZ:14 DPE		<0.0001	****	
LacZ:3 DPE vs. LacZ:18 DPE		<0.0001	****	
LacZ:3 DPE vs. Aβ42:3 DPE		0.9975	ns	
LacZ:7 DPE vs. Aβ42:7 DPE		<0.0001	****	
LacZ:14 DPE vs. Aβ42:14 DPE		0.7635	ns	
LacZ:18 DPE vs. Aβ42:18 DPE		0.0006	***	
Aβ42:3 DPE vs. Aβ42:14 DPE		<0.0001	****	
Aβ42:3 DPE vs. Aβ42:18 DPE		<0.0001	****	
Aβ42:7 DPE vs. Aβ42:14 DPE		0.9946	ns	
Aβ42:7 DPE vs. Aβ42:18 DPE		<0.0001	****	
Figure 3.13C				
Two-way ANOVA:				
Interaction		<0.0001	****	F (3, 432) = 24.49
Genotype		<0.0001	****	F (1, 432) = 50.63
Timepoint		<0.0001	****	F (3, 432) = 224.9
Comparisons:				
LacZ:3 DPE vs. LacZ:7 DPE		<0.0001	****	
LacZ:3 DPE vs. LacZ:14 DPE		<0.0001	****	
LacZ:3 DPE vs. LacZ:18 DPE		<0.0001	****	
LacZ:3 DPE vs. Aβ42:3 DPE		>0.9999	ns	
LacZ:7 DPE vs. Aβ42:7 DPE		0.7289	ns	
LacZ:14 DPE vs. Aβ42:14 DPE		<0.0001	****	
LacZ:18 DPE vs. Aβ42:18 DPE		<0.0001	****	
Aβ42:3 DPE vs. Aβ42:14 DPE		<0.0001	****	
Aβ42:3 DPE vs. Aβ42:18 DPE		<0.0001	****	
Aβ42:7 DPE vs. Aβ42:14 DPE		0.2539	ns	
Aβ42:7 DPE vs. Aβ42:18 DPE		0.2084	ns	

Appendix III. QUAS-Aβ42 forward sequence of Hsp70-Sv40 insertion region

Necrotic peptide; insect codon-modified Aβ42 peptide

```
CCTGGAGGGGCGATAAGTCAATTGTTCAACATGCGAAAGTGATACACGTGCGCTAAGCG
AAAGCTAAGCAAATAAACAAGCGCAGCTGAACAAGCTAAACAATCTGCAGTAAAGTGCA
AGTTAAAGTGAATCAATTAAAAGTAACCAGCAACCAAGTAAATCAACTGCAACTACTGA
AATCTGCCAAGAAGTAATTATTGAATACAAGAAGAGAACTCTGAATAGGGAATTGGGAA
TTCAACATGGCGAGCAAAGTCTCGATCCTTCTCCTGCTAACCGTCCATCTTCTGGCTGC
TCAGACCTTCGCCCAGGATGCGGAATTTCGCCATGACAGCGGCTACGAAGTGCATCATC
AAAAATTGGTGTTTTTTGCGGAAGACGTGGGCTCGAACAAAGGCGCGATTATTGGCTTG
ATGGTGGGCGGCGTGGTGATTGCGTAATCTAGAGGATCTTTGTGAAGGAACCTTACTTC
TGTGGTGTGACATAATTGGACAAACTACCTACAGAGATTTAAAGCTCTAAGGTAAATAT
AAAATTTTTAAGTGTATAATGTGTTAAACTACTGATTCTAATTGTTTGTGTATTTTAGA
TTCCAACCTATGGAAGAAAAGAGAAGGAAAAA
```